Search for the H-Dibaryon via the (K^-, K^+) Reaction on ^{12}C

Kazuhiro Yamamoto

A dissertation submitted in partial fulfillment of
the requirements for the degree of

Doctor of Science

Department of Physics
Kyoto University

May, 2000

Abstract

A search for the H-dibaryon via the (K^-, K^+) reaction on ^{12}C was performed at Brookhaven National Laboratory Alternating Gradient Synchrotron (BNL-AGS) using a high-intensity 1.8 GeV/c K^- beam. The H-dibaryon was looked for both in the direct production process, $K^- + {}^{12}\mathrm{C} \rightarrow K^+ + H + X$, and through the atomic capture process of Ξ^-, $(\Xi^-, {}^{12}\mathrm{C})_{atom} \rightarrow H + X$, where the Ξ^- was produced via the quasi-free (K^-, K^+) reaction on a proton in ^{12}C. A diamond target was exposed to the K^- beam in order to obtain the (K^-, K^+) reaction, and it was also used for a Ξ^- absorption target by taking advantage of its high density. The (K^-, K^+) reaction was measured with a large-acceptance magnetic spectrometer. A total of 3×10^5 (K^-, K^+) reaction events were obtained with 8×10^{11} incident K^-'s.

A missing-mass analysis below the end point of the quasi-free Ξ^- production was used to investigate the direct H production process. No evidence of the H was observed, and an upper limit on the H-production cross section in the K^+ forward angle was obtained in the range of a few nb/sr to 10 nb/sr for the H masses below 2100 MeV/c^2 with 90% C.L. This upper limit is the most sensitive H search result to date for the H of the mass less than 2160 MeV/c^2.

For the study of the H via the atomic capture process of Ξ^-, the scintillating-fiber detectors and the neutron counter arrays were used to detect decay products of the H in coincidence with the (K^-, K^+) reaction. The decay modes of $H \rightarrow \Sigma^- p$ and $H \rightarrow \Lambda n$ were searched for by investigating their decay kinematics. No clear signals were found. The 90% C.L. upper limits were obtained with respect to the product of the branching ratio of the H formation from the $(\Xi^-, {}^{12}\mathrm{C})_{atom}$ and that of the H decay into $\Sigma^- p$ and Λn as a function of the H lifetime ($0.1 \sim 10$ ns) and the H mass ($2140 \sim 2230$ MeV/c^2 for $H \rightarrow \Sigma^- p$ and $2180 \sim 2230$ MeV/c^2 for $H \rightarrow \Lambda n$). In the decay mode of $H \rightarrow \Sigma^- p$, the upper limits are less than 30% in the region of the H lifetime $0.2 \sim 2$ ns, especially 10% for the H masess larger than 2220 MeV/c^2 and the H lifetimes of $\sim$1 ns. On the other hand, the minimum upper limit of 26% was obtained for the $H \rightarrow \Lambda n$ mode with the H mass and lifetime around 2205 MeV/c^2 and 0.4 ns.

Contents

Chapter 1

Introduction

1.1 H-dibaryon

One of the most important recent developments in physics is to have found and established quarks and gluons as constituents of hadrons. The quarks and gluons are regarded as carriers of the color charge, and the color interaction between quarks and gluons is generally believed to be described by quantum-chromodynamics (QCD), a theory of strong interaction, because of the quite successful agreement between theoretical calculations and numerous experimental results in the high energy region. However, development of a theoretical framework of QCD for the low energy region, which should predict masses and low-energy interactions of hadrons, is still in progress due to its nonperturbative nature. In such difficulties, the structure of hadrons has been studied by means of various quark models based on QCD. In the naive quark model, baryons and mesons are considered to be composites of three quarks (qqq) and a quark-antiquark pair ($q\bar{q}$) respectively, and this simple quark assignment consistently explains spin, parity, charge, and magnetic moment. The mass of hadrons was also calculated with several additional effective interactions between quarks. Using these frameworks, nonstandard hadrons such as "baryonium ($qqq\bar{q}\bar{q}$)", "pentaquark ($qqqq\bar{q}$)", "hybrid meson ($q\bar{q}g$)", and "dibaryon ($qqqqqq$)" were theoretically investigated; current QCD theory requires only that hadrons are formed in color-singlet states but does not limit the number of quarks. Studies of the quark matter including "strangelet" and "charmlet" have been also performed in the extension of the above quark-model framework.

In 1977, R.L. Jaffe predicted the doubly-strange dibaryon, which was called H-dibaryon, to be stable with respect to the strong interaction in the quark configuration of $uuddss$ with $J^P = 0^+$ and $I = 0$ using the MIT bag model [1]. It should be noted that this H is a six-quark state in a single QCD bag and not a deuteron-like baryon molecule. The originally predicted mass was 2150 MeV/c^2, 80 MeV/c^2 below the mass of $\Lambda\Lambda$ which is the lowest lying baryon pair in the S $= -2$ sector. This binding is due to the large attractive force of the color-magnetic interaction resulting from the one-gluon exchange between

quarks. The corresponding term H_m is expressed as

$$H_m = -\alpha_s \sum_{i>j}^{N} \sum_{a=1}^{8} (\vec{\sigma}_i \lambda_i^a) \cdot (\vec{\sigma}_j \lambda_j^a) M(m_i, m_j)\,, \tag{1.1}$$

where α_s is the strong coupling constant, $\vec{\sigma}_i$ and λ_i^a are the Pauli and Gell-Mann matrices, N is the total number of quarks, $m_{i(j)}$ refers to the mass of $i(j)$-th quark, and $M(m_i, m_j)$ stands for the interaction strength. In a system containing N quarks and no antiquarks, the energy eigenvalue of Eq. (1.1) is written to be

$$E_m = \alpha_s \left\{ 8N - \frac{1}{2} C_6 + \frac{4}{3} J(J+1) \right\} \overline{M}\,, \tag{1.2}$$

where C_6 is the eigenvalue of the quadratic Casimir operator of SU(6) for the color-spin representation of the quarks, J is the total angular momentum, and $\overline{M}$ is an average interaction strength. The value C_6 becomes the largest, 144, for the most symmetric color-spin configuration which gives the largest reduction to the resulting mass. Due to Pauli's exclusion principle, such color-spin symmetric configuration can be realized in the flavor-singlet state, namely the six-quark state $uuddss$ with $J^P = 0$ and $I = 0$, which is the H-dibaryon predicted by Jaffe.

Following the prediction of the stable H-dibaryon, various calculations of the H mass were performed using the bag model framework [2]-[11]. Some of them include corrections in terms of center-of-mass motion [4], pionic clouds [5, 6], and bag surface energy [7]. These corrections pushed up the H mass, and the unbound H was sometimes found. However, Kerbikov suggested that because of couplings to hadronic channels $\Lambda\Lambda$, $N\Xi$, and $\Sigma\Sigma$ the mass of the H would decrease by $150 \sim 200$ MeV for all the previous predictions [8]. One of the most recent bag-model calculations was carried out by Golowich and Sotirelis [11]. They studied the higher order $O(\alpha_s^2)$ contribution in a truncated bag model; the values for the H mass (M_H) was obtained in the range $2.12\ \mathrm{GeV}/c^2 < M_H < 2.19\ \mathrm{GeV}/c^2$.

The doubly strange dibaryon having the same quantum numbers as Jaffe had predicted as the H was also identified in the Skyrme model, where baryons are considered as topological solitons in a non-linear chiral field. Calculations within this scheme have usually provided the bound H [12]-[19]; sometimes the values of much lower mass than the bag model predicted were found [14, 15, 17]. On the other hand, several different approaches for the extension of the Skyrme model to strange baryons have been attempted in Refs. [20, 21, 22], where the H was found to be unbound or quite loosely bound. However, it should be noted that the accuracy of the Skyrme model predictions is generally in $20 \sim 30\%$.

The quark cluster model is also one of the models that can make a quantitative prediction of the binding energy. Quarks are described as particles moving non-relativistically in a potential. Early works using this model showed no bound state for S=−2 dibaryon configuration [23, 24, 25]. An attempt to introduce the instanton-induced interaction provided less probability of the bound H because of the strong three-body repulsion [26]. However, the major improvement of the quark cluster model was done by incorporating the

pseudoscalar and σ meson exchange potential in order to describe long and medium range interactions. Although the predicted H masses strongly depends on the quark confinement mechanism, most of the calculations using this framework found the bound state of the H [27]-[35]. The H binding energy (B_H) was predicted to be relatively small value ($\lesssim$ 25 MeV) except for Ref. [29], where the quark confinement by the flip-flop model brought about $B_H = 60 \sim 120$ MeV, and Ref. [32], where B_H was predicted to be 252 MeV using an extended basis consisting of the usual two-baryon configuration and an additional spatially symmetric six-quark state.

Lattice QCD gives us a method to calculate the H mass numerically from first principles. However, a concern lies on effects from the finite lattice size. The first attempt to calculate the H mass using lattice QCD was reported by Mackenzie and Thacker [36]. They worked on a $6^2 \times 12 \times 18$ lattice and obtained the larger value for the H mass than that for a double of the Λ mass, namely the unbound H. However, the second calculation by Iwasaki *et al.* with a larger lattice size $16^3 \times 48$ indicated the quite strongly bound H which is below the NN threshold [37]. The latest published lattice study on the H mass was carried out by Negele *et al.* using a $16^3 \times 32$ lattice and a $24^3 \times 32$ lattice [38]. Although the former case ($16^3 \times 32$) provided the deeply bound state, which is consistent with the result by Iwasaki *et al.*, the latter case with a larger lattice ($24^3 \times 32$) showed the unbound H. Currently, another independent calculation with $16^3 \times 30$ and $24^3 \times 30$ lattices are being performed by Wetzorke *et al.*, and preliminary results can be found in Ref. [39]. Although their statistics is not yet sufficient to draw a definite conclusion, the preliminary results supported the findings of Negele *et al.* It is expected that the current striking progress on the computing power will resolve the finite volume dependence of lattice QCD.

The H mass has been predicted with many other approaches such as QCD sum rule [40, 41], flux-tube model [42], color dielectric model [43, 44, 45], and other various quark models [46]-[57]. The predicted mass ranges widely from 1.7 GeV/c^2 to 2.8 GeV/c^2.

As seen above, the doubly strange dibaryon H does appear not only in the bag model but also in many other types of calculation. In that sense, the stability of H is a global interest of the low-energy QCD, which is expected to improve our understanding on the quark dynamics in hadrons.

1.2 Previous and ongoing experiments

Since the H-dibaryon was theoretically predicted, many experimental searches have been performed with various techniques using protons, heavy ions, kaons, etc.

Just after Jaffe's prediction of the H, Carroll *et al.* made an experiment at Brookhaven to search for the H in the missing mass spectrum of the reaction, $p + p \to K^+ + K^+ + X$ (BNL-E703) [58]. No narrow structure suggesting the H was observed, and a 90% C.L. upper limit on the production cross section was set in the range of $30 \sim 130$ nb depending on the H mass ($2.0\ \mathrm{GeV}/c^2 \sim 2.5\ \mathrm{GeV}/c^2$). However, the calculated cross section [59] is two orders of magnitude lower than the obtained upper limit, thus the above upper limit

is too crude to rule out the existence of the H-dibaryon.

Condo *et al.* searched for the H in the antiproton annihilation, $\bar{p} + A \to H + X$ [60]. Various nuclear targets (C, Ti, Ta and Pb) were exposed to an anti-proton beam in the BNL 30-inch hydrogen bubble chamber, and about 80,000 $\bar{p}$ annihilations were observed. No evidence was found, and the obtained upper limit for the production rate of the H in $\bar{p}A$ collisions is 9×10^{-5} with 90% C.L.

At the Serpukhov Proton Synchrotron, streamer chambers filled with a helium-neon gas mixture were utilized for the H search in $\pi^- + A \to H + X$ by Bärwolff *et al* [61]. Although the decay mode of $H \to \Sigma^- p$ with the subsequent $\Sigma^- \to \pi^- n$ decay was looked for, no signal was found. A 90% C.L. upper limit on the H production rate per inelastic $\pi^- A$ collision was obtained to be 1.5×10^{-4}. The corresponding 90% C.L. upper limit on the production cross section is 160 nb.

In the propane bubble chamber experiment at Dubna using a 10 GeV/c proton beam, four events were reported by Shahbazian *et al.* as H candidates [62]-[65], either of which showed a "V" track associated with a production star and was interpreted as the $H \to \Sigma^- p$ decay. The reconstructed masses were claimed to be 2173.94 ± 13.10 MeV/c^2, 2218 ± 12 MeV/c^2, 2408.9 ± 11.2 MeV/c^2, and 2384.9 ± 31.0 MeV/c^2, respectively. Also, the spark chamber experiment by Alekseev *et al.*, where C and Cu targets were exposed to a neutron beam, showed another H candidate which was interpreted as $H \to \Lambda p \pi^-$ [66]. The reconstructed mass of this event was 2220.1 ± 5.4 MeV/c^2. However, it should be noted that these events could be explained as other interpretations such as $\Lambda + n \to \Sigma^- + p$ for $H \to \Sigma^- p$ candidates and two Λ production for $H \to \Lambda p \pi^-$ candidate. Although the particle identification of products generated at the star is important for assuring the neutral particle of our interest to be carrying two units of strangeness, above two experiments had no proper treatments on it.

An experiment on strange-particle production in $\bar{p}$-Xe interactions was performed using the 700-liter xenon bubble chamber at ITEP. The chamber was exposed to a $\bar{p}$ beam with momentum of about 1.0 GeV/c. The H was expected to be created via $\bar{p}$Xe annihilation. No H candidates were found in a sample of 7.8×10^5 antiproton annihilations, and the upper limit for the frequency of the reaction $\bar{p} + \mathrm{Xe} \to H + X$ turned out to be 1.2×10^{-5} [67], which is about one order of magnitude lower than the value reported in Ref. [60].

If the mass of H is smaller than that of two nucleons, the H would be formed from the decay of two nucleons. Ejiri *et al.* searched for the H by means of double weak decays in the follows reactions [68]:

$$\begin{array}{lll} {}^{A}_{Z}N \to {}^{A-2}_{Z-1}N + H + \beta^+ + \nu_e & \text{for } d \text{ and } {}^{127}\mathrm{I}\,, \\ {}^{A}_{Z}N \to {}^{A-2}_{Z}N + H + \gamma & \text{for } {}^{72}\mathrm{Ge},\ {}^{70}\mathrm{Ge}, \text{ and } {}^{10}\mathrm{Be}\,. \end{array} \tag{1.3}$$

No evidence was found and the H-dibaryon with the mass less than 1875.1 MeV/c^2 (2.7 MeV/c^2 below the mass of $p + n$) was excluded.

The (K^-, K^+) reaction is a good way to confirm the deposit of two units of strangeness at the reaction point, and hence there have been a series of experiments using this process. Since the details of this process are described in the next section, the experiments are just reviewed here.

At KEK-PS, the H was searched for via the direct process using an emulsion-counter hybrid method by Aoki *et al.* (KEK-E176) [69, 70], where a proton-pair in a nucleus was expected to react with K^- to produce the H, namely $K^- + (pp) \to K^+ + H$. A separated peak in the K^+ momentum spectrum above the quasi-free Ξ^- production was the signal of H production. The incident K^- momentum was 1.66 GeV/c^2. By scanning back the K^+ tracks in the emulsion, the reaction vertices were visually investigated and this was useful for background rejection. As a result, no signal was seen and the upper limit on the production cross section was set to $0.2 \sim 0.6\%$ of the quasi-free Ξ^- production with 90% C.L. in the H mass range from 1900 MeV/c^2 to 2160 MeV/c^2. Another important result of this experiment is to have found the double-Λ hypernucleus with high reliability, which is described in detail in the later paragraph.

At the same beam line at KEK, another H search experiment (KEK-E224) was performed [71]-[74]. Instead of the emulsion, a newly developed scintillating-fiber live target was used as a triggerable visual detector together with the magnetic spectrometer. This detector was sensitive for neutral particles having a few-cm path length which corresponds to the lifetime of $10^{-10} \sim 10^{-8}$ sec; they cannot be investigated with the emulsion. The H was searched for in the direct production process and also via the atomic capture of Ξ^- in the $\Sigma^- p$ decay mode. However, no evidence for the H was observed. A 90% C.L. upper limit on the forward-angle cross section of the direct H production was set to be $0.04 \sim 0.6$ μb/sr for the H mass range $1850 \sim 2215$ MeV/c^2 [71, 72], while a 90% C.L. upper limit of $0.35 \sim 0.5$ μb/sr was obtained with respect to the product of the forward-angle cross section on the direct H production and the decay branching ratio of $H \to \Sigma^- p$ for the H mass range $2200 \sim 2230$ MeV/c^2 [73]. Concerning the H production through the atomic capture process of Ξ^-, an upper limit in terms of the product of the branching ratio of the H formation from the $(\Xi^-, {}^{12}\mathrm{C})_{atom}$ and that of H decay into $\Sigma^- p$ was determined in the range from 0.2 to 1 for the H masses 2150 MeV/c^2 $\sim$ two Λ mass and the H lifetime $10^{-10} \sim 10^{-9}$ sec [72]. Recently, Ahn *et al.* have suggested a possible Λ-Λ resonance by investigating the invariant-mass spectrum of $\Lambda\Lambda$ using the E224 data [75].

At Brookhaven AGS, an experiment to search for the H via the atomic capture of Ξ^- in a deuterium-atom was carried out with a combined cryogenic target of liquid-hydrogen and deuterium (BNL-E813) [76]-[82]. In this experiment, Ξ^- hyperons were created via $p(K^-, K^+)\Xi^-$ in the liquid-hydrogen vessel, and then stopped to produce Ξ^--d atoms in the liquid-deuterium vessel. The H was searched for by looking into the monoenergetic neutrons from the two-body decay, $(\Xi^-, d)_{atom} \to H + n$. The energy of neutrons could be used to determine the H mass. The data have been partially analyzed, and the final result will appear in the foreseeable future.

Using the same beam line at the AGS, the direct H production in ${}^3\mathrm{He}(K^-, K^+)Hn$ was

searched for by use of a liquid-^{3}He target (BNL-E836). The result was reported in Refs. [83, 84]; the upper limits on the H production cross section were obtained in the range of 0.058 to 0.021 μb/sr for assumed H masses from 1850 MeV/c^2 to 2180 MeV/c^2. Although the data on a ^{6}Li target was also collected in this experiment, any evidence of the H was not seen again [85].

A unique experiment using a hyperon beam was carried out at CERN-SPS (WA89). H-dibaryon states above threshold were looked for by investigating the invariant mass of their decay channels, $\Lambda\Lambda$ and $\Xi^- p$, using a 330 GeV/c Σ^- hyperon beam incident on C/Cu targets. The upper limits for the production of a resonance in the $\Lambda\Lambda$ and $\Xi^- p$ channels were reported to be 156 nb and 1330 nb respectively [86].

The strangeness production in high-energy heavy ion collisions is another possible method to search for the H. Preliminary results on the H search in collisions of 14.6 A GeV/c Si ions with a Pb target at the AGS was reported (BNL-810) [87]. The events having a topology consistent with $H \to \Sigma^- p$ decay were searched for with use of a time-projection chamber, and 33 candidates on a background of 11 were reported from a sample of 5000 central collisions. Recent updates showed the H mass of 2210 ± 15 MeV/c^2 with 29 $\Sigma^- p$ and 21 $\Lambda p\pi^-$ events as the analysis result of 20,000 central collisions. These candidates are consistent with a lifetime $c\tau$ around 4 cm, a half of that of Λ [88]. However, the production rate of H implied by this experiment is a factor of 25 to 50 times larger than that based on the $\Lambda\Lambda$ coalescence model of Baltz *et al.* [89], and of the same order of magnitude as Ξ^- production.

Another H search experiment which has an improved sensitivity was made in 11.6 A GeV/c Au+Au collisions at the AGS (BNL-E896) [90, 91]. The experimental setup containing a 4.7 Tesla superconducting sweeper magnet and distributed drift chambers allows to detect the $H \to \Sigma^- p$ decay topology under the condition free from charged background tracks generated at the target. This experiment has good sensitivity for lifetimes as short as typical hyperon lifetimes, thus is expected to inspect a potential $H(2210)$ reported in the E810 analysis. The data taking run was carried out in 1998, and the analysis is currently in progress.

Rusek *et al.* reported the indirect H search by means of the H-nucleus bound states production in 10.8 A GeV/c Au collisions with a Pt target [92]. This was a byproduct analysis of the strangelet search experiment at the AGS (BNL-E886) [93, 94]. Nuclear systems that have significantly different mass-to-charge (M/Z) ratios compared to known nuclear bound states were searched for as the H-nucleus signals. Although a good particle separation was achieved among π, K, p, and light nuclear species, no events having unusual M/Z were found for the lifetimes larger than several-hundred ns. The 90% C.L. upper limits on the production cross section ($Ed^3\sigma/dp^3$) were obtained to be 5×10^{-5} mb/GeV^2 for H-d nuclei and 7×10^{-6} mb/GeV^2 for H-^{3}He nuclei in the above lifetime range.

The heavy ion program was also executed at CERN-SPS. In WA97 experiment, Λ-Λ pairs produced in Pb-Pb collisions are being studied in terms of their invariant mass and HBT correlation. A preliminary result including a half of the total statistics was reported

in Ref. [95], which showed no evidence of the Λ-Λ resonance.

There are four recent experiments using a high-energy proton beam incident on the target. An experiment to search for H decays into $\Lambda p\pi^-$ and $\Sigma^- p$ final states was performed using an 18 GeV/c secondary proton beam at the AGS in collisions with a Au target (BNL-E910). The preliminary result showing no clear H signal in the $\Lambda p\pi^-$ sample and no events consistent with $H \to \Sigma^- p$ decays can be found in Ref. [96].

The reaction at the first H search experiment, $p+p \to K^+ + K^+ + H$, was reinvestigated with much higher sensitivity using a liquid-hydrogen target and a 12 GeV/c primary proton beam at KEK-PS (KEK-E248) [97]. The double-arm spectrometer containing a highly efficient particle-identification system for high momentum $\pi/K/p$ using low-index aerogel Čerenkov counters was designed to perform the missing mass spectroscopy of $p + p \to K^+ + K^+ + X$. The data taking was completed, and the analysis is in progress.

The other two experiments were carried out by utilizing the experimental setup for neutral kaon rare decays. One of this kind of experiments was carried out at the AGS. In this experiment, the H was searched for by means of the weak decay and also the dissociation process (BNL-E888). In the weak decay search, the decays $H \to \Lambda n$ and/or $H \to \Sigma^0 n \to \Lambda\gamma n$ were looked for. The signal was a Λ which does not point back to the target. Two candidates were initially reported, and the 90% C.L. upper limits on H production cross section were set in the range of $10^{-4} \sim 10^{-5}$ of that for Λ production for H lifetimes longer than 6 ns [98]. The further analysis subsequently provided the two candidates a more likely interpretation as semi-leptonic K^0_L decays with misidentified decay products [99]. For the dissociation process, the decay chain $H + A \to \Lambda\Lambda A \to p\pi^- p\pi^- A$ was searched for in a plastic scintillator dissociator [100]. No evidence for H dissociation was observed, and a 90% C.L. upper limit on the forward-angle H production cross section was obtained to be 1 mb/sr for H lifetimes longer than 10 ns.

The H search was also performed as a byproduct of the KTeV experiment at Fermilab (FNAL-E799II). The weak decays $H \to \Lambda p\pi^-$ were looked for in the 65-meter long vacuum decay volume [101]. They presented upper limits on the H production cross section compared to that of Ξ^0 production as a function of the H mass and lifetime. Using models proposed by Rotondo [102] and Donoghue *et al.* [103], upper limits on the ratio $(d\sigma_H/d\Omega)/(d\sigma_{\Xi^0}/d\Omega)$ were set in the range of $10^{-4} \sim 10^{-6}$ for the H mass of 2194 MeV/c^2 ($\Lambda p\pi^-$ threshold) $\sim$ 2231 MeV/c^2 ($\Lambda\Lambda$ threshold) and lifetime larger than $\sim$ 3.5 ns. These upper limits are up to five orders of magnitude smaller than the theoretical prediction.

It is worth mentioning about double-Λ hypernuclei as well as the H-dibaryon. The H and double-Λ hypernuclei have a close connection in the sense that measurement of the ground state of a double-Λ hypernucleus gives an indirect lower limit for the H mass. If the mass of H is lower than that of two Λ's in the nucleus, a double-Λ hypernucleus is expected to decay into an H-nucleus. Hence the observation of a double-Λ hypernucleus implies the relation $M_H > 2M_\Lambda - B_{\Lambda\Lambda}$, where M_H and M_Λ refer to the H mass and Λ mass, and $B_{\Lambda\Lambda}$ means the binding energy of two Λ's in the nucleus. In 1960's, two events of double-Λ hypernuclei were reported with the observation of Ξ^- captures and sequential weak decays

in the emulsion. One was interpreted as ${}^{10}_{\Lambda\Lambda}$Be with $B_{\Lambda\Lambda}$ of 17.5 ± 0.4 MeV [104], while the other was interpreted as ${}^{6}_{\Lambda\Lambda}$He with $B_{\Lambda\Lambda}$ of 10.9 ± 0.8 MeV [105]. In both experiments, a K^- beam was exposed to the emulsion in order to produce Ξ^-'s. However, if these events are truly double-Λ hypernuclei, it is remarkable to have observed sequential double pionic decays as well as double-Λ hypernuclear formation under the quite low statistics.

Recently, another event was reported at KEK using a counter-emulsion hybrid method (KEK-E176). Since the Ξ^- production was tagged by measuring the (K^-, K^+) reaction with the counter system, this event is even more reliable than the previously reported ones. The event was interpreted as either ${}^{13}_{\Lambda\Lambda}$B with $B_{\Lambda\Lambda}$ of 27.6 ± 0.7 MeV or ${}^{10}_{\Lambda\Lambda}$Be with $B_{\Lambda\Lambda}$ of 8.5 ± 0.7 MeV [106]. This result indirectly requires the H mass to be larger than 2203.7 ± 0.7 MeV/c^2.

Since then, several experiments to study double-Λ hypernuclei have been proposed. A search for ${}^{12}_{\Lambda\Lambda}$B was performed at the AGS by looking for monoenergetic neutrons from $(\Xi^-, {}^{12}\mathrm{C})_{atom} \rightarrow {}^{12}_{\Lambda\Lambda}\mathrm{B}+n$ (BNL-E885). The details can be found in Refs. [107, 108], and it is another topic of the experiment reported in this thesis. An experiment to look for double-Λ hyper-fragments, ${}^{5}_{\Lambda\Lambda}$H and ${}^{6}_{\Lambda\Lambda}$He, was made via the (K^-, K^+) reaction on ^{9}Be at the same beam line of the AGS (BNL-E906) [109]. Characteristic pions would be detected as a signal of pionic weak decays using the cylindrical detector system containing a cylindrical drift chamber in a solenoid magnet. The data taking was completed, and the data are being analyzed now. The upgraded version of the counter-emulsion hybrid experiment is currently going on at KEK (KEK-E373) [110]. This experiment aims to obtain ten times larger statistics than that of KEK-E176, and it is expected to resolve the ambiguity of possible two interpretations reported by KEK-E176.

To summarize, although a number of H searches have been performed as mentioned above, no clear evidence of its existence or nonexistence has been established. However, many restrictions have been imposed with respect to the production cross section and mass of the H. Especially, the long-lived H with lifetime more than a few ns is quite unlikely according to the experiments using heavy ion collisions and pA collisions. The investigation of a short-lived H of which lifetime is comparable to that of hyperons is desirable. As for the H mass, the observation of the double-Λ hypernucleus at KEK-E176 have set an indirect lower limit to be 2203 MeV/c^2. This limit was, however, obtained from only one event. Although an experiment to accumulate more statistics of the double-Λ hypernuclei is currently going on in order to confirm the KEK-E176 result as stated above (KEK-E373), a search for the deeply bound H whose mass is less than 2203 MeV/c^2 is also quite important as a complementary study of the double strangeness system. The H-dibaryon is still open question in the low energy QCD.

1.3 H production via the (K^-, K^+) reaction

Although many kinds of processes for H production were shown in the previous section, here the subject is focused on the H production via the (K^-, K^+) reaction. Since two

units of strangeness are transferred to a target nucleus, the (K^-, K^+) reaction is one of the most efficient way to produce S $= -2$ systems. There are two different processes which have potential to produce the H using the (K^-, K^+) reaction.

One is the direct production process, in which the H wound be created at the vertex of the (K^-, K^+) reaction as follows:

$$K^- + A \rightarrow K^+ + H + X. \tag{1.4}$$

From a view of the elementary process, two protons in a nucleus participate in the reaction:

$$K^- + (pp) \rightarrow K^+ + H, \tag{1.5}$$

where the Ξ^- is virtually created with the first proton via $p(K^-, K^+)\Xi^-$, and then the second proton and the Ξ^- fuse into the H. The process is schematically shown in Figure 1.1. As Aerts and Dover suggested in the theoretical calculation for the ^{3}He target [111], the H production spectra of the K^+ momentum and the (K^-, K^+) missing mass have a peak structure; it would be well-separated from that of the quasi-free Ξ^- production in case of the relatively light H mass. Therefore, the signal of H can be searched for with the careful investigation of the momentum and missing mass spectrum. It should be also noted that the direct H production is a competing process with the Ξ^- and double-Λ hypernuclear production [112, 113].

The other possible process to produce the H is via the atomic capture of Ξ^-. The quasi-free Ξ^- production,

$$K^- + (p) \rightarrow K^+ + \Xi^-, \tag{1.6}$$

is the first step of this process, where (p) refers to a proton in a nucleus. The created Ξ^- is degraded and brought to rest in the material. Then the H is expected to be produced through the Ξ^- atom as follows:

$$(\Xi^-, A)_{atom} \rightarrow H + X. \tag{1.7}$$

The schematic diagram is also shown in Figure 1.2. In this case, the energy excess due to the Q-value prevents the H from being formed from proton and Ξ^- if the H mass is low. Aerts

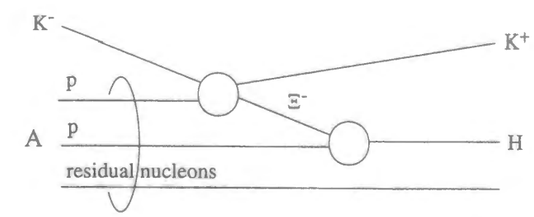

Figure 1.1: Schematic diagram of the direct H production. A virtual Ξ^- created via $p(K^-, K^+)\Xi^-$ from a first proton fuses with a second proton to form the H.

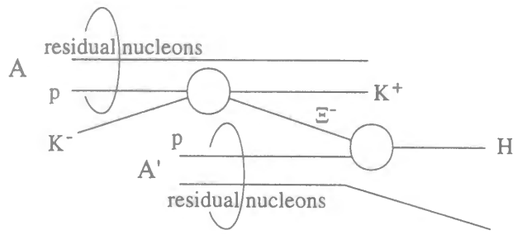

Figure 1.2: Schematic diagram of the H formation via the atomic capture of Ξ^-.

and Dover performed theoretical calculations on the branching ratio of the H formation from the $(\Xi^-, d)_{atom}$ and $(\Xi^-, {}^4\mathrm{He})_{atom}$ [114]. In both cases, the estimated branching ratio is sizable (> 0.1) and increases as the H mass becomes larger. Especially, it amounts to more than 90% for the $(\Xi^-, {}^4\mathrm{He})_{atom}$ with the H mass larger than $\sim$2220 MeV/c^2 using the Nijmegen model-D potential. The atomic capture process of Ξ^- is sensitive to the heavy H, whereas the direct process is suitable to search for the light H.

Although only the H has been mentioned as a product from the Ξ^- atom, there are in fact many other final states from the Ξ^- atom which include double- and single-Λ hypernuclear production. The systematic theoretical estimates can be found in Refs. [115, 116]. All of them are competing processes of the H production via the atomic capture of Ξ^-.

In our experiment (BNL-E885), we have searched for $\mathrm{S} = -2$ nuclei and the H-dibaryon in both direct and the Ξ^- atomic capture processes via the (K^-, K^+) reaction mentioned above. Using a diamond target as a (K^-, K^+) reaction target and also a Ξ^- absorption target, the following channels were studied:

- direct process

$$K^- + {}^{12}\mathrm{C} \rightarrow K^+ + {}^{12}_{\Xi}\mathrm{Be}^* \quad (1.8)$$
$$K^+ + {}^{12}_{\Lambda\Lambda}\mathrm{Be}^* \quad (1.9)$$
$$K^+ + H + X\,, \quad (1.10)$$

- Ξ^- atomic capture process

$$K^- + (p) \rightarrow K^+ + \Xi^-, \quad (1.11)$$

$$(\Xi^-, {}^{12}\mathrm{C})_{atom} \rightarrow {}^{12}_{\Lambda\Lambda}\mathrm{B} + n \quad (1.12)$$
$$H + X\,. \quad (1.13)$$

The direct process was investigated with the missing mass analysis, while the Ξ^- atomic capture process was studied using additional detectors, the neutron counter arrays and

the scintillating-fiber (SCIFI) detectors. Among the above physics topics, the discussion is focused on the search for the H-dibaryon in this report. Analyses of the other channels can be found in Refs. [107, 108, 117, 118, 135]. The experimental setup, data analysis, and obtained results with respect to the H search are described in the following chapters.

Chapter 2

Experiment

2.1 Overview

The experiment was carried out using a 1.8 GeV/c K^- beam at the D6 beam line of the Brookhaven National Laboratory Alternating Gradient Synchrotron (BNL-AGS). The typical K^-/π^- ratio was 1.4 with the intensity of 1.0×10^6/spill (~1.2 sec). The physics objective of the experiment was to search for S=−2 nuclear objects such as double-Λ hypernuclei, Ξ^- hypernuclei, and the H-dibaryon using the (K^-, K^+) reaction on a carbon target. Since the S=−2 objects can be produced through both of the direct production and the atomic capture of Ξ^-, as mentioned in the previous chapter, we have designed the experiment so as to study both processes. The direct process can be searched for by looking into the bound region of the ^{11}B+Ξ^- system which is free from the large population of the quasi-free Ξ^- production, while measurements of decay products are used to find candidates of the S=−2 systems produced via the atomic capture of Ξ^-. As mentioned in the introduction, the story is focused on the H search in this report.

Figure 2.1 shows a magnetic spectrometer for measurement of the (K^-, K^+) reaction. This spectrometer was originally constructed for the previous H-dibaryon search experiments (BNL-E813 [76]-[82], BNL-E836 [83, 84, 85]). We have made some alternations and upgrades for our experiment. The spectrometer is mainly composed of a dipole magnet (48D48), drift chambers (ID1-3, FD0-3, and BD1-2), aerogel Čerenkov counters (IC, FC0, FC, and BC), and scintillator hodoscopes (MP, MT, IT, FP, BP, and BT). In order to produce the (K^-, K^+) reaction, a diamond target, which is made of industrial diamond wafers, was placed at the final focus of the beam line. The momentum of particles was analyzed by the dipole magnet with the tracking information from the drift chambers. The scintillator hodoscopes provided us the timing information from which we knew the time-of-flight. The other roles of the scintillator hodoscopes were the definition of acceptance and the online triggers. The aerogel Čerenkov counters were used for the background subtraction in the (K^-, K^+) reaction. The main backgrounds of K^-'s in the incident beam were π^-'s, and those of outgoing K^+'s were π^+'s and protons. The counter IC discriminated between the K^- and the π^-. Also the separation of the K^+ from the π^+ was achieved by FC and BC, whereas FC0 suppressed outgoing protons. Since the (K^-, K^+) reaction is a rare event,

the background subtraction is important to reduce the trigger rate and thus to raise the live time of the data acquisition.

Around the target, apparatuses for the detection of decay particles were installed in the out-of-beam directions. These detectors are mainly for the analysis of the atomic capture process of Ξ^-. Neutron counter arrays were placed on the right and left sides of the target with a large solid angle. They consist of thick plastic scintillator logs for neutron detection and thin plastic scintillator plates which were located in front of the scintillator logs in order to veto charged particles. Above and below the target, two identical scintillating fiber (SCIFI) blocks were installed. The block was fabricated by stacking scintillating fiber sheets alternately in two directions. Each fiber has a 1mm by 1mm square-shape cross section. Figure 2.2 represents a basic concept of this detector. When a charged particle enters the block, photons are emitted from the fibers which the particle passes through. Therefore the particle track can be observed as a photon image at the end of each arm. The image was viewed by an image intensifier tube (IIT) and focused on a CCD camera. By combining images on both arms, three-dimensional information was obtained. The weak decay topology of the H-dibaryon can be observed in this detector in coincidence with the (K^-, K^+) reaction.

The experimental data was taken from March to June in 1996. The diamond target was exposed to $8 \times 10^{11} K^-$'s in total and about 3×10^5 (K^-, K^+) events were collected.

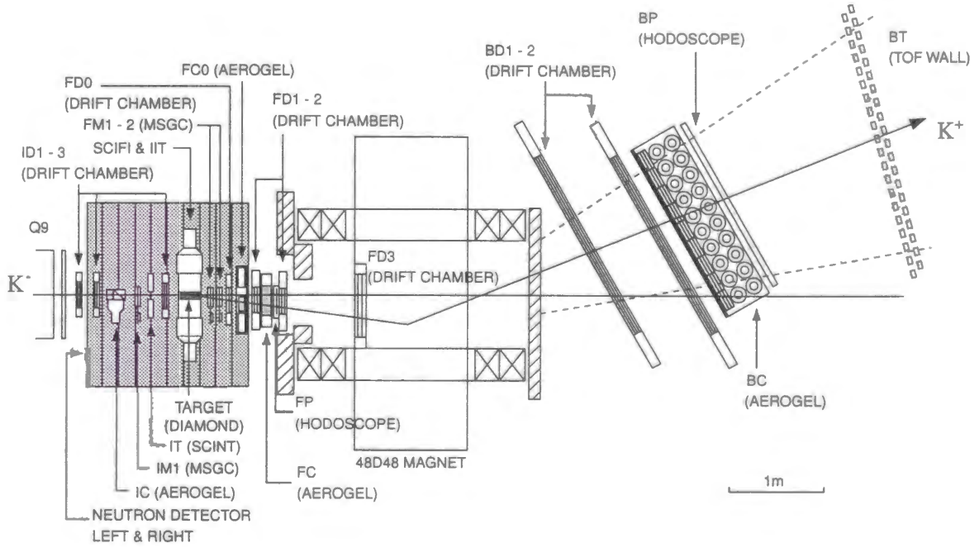

Figure 2.1: Schematic side view of the experimental setup.

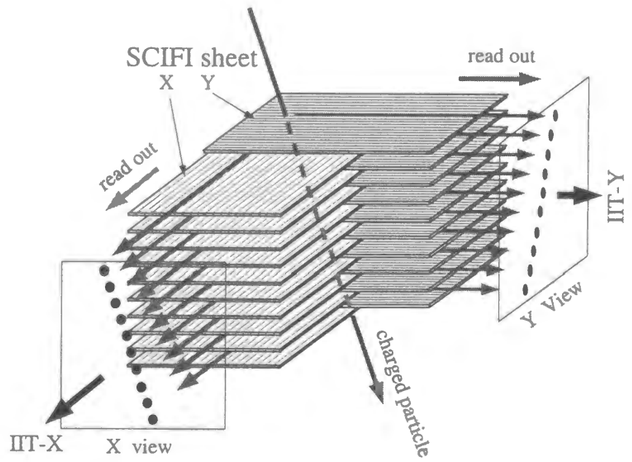

Figure 2.2: Basic concept of the SCIFI block.

2.2 D6 beam line

The BNL-AGS D6 beam line was built in 1991 in order to deliver a 1-2 GeV/c K^- beam of high intensity and high purity. Figure 2.3 shows a schematic view of the beam line. The details are described in Ref. [119]. The primary protons accelerated up to 24 GeV/c were extracted from the AGS, and hit a 9.0 cm long, 0.7 cm wide, and 1.0 cm high platinum target with the typical intensity of 1-10 $\times 10^{12}$ per spill. One spill corresponds to 1.2 seconds among 2.5-second beam cycle. The negative-charged secondary particles in the direction of 5 degrees to the primary beam were deflected by 25 degrees with the first dipole magnet (D1), and then transported to the final focus through the beam line which incorporates 3 dipoles (D1-3), 9 quadrupoles (Q1-9), 6 sextupoles (S1-6), 5 octupoles (O1-5), and collimators (4JAW, HS, and MS1,2). The beam momentum in our experiment was 1.8 GeV/c with $\pm 3\%$ acceptance range (FWHM). The typical K^-/π^- ratio was 1.4 with the K^- flux of 1.0×10^6/spill. This high purity was achieved by two-stage electrostatic separators (E1 and E2), steering dipoles (CM1-4) and, mass slits (MS1 and MS2). The electrostatic separators were operated with ± 300 kV on the anode and cathode plates which are 450 cm long, 39 cm wide, and 10 cm apart. The final focus of the beam line was 31.4 m away from the production target. The parameters of the beam line are summarized in Table 2.1.

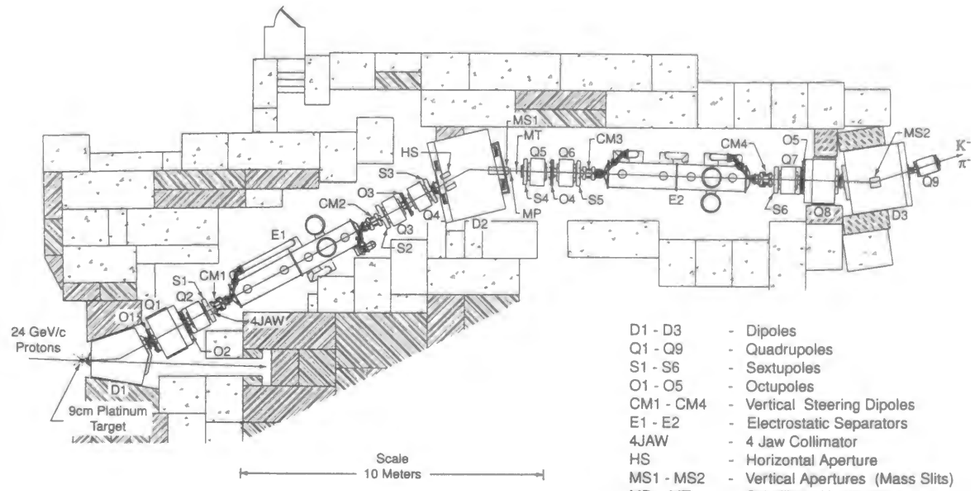

Figure 2.3: Schematic top view of the BNL-AGS D6 beam line.

Table 2.1: Operation parameters of the BNL-AGS D6 beam line.

Momentum	1.8 GeV/c
Target(length×width×hight)	$9 \times 0.7 \times 1.0$ cm platinum
Central production angle	5°
Momentum acceptance(FWHM)	$\pm 3\%$
Separators(E1&E2)	600 kV, 4.5 m long (each), 10 cm gap
Final Focus	
Horizontal image size (rms)	1.7 cm
Vertical image size (rms)	0.24 cm
Kaon flux. $K^-/8 \times 10^{12}$ protons	1.0×10^6/spill
K^-/π^- ratio	1.4

2.3 Diamond target

At the final focus of the beam line, a diamond target shown in Figure 2.4 was placed. It was composed of $1 \times 1 \times 0.1$ cm^3 wafers of industrial diamond, made by a chemical-vapor-deposition (CVD) process, stacked and epoxied together. The total dimension was 8 cm wide, 1 cm high, and 5 cm long with the density of 3.30 g/cm^3, which is 94% of that of the diamond crystal[1]. The more details on the target fabrication can be found in Ref. [120].

The primary function of the target was to obtain the (K^-, K^+) reactions which lead not only the Ξ^- production but also the direct production of S=−2 nuclear systems. Another function was to degrade the Ξ^- and bring it to rest in order to induce the atomic capture of Ξ^-. A small mass number ($A = 12$) and a high density of diamond provides a large advantage to the latter function. According to the previous experiment at KEK, the forward-angle cross section of the quasi-free (K^-, K^+) reaction scales by $A^{0.38}$ in the momentum region where the Ξ^- production is dominant [121]. Nuclear targets with a small mass number are favorable for obtaining a large Ξ^- yield owing to the above A dependence. Diamond has the highest density among target materials of the low mass number nuclei, and thus can stop short-lived particles such as Ξ^- very effectively. Also the (K^-, K^+) reaction on carbon nuclei has been well studied in the previous experiments [74, 78, 121]. This is important for making a Monte Carlo simulation to estimate the number of stopped Ξ^-'s, which is reported in Section 3.11.

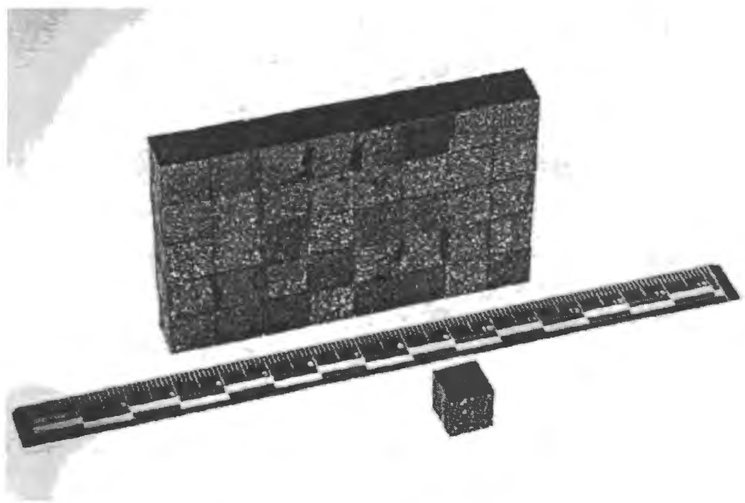

Figure 2.4: Photograph of the diamond target.

[1]The density of pure diamond crystal is 3.51 g/cm^3

2.4 Spectrometer magnet

A large-aperture dipole magnet was installed in the spectrometer at the end of the D6 beam line for the purpose of the momentum analysis of outgoing particles. The pole size was 48 inch wide and 48 inch deep with an 80 cm gap. Therefore it was called "48D48". Since the field direction was horizontal, particles were bent vertically. We operated it with the central field strength of 1.4 Tesla during the experiment. The magnetic field strength (B_x) as a function of the z position at $x = y = 0$ is shown in Figure 2.5. Here, the origin corresponds to the center of the magnet; z is the beam direction; x and y are horizontal and vertical directions perpendicular to the beam axis. Each component of the field strength inside the magnet aperture was measured to produce the field map for particle tracking. The measurement was done using hole probes with the accuracy of 2.54 cm in the z direction and 2.0 cm in the x and y directions. Also, a large plastic bag filled with helium gas was located inside the pole gap in order to reduce multiple scatterings by air.

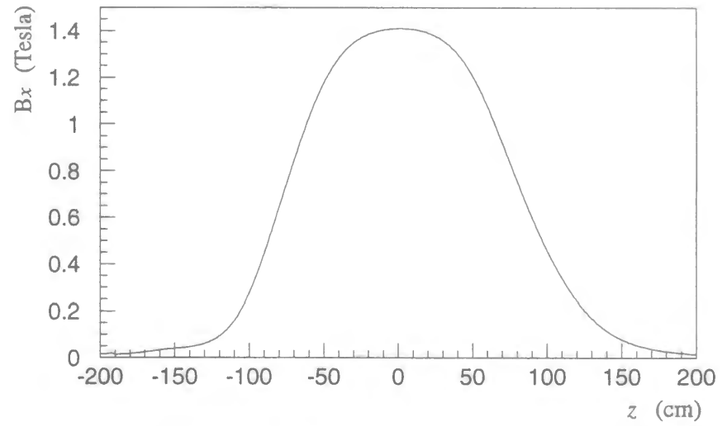

Figure 2.5: Magnetic field strength (B_x) as a function of the z position at $x = y = 0$.

2.5 Scintillator hodoscopes

In order to obtain the timing information and determine the rough location which particles passed through, several segmented scintillation counters were used. We called them scintillator hodoscopes. The material which we used was BC408 plastic scintillator made by Bicron for all hodoscopes. Photomultiplier tubes (PMTs) were coupled to each element of the scintillator hodoscopes to detect scintillation photons. In all hodoscopes except one, PMTs were coupled to both ends of each element, while PMTs were coupled to only one side of elements of MP, which is described in the next paragraph. Table 2.2 is a summary of the specifications.

Table 2.2: Specifications of the scintillator hodoscopes. The orientation is indicated by the direction of hodoscope slats (V: vertical, H: horizontal).

Hodoscope	Orientation	Dimension of one element[a] (cm^3)	Number of elements	PMT type
MP	V	1.5 × 0.7 × 0.3	72	R647-01
MT	V	1.5 × 3.7 × 0.6	9	RCA8575
IT	V	3.0 × 2.5 × 1.3	4	RCA8575
FP	H	24.0 × 1.5 × 0.4	16	H3167
BP	V	180.0 × 21.0 × 1.0	6	XP2262
BT	H	200.0 × 8.5 × 5.0	40	H1949

[a]length × width × thickness (cm^3)

Two vertical-segmented hodoscopes MP and MT were placed just downstream of the D2 dipole magnet in the beam line. The number of elements were 72 and 9 for MP and MT respectively. The beam momentum was well-dispersed horizontally at this position, and thus MP helped to determine the momentum by measurement of the horizontal position with its fine segmentation. On the other hand, the time-of-flight of incident particles was measured by the relative timing of MT to IT. Also the accidental hits were suppressed by requiring the position consistency of MP and MT.

A four-element hodoscope IT was located upstream of the target. The timing of IT was used as the standard of the start time of all TDC's and all online triggers. The time resolution was evaluated to be 60 ps (r.m.s.).

A sixteen-element hodoscope FP and a six-element hodoscope BP were used to detect scattered particles for the purpose of making the hardware triggers and also defining the spectrometer acceptance. The hodoscope FP was positioned downstream of the target and upstream of the 48D48 spectrometer magnet, while BP was placed downstream of 48D48. Since the elements of FP were oriented horizontally, the rough measurement of the scattering angle (θ_y) was possible. This information was utilized in the matrix coincidence trigger, which was one of the hardware triggers and is described in Section 2.10. Also the elements from #13 through #16 were used to veto the noninteracting beam particles.

At the end of the spectrometer, a scintillator hodoscope BT was installed to measure the time-of-flight of outgoing particles. It consisted of forty scintillator bars with dimensions 200.0 cm long, 8.5 cm wide, and 5.0 cm thick. The total active area was 200 cm × 320 cm. Since the high resolution of timing was required in this detector, fast-response PMTs (Hamamatsu H1949) were used for the light collection, and the signals were processed by constant fraction discriminators. The intrinsic time resolution was achieved at 150 ps (r.m.s.). The details of BT can be found in Ref. [122].

2.6 Drift chambers

The trajectories of incident and outgoing particles were measured with the drift chambers. This information was used for determination of the bending angle in the spectrometer magnet and the path length of particles. Table 2.3 summarizes the parameters of the drift chambers each of which is described below. The gas mixture of 77% argon, 20% isobutane, and 3% methylal was used for all the drift chambers.

We had three identical drift chambers ID1-3 upstream of the target. Each chamber consisted of three units of a double-plane structure. Namely, one plane and another plane whose wire alignment was shifted by a half wire spacing made one unit. This was for resolving the left-right ambiguity. The number of sense wires in one plane was 24 and the wire spacing was 5.08 mm. Since the beam particles were momentum-dispersed in the horizontal direction because of the horizontal bending in the beam line dipoles (D2 and D3), the x position measurement was important to analyze the momentum. Therefore the wires were aligned in the orientation of u-u', v-v', and x-x' in the hexagonal active area, where the planes labeled by prime (u', v', and x') stand for the ones shifted by a half wire spacing.

For the purpose of measuring the tracks of outgoing particles which entered the 48D48 dipole magnet, three drift chambers FD0-2 were placed downstream of the target and upstream of 48D48. The drift chambers FD1 and FD2 were identical, and they had the same structure as that of ID1-3 except the wire orientation and the size. Unlike the situation at the beam line, particles were bent vertically in the spectrometer. The wire orientation was hence u-u', v-v', and y-y'. The size of FD1 and FD2 was basically scaled up by a factor of two compared with the ID chambers. They had 48 sense wires in one plane with 5.08 mm wire spacing. The drift chamber FD0 was additionally installed just after the target in order to obtain the better z vertex resolution by improving the y position measurement. It consisted of only one pair of y-y' planes having the same number of wires and the same wire spacing as those of FD1 and FD2.

A four-plane drift chamber FD3 was located inside the 48D48 magnet aperture. This chamber helped us achieve the better track fitting combined with the field map of the magnet. The plane elements were u, y, y', and v each of which had 64 sense wires with 12.7 mm wire spacing. Another important role of this chamber was to provide the position information to not only the usual data stream but also the second-level trigger that is described in section 2.10.

Downstream of the 48D48 magnet, two large drift chambers BD1 and BD2 were placed so as to detect the particle trajectory after a bent by the magnet. The number of planes on BD1 was four with the wire orientation of y, u, v, and y', whereas that on BD2 was five due to an addition of the v' plane. The active area was a square window that was 114.0 cm wide and 214.0 cm high for both chambers. The number of wires was 112 for the y and y' planes and 128 for the u and v planes. The neighboring sense wires were 20.0 mm apart.

In order to make the particle tracking, the microstrip gas chambers (MSGCs) were also installed (IM1, FM1, and FM2) as well as the drift chambers. However, the data from the MSGCs were not used in the analysis reported here due to the low efficiency. The details

on the MSGCs are described in Appendix B.

Table 2.3: Parameters of the drift chambers.

	Plane	Orientation	Sense wire		Active area	Resolution
			spacing(mm)	# of wires	(X × Y cm^2)	(σ mm)
ID1	u-u'	120°	5.08	24×2	12.2×10.6	0.2
	v-v'	60°	5.08	24×2		
	x-x'	0°	5.08	24×2		
ID2	u-u'	120°	5.08	24×2	12.2×10.6	0.2
	v-v'	60°	5.08	24×2		
	x-x'	0°	5.08	24×2		
ID3	u-u'	120°	5.08	24×2	12.2×10.6	0.2
	v-v'	60°	5.08	24×2		
	x-x'	0°	5.08	24×2		
FD0	y-y'	90°	5.08	24×2	12.2×10.6	0.2
FD1	u-u'	210°	5.08	48×2	21.2×24.4	0.2
	v-v'	150°	5.08	48×2		
	y-y'	90°	5.08	48×2		
FD2	u-u'	210°	5.08	48×2	21.2×24.4	0.2
	v-v'	150°	5.08	48×2		
	y-y'	90°	5.08	48×2		
FD3	u	150°	12.7	64	45.7×81.3	0.3
	y	90°	12.7	64		
	y'	90°	12.7	64		
	v	30°	12.7	64		
BD1	y	90°	20.0	112	114.0×214.0	0.4
	u	120°	20.0	128		
	v	60°	20.0	128		
	y'	90°	20.0	112		
BD2	y	90°	20.0	112	114.0×214.0	0.4
	u	120°	20.0	128		
	v	60°	20.0	128		
	y'	90°	20.0	112		
	v'	60°	20.0	128		

2.7 Aerogel Čerenkov counters

Since the (K^-, K^+) reaction is a rare event, it is quite important to reduce backgrounds at the hardware level in order to increase the efficiency. Most of backgrounds in the incident channel were π^-'s, while those in the outgoing channel were π^+'s and protons. We used aerogel Čerenkov counters to discriminate pions and to suppress protons. The chemical component of the aerogel was silicon-dioxide (SiO_2). By setting a proper refractive index, particles were discriminated in terms of their velocity difference. For the particle of which velocity is larger than c/n, where n is the refractive index, the aerogel emits Čerenkov light. Photomultiplier tubes (PMTs) were used to collect photons. Since the momentum of incident particles was almost equal and also that of outgoing particles was not so dispersed due to the limited spectrometer acceptance, the velocity difference roughly reflected the mass difference.

In the incident channel, an aerogel Čerenkov counter IC, of which radiators had the refractive index of 1.029, was positioned between ID2 and ID3 in order to identify K^-'s. Concerning the outgoing channel, aerogel Čerenkov counters FC and FC0 were installed upstream of the 48D48 magnet and BC was located downstream of the last drift chamber, BD2. The role of FC and BC was to discriminate K^+'s from π^+'s, and thus the refractive indices of radiators were 1.037 and 1.04 respectively. However, FC0 had radiators of which refractive index was 1.121, and it functioned to suppress protons of which momenta were less than 1.85 GeV/c mainly caused from inelastic and a part of elastic K^-p scattering. However, protons elastically-scattered in the forward direction of the center-of-mass frame were not rejected due to the high momentum. Figures 2.6 - 2.9 represent schematic views of the above counters, and the specifications of each counter are summarized in Table 2.4. The inner faces of aerogel containers of each counter were coated by highly reflective white sheets (Millipore for IC, FC0, and BC; Goretex for FC) in order to suppress light absorption. Moreover, aluminized mylar mirrors were equipped in IC and BC to guide photons to PMTs as shown in Figures 2.6 and 2.9. Since IC and FC were in-beam counters and thus they were operated under high count rates, additionally boosting high voltages were applied to the last several dynodes in order to maintain the stable pulse height of output signals.

Generally, the aerogel has a nature of hygroscopicity, and the nitrogen gas flow is needed to keep its quality. However, due to the recent efforts, the hydrophobic aerogel has become available [124], which allows us easier maintenance. The nitrogen gas flowing is not necessary any more. We have upgraded IC and FC for this experiment by replacing the old radiators to the new hydrophobic ones which had been fabricated at KEK. In addition, fine-mesh PMTs (Hamamatsu H6155-01), which keep a good performance even in the operation under high magnetic fields, were introduced to FC in this upgrade.

The efficiencies of IC, FC, and BC were measured by exposing the radiators to the π^- and K^- beams. The beam momentum was set to be 1.8 GeV/c for IC and 1.4 GeV/c for FC and BC considering their thresholds. The ADC spectra of these counters are shown in Figure 2.10. The obtained efficiencies for pion rejection were 99.4 %, 99.9 %, and 95.0 % for IC, FC, and BC, respectively. Since the new radiator was also developed in respect

of transparency, the light yield has become larger compared with the old one, and this brought us good performance in IC and FC. As for FC0, scattered protons and kaons were utilized for the efficiency estimation. Due to less transparency of the radiator, the position dependence of the efficiency was found (~98% near the PMT input windows, ~50% deeply inside). This dependence was taken into account in estimating the total K^+ detection efficiency of the spectrometer system, which is described later. Figure 2.10(d) shows the ADC spectra of 1.7 GeV/c protons and 1.2 GeV/c K^+'s which hit the top two aerogel blocks in FC0 (see Figure 2.8). The corresponding efficiencies are 7% for 1.7 GeV/c protons and 93% for 1.2 GeV/c K^+'s, respectively.

	IC	FC	BC	FC0
Effective area (X×Y cm^2)	10×5.8	23×23	126×189	13×14.4
Total thickness (cm)	6.0	8.0	9.0	3.6
Dimension of a block (X×Y×Z cm^3)	10 × 5.8 × 2	11.5 × 11.5 × 2	21 × 21 × 3	13 × 1.8 × 3.6
Number of block	3	16	162(= 6 × 9 × 3)	8
Refractive index (n)	1.029	1.037	1.04	1.121
Threshold momentum for $\pi/K/p$ (GeV/c)	0.58/2.04/3.87	0.51/1.80/3.42	0.49/1.73/3.28	0.28/0.97/1.85
PMT type	Hamamatsu R1250	Hamamatsu H6155-01	Burle 8854	Hamamatsu H1161Q

Table 2.4: Parameters of aerogel Čerenkov counters.

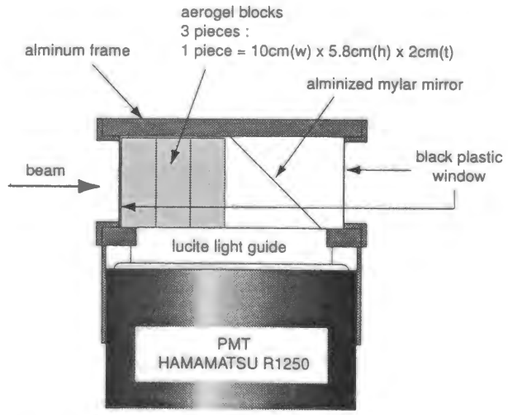

Figure 2.6: Schematic drawing of IC.

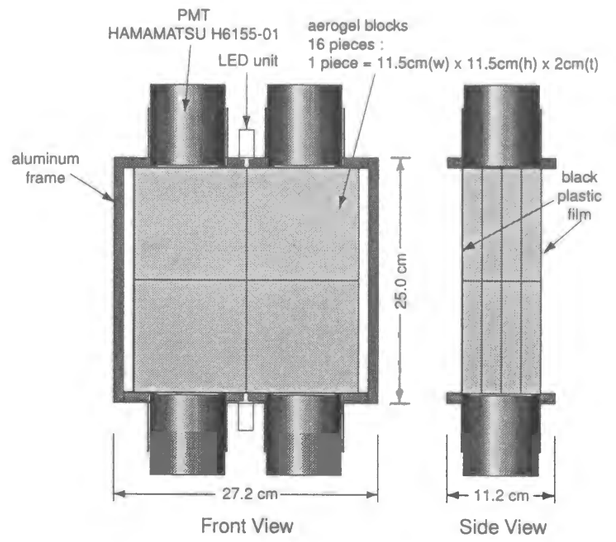

Figure 2.7: Schematic drawing of FC.

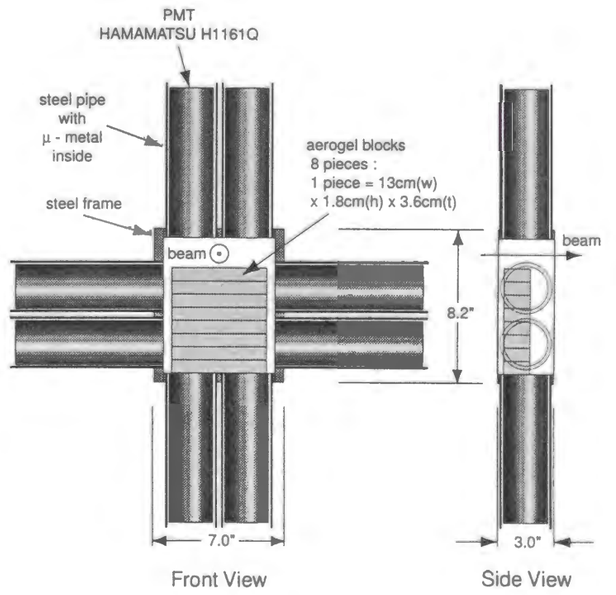

Figure 2.8: Schematic drawing of FC0.

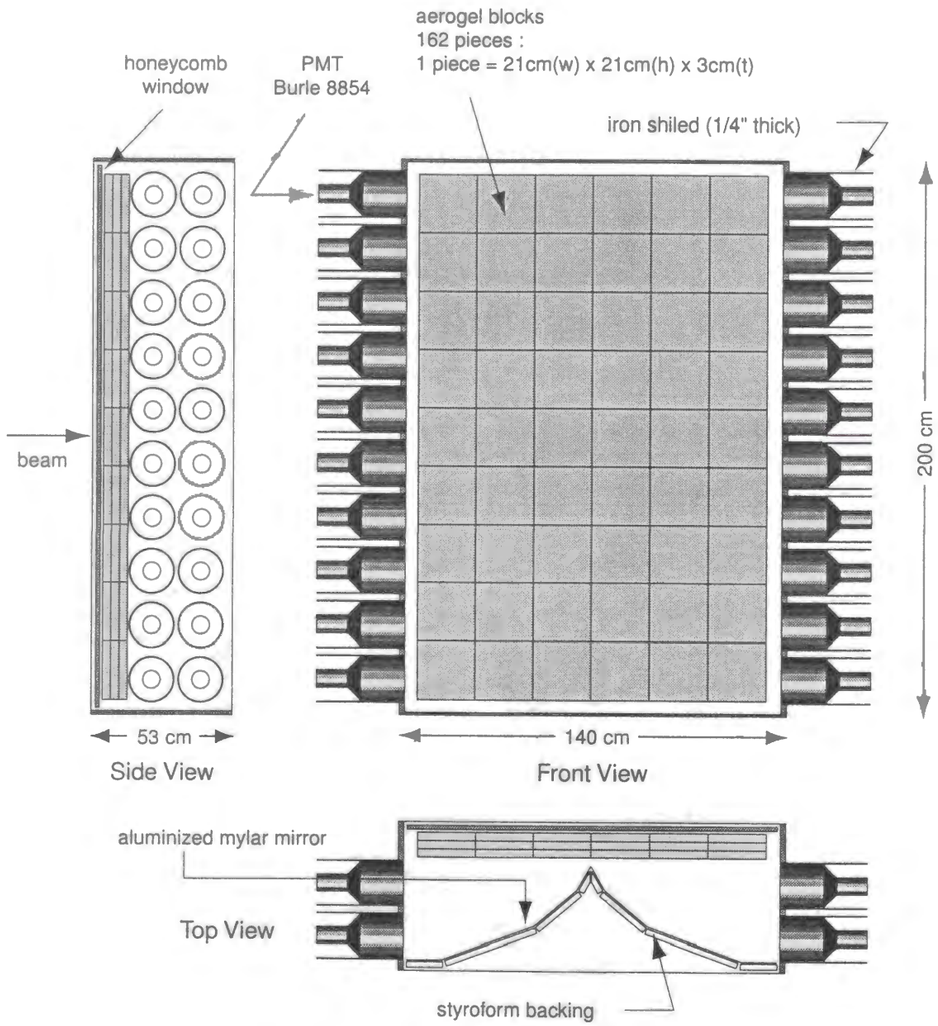

Figure 2.9: Schematic drawing of BC.

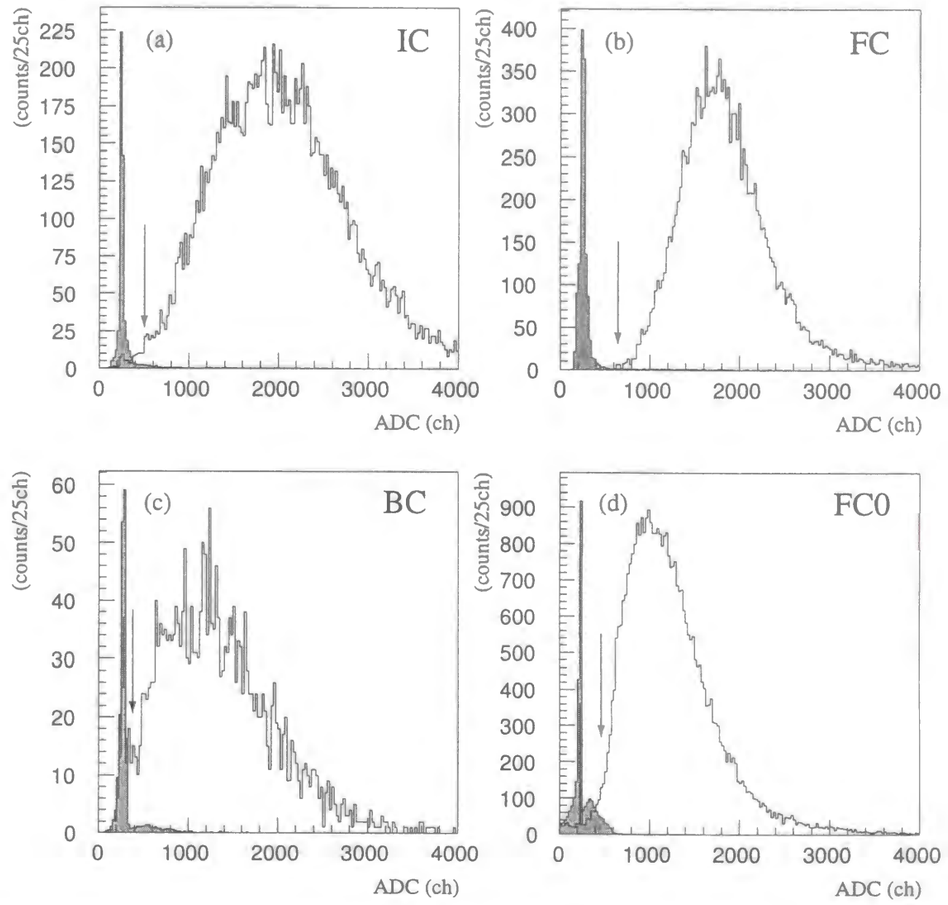

Figure 2.10: ADC spectra of aerogel Čerenkov counters. For the efficiency evaluation, the π^- and K^- beams were used for IC (a), FC (b), and BC (c). The open histograms show the response of π^-, while the shaded ones show that of K^-. For FC0 (d), the open and shaded histogram correspond to K^+ and the scattered protons respectively (see the text). The shaded histograms were scaled down for proper superimposition. The arrows indicate the positions of the discriminator thresholds.

2.8 Neutron counter arrays

On both right and left sides of the diamond target, we placed neutron counter arrays with a large solid angle (totaling $\sim$ 0.21 of 4π) in order to detect neutrons which are signals of the H decay and the ${}^{12}_{\Lambda\Lambda}$B production. Each array was composed of fifty plastic scintillator logs (RN and LN), each of which was 5.08 cm thick, 15.24 cm wide, and 182.88 cm high. Charged particles resulting from nuclear interaction such as n-p scattering and n-^{12}C interaction produced signals of the neutron hits. The inner side of each array facing to the diamond target was covered by 0.95 cm thick plastic scintillators (RV and LV), which were used to veto charged particles. Bicron BC408 was used for all elements. Figure 2.11 represents the geometric configuration of the neutron counter arrays. In order to get rid of inefficient areas, each layer of RN and LN was aligned with a shift of a half-element to the neighboring layers, and the elements of RV and LV were slightly overlapped.

Two PMTs (Amperex 2262 for RN and LN, RCA 8575 for RV and LV) were coupled to both ends of each scintillator for light detection. The signals from these PMTs were split into two streams for ADCs and TDCs. Constant-fraction discriminators (CFDs) were used to provide timing pulses for TDCs. The ADC information was converted into the energy deposit in the scintillator logs, while the mean time and the time difference of a pair of PMTs at both ends of each element determined the time-of-flight and the vertical hit position, respectively. The resolution studies were performed using cosmic rays and a

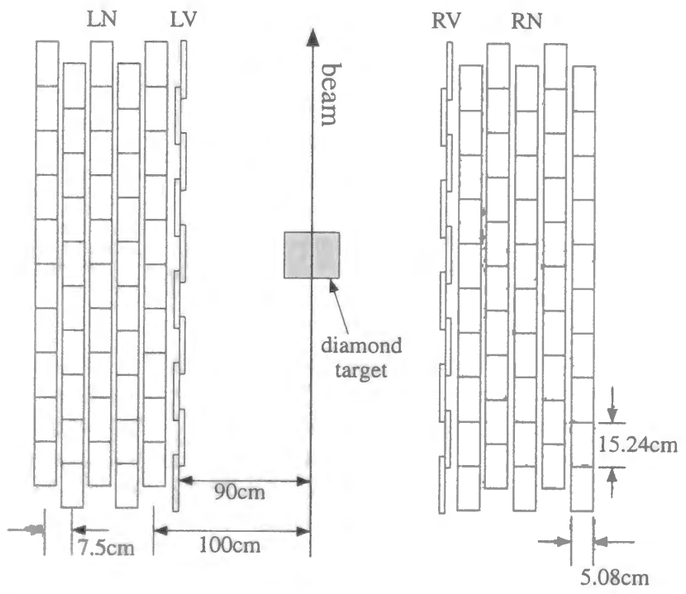

Figure 2.11: Schematic top view of the neutron counter arrays.

laser flasher, which are described later in detail.

The neutron detection efficiency was evaluated with the DEMONS [125, 126] code, which incorporates the simulation of nuclear interactions in the scintillator material. Figure 2.12 shows the obtained efficiencies of neutron detection for various thresholds of energy deposit as a function of neutron kinetic energy. Note that the acceptance of the counters from the target was included in this estimation. The unit "MeVee (MeV electron-equivalent)" used to represent the energy deposit in the figure stands for the light output which is equivalent to the energy deposit of an electron by a unit of MeV. The efficiency curves change much at low energies, whereas they become flat at the kinetic energies of larger than 100 MeV.

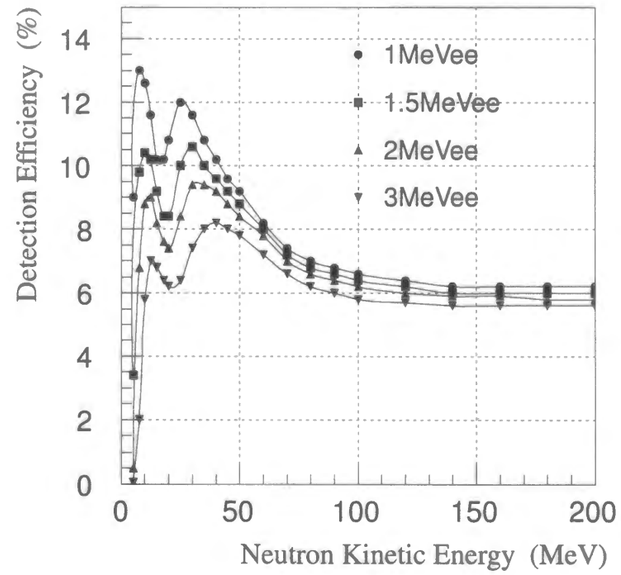

Figure 2.12: Neutron detection efficiency calculated by the DEMONS code as a function of the neutron kinetic energy. The efficiencies for the energy-deposit threshold of 1 MeVee, 1.5 MeVee, 2 MeVee, and 3 MeVee are shown.

The comparison between the simulation and experimental data was done by using neutrons resulting from $(\Sigma^-, p)_{atom} \to \Lambda + n$. The product of the Σ^- stopping rate on liquid hydrogen and the neutron detection efficiency was investigated by counting the number of detected neutrons. The details on the analysis can be found in Ref. [80]. Although some dependence on the K^+ angle cut was reported, it was found that the measured value was comparable to or up to twice larger than the calculated value.

2.9 Scintillating fiber (SCIFI) detector

Above and below the target, two identical scintillating fiber (SCIFI) detectors were installed to observe tracks of charged decay products. One unit of this detector system consisted of a SCIFI block, two sets of an image intensifier tube (IIT) and a CCD camera. The details of each component are described below.

2.9.1 Scintillating fiber (SCIFI) block

The scintillating fiber (SCIFI) is a kind of an optical fiber which gives scintillation light due to a hit of a charged particle. It consists of a polystyrene core and an acrylic clad to emit and transmit photons. We used Bicron BCF-12 scintillating fibers for the experiment. The wave length of emitted photons peaked at 435 nm, and the attenuation length was 2.2 m. Each fiber had a 1 mm $\times$ 1 mm square cross section in which 2$\times$20 μm-thick cladding was included. Also it was coated with white extra-mural-absorber (EMA) to eliminate crosstalk. Parameters of the scintillating fiber are listed in Table 2.5.

Fiber	Emission color	Emission peak (nm)	Decay time (ns)	Attenuation length (m)	Number of photons/MeV
BCF-12	blue	435	3.2	2.2	~8000

	Material	Refractive index	Density (g/cm^3)	Thickness (μm)
core	polystyrene $(CH)_n$	1.60	1.05	960
clad	acrylic $(C_5H_8O_2)_n$	1.49	1.20	2$\times$20t

Table 2.5: Scintillating fiber parameters.

The SCIFI block was fabricated by stacking SCIFI sheets alternately in two orthogonal directions. Scintillating fibers described above were arranged in a "boomerang" shape to compose each SCIFI sheet. BC-600 optical cement was used to glue fibers. A schematic view of the fabricated SCIFI block is shown in Figure 2.13(a). The block was 12 cm long in the beam direction by 7 cm across at the base. The overlapped section of the SCIFI sheets in two orientation made a three-dimensional active area. The total number of fibers in a block was about 7600 in a total of 100 sheets. The sheet pitch was 1.2 mm. The body of the SCIFI block was supported by aluminum frames in order to keep its shape. This characteristic shape was devised to open the space between the diamond target and the neutron counter arrays described in former sections. The geometric layout of the blocks relative to the diamond target in the experimental installation is presented in Figure 2.13(b). The bases of the SCIFI blocks were away from the diamond-target center by 12.3 mm for the upper block and 15.7 mm for the lower block. The particle tracks were projected onto u-v directions as photon images and read out at both ends of extended fiber arms (see Figure 2.13(a)).

2.9.2 Image intensifier tube (IIT)

The projected photon image at the end of each arm of the SCIFI block was viewed by an image intensifier tube (IIT). This tube multiplied the number of photons keeping their topological information. Namely an optical image was amplified in terms of its brightness. The IIT used in our experiment had a three-stage structure, as shown in Figures 2.14 and 2.15, each of which consisted of a photocathode, an electron accelerator or multiplier, and a phosphor on which the source was imaged. One SCIFI block was coupled to Hamamatsu C4693 and Delft PP0040. These two types of IIT had almost similar characteristics and performance except for the diameter of input and output windows. Table 2.6 represents the specifications of the two types of IIT. Since we used two SCIFI blocks over and below the target as seen in Figure 2.13(b), we utilized four IITs in total.

The first stage of the IIT electro-statically accelerated the photoelectrons with cathode-to-anode voltage of +20 kV. Also the focusing electrodes arranging inside compressed the spatial configuration of the electrons. Then the accelerated electrons struck the phosphor at the end of the stage to be converted to the optical image which was an input of the second stage.

The second and the third stages had micro-channel plates (MCP) for photon multiplication. By applying pulse voltage, the gate operation was possible. For the Hamamatsu IIT, the pulse voltage was applied between the input and output of the MCP. The MCP input was always at the ground level, and the MCP output voltage was +800 V at gate

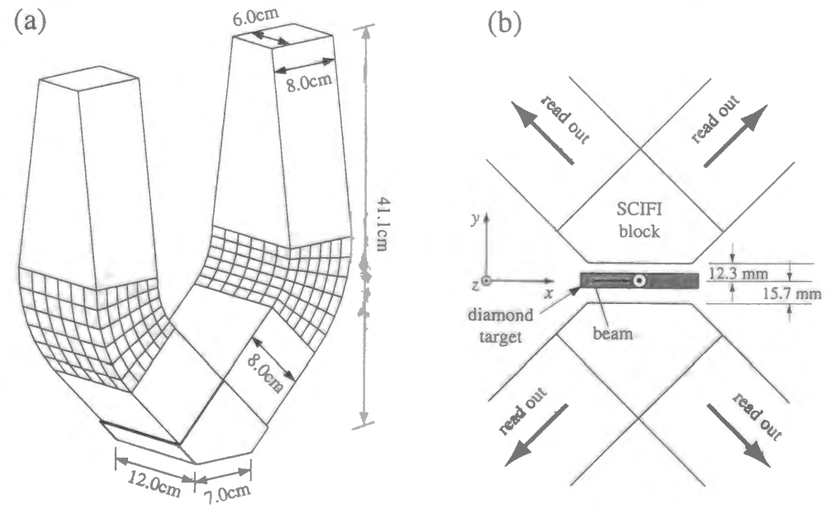

Figure 2.13: Scintillating fiber (SCIFI) block used in the experiment. (a) : Schematic view of one unit. (b) : Front view of the geometric layout of the blocks relative to the diamond target.

open and 0 V at gate closed. The last phosphor of each stage was kept at +4 kV with respect to the MCP output in order to accelerate the multiplied electrons. On the other hand, the pulse voltage was applied between the photo cathode and the MCP in the Delft IIT. The voltages on the MCP input and output were fixed at −750 V and 0 V respectively, while the voltage applied to the cathode was −200 V to open the gate and +50 V to close it compared to the MCP input. The phosphor voltage for electron acceleration was +5.8 kV. The voltages applied to the MCPs are summarized in Table 2.7. The first- and second-level triggers, which are described in Section 2.10, gated the second and the third stage respectively in the experiment in order to obtain 'snapshots' in coincidence with the (K^-, K^+) events. In this gating scheme, phosphors at the end of each stage functioned as an image memory while making a trigger decision. P-24 phosphor which has decay time of 2.4 μs was used in the first stage, while P-20 phosphor of which decay time is 50 μs was used in the second and the third stage. The second-stage gate widths were 3 μs and 2 μs for the Hamamatsu and Delft IITs respectively, and the third-stage gate widths were 150 μs for both of the Hamamatsu and Delft IITs.

It should be noted that the output images of the IITs were easily distorted by the magnetic field of the spectrometer because the photo-electrons were accelerated in the focusing electric field at the first stage. Therefore, the IITs were put into the iron boxes made of 1/2″ thick iron plates, as shown in Figure 2.16, after being surrounded by the μ-metal shields on their sides.

We have found that images were not intensified by IITs at higher trigger rates than 60 Hz for the Hamamatsu one and 100 Hz for the Delft one. In order to keep the image quality, trigger intervals of the IITs were kept larger than 15 ms by applying additional self vetoes. By the later investigation, it turned out that the power supplies for gate pulses could not keep the voltage at higher rates than the values shown above.

IIT type	Photon gain		Phosphor type		Input and output window diameter (mm)	
	Stage 1	Stages 2,3	Stage 1	Stages 2,3	Stage 1	Stages 2,3
Hamamatsu C4693	10 [a]	3×10^3 [b]	P-24	P-20	100, 25	25, 25
Delft PP0040	$\geq$8 [c]	10^3 [d]	P-24	P-20	80, 16	16, 16

Table 2.6: Specifications of the image intensifier tubes.

[a] At cathode-to-anode voltage = +20kV
[b] At MCP voltage = +900V
[c] At cathode-to-anode voltage = +20kV
[d] At MCP voltage = +750V

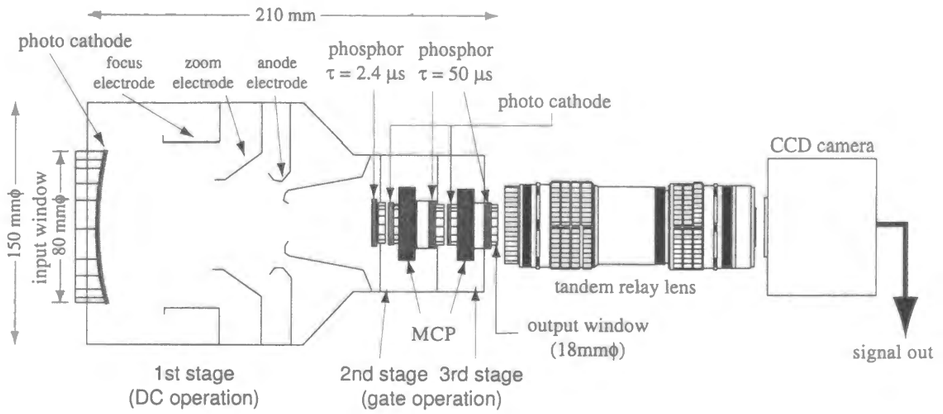

Figure 2.14: Schematic view of the Delft PP0040 image intensifier - CCD camera system.

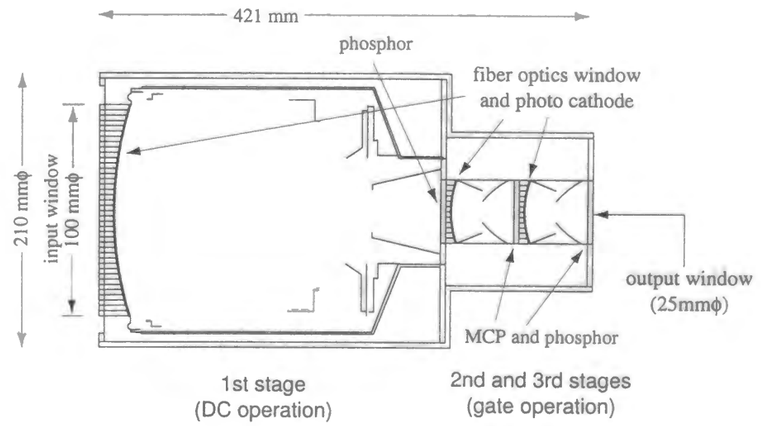

Figure 2.15: Schematic view of the Hamamatsu C4693 image intensifier. The same relay lens and CCD camera were mounted in the rear of the last phosphor.

Electrode	Applied voltage			
	Hamamatsu C4693		Delft PP0040	
	Gate open	Gate closed	Gate open	Gate closed
Photo cathode	-1.7 kV		$V_{\text{MCP-in}} - 250$ V	$V_{\text{MCP-in}} + 50$ V
MCP-in	0		-750 V	
MCP-out	+900 V	0	0	
Phosphor	$V_{\text{MCP-out}} + 4$ kV		+5.8 kV	

Table 2.7: List of the voltages applied to the MCP.

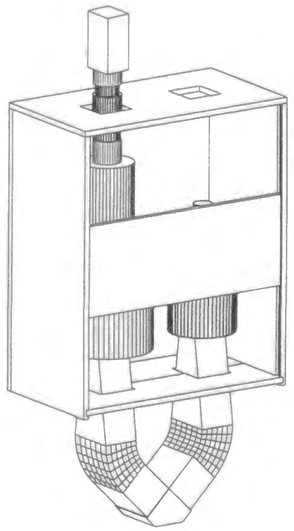

Figure 2.16: Schematic view of the SCIFI block and the IITs equipped with the magnetic shield.

2.9.3 CCD camera

Output images of the IIT projected on the last phosphor window were focused on the CCD image sensor of Dalsa CA-D1 CCD camera via the optical lens system. The size of the CCD chip was 4.096 $\times$ 4.096 mm^2, in which 256$\times$256 pixels were built in. The camera was operated by the internal clock at the read-out rate of 203 frames per second. The clock of each camera was reset by the external sync pulse at the end of every spill in order to align the timing of all the cameras. Optical images on the CCD were processed into digital output signals containing the vertical- and horizontal-pixel addresses and the brightness with 8-bit data for each. Also we have modified the camera to output ECL signals in order to transfer data for a long distance all the way from the experimental area to the counting house, while the commercial product had an only TTL output. The output signals were sent to the module to compress data by trimming off the pixel information

of which brightness was lower than the threshold. The threshold was optimized at the level just over the thermal noise. Then the compressed data only in coincidence with the second-level triggers were transferred to the memory modules on the VME data acquisition system.

As a total system of the SCIFI detector, we found that a 1 mm $\times$ 1 mm square fiber corresponded to an image on the CCD of a square with sides of 2.0 $\sim$ 2.2 pixels for the system of the Hamamatsu IIT and 2.3 $\sim$ 2.5 pixels for that of the Delft one. Figure 2.17 shows an example of the obtained image data representing a typical sequential decay of Ξ^- ($\Xi^- \to \Lambda + \pi^-$, $\Lambda \to p + \pi^-$).

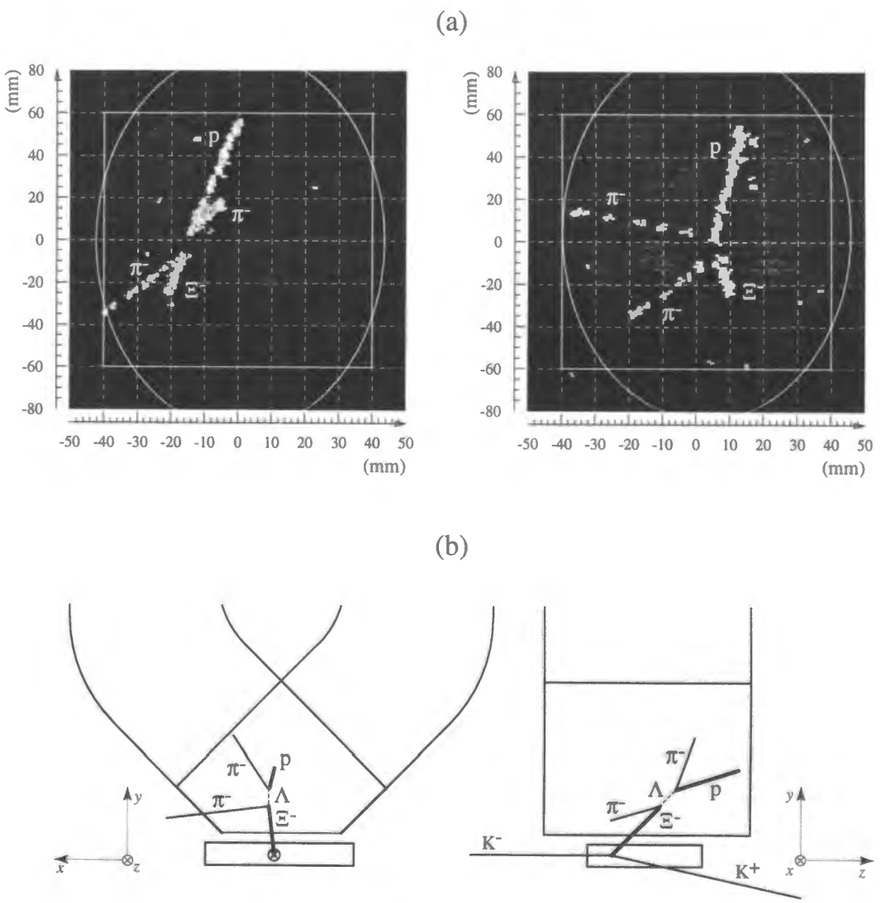

Figure 2.17: (a): Example of the image data obtained by the SCIFI detectors. A sequential decay of Ξ^- ($\Xi^- \to \Lambda + \pi^-$, $\Lambda \to p + \pi^-$) was observed. (b): Schematic view of the reaction of (a).

2.10 Triggers

In order to obtain the data of interest efficiently under the limited data-acquisition rate, the detected events were first assorted to various kinds of categories in online mainly in terms of the incident- and outgoing-particle species and their combinations. The categorization was achieved by a set of "first-level triggers" which were formed by the logical combinations of fast signals from the scintillator hodoscopes and the aerogel Čerenkov counters. After this first-level decision, the events categorized as (K^-, K^+), which is of our most interest, were further sent to the second-level decision using an additional trigger logic ("second-level trigger") to make more efficient reduction of backgrounds which were mostly outgoing protons resulting from (K^-, p) scattering.

2.10.1 First-level triggers

In the first level decision, beam particles were categorized to K^- candidates and π^- candidates. The corresponding triggers were "KBeam" and "πBeam" respectively, defined by the status whether the IC aerogel Čerenkov counter had a hit or not in coincidence with a hit on the IT hodoscope as follows:

$$\mathrm{KBeam} = \mathrm{IT}^1_4 \otimes \overline{\mathrm{IC}}\,, \tag{2.1}$$
$$\pi\mathrm{Beam} = \mathrm{IT}^1_4 \otimes \mathrm{IC}\,, \tag{2.2}$$

where IT^1_4 means a logical OR of discriminated signals from four elements of IT. Similarly, "KScat" and "πScat" triggers were used to classify outgoing particles into K^+ candidates and π^+ candidates, which were defined as

$$\mathrm{KScat} = \mathrm{FP}^1_{12} \otimes \mathrm{BP}^1_6 \otimes \mathrm{FC0} \otimes \overline{(\mathrm{FC} \oplus \mathrm{BC})}\,, \tag{2.3}$$
$$\pi\mathrm{Scat} = \mathrm{FP}^1_{12} \otimes \mathrm{BP}^1_6 \otimes (\mathrm{FC} \oplus \mathrm{BC})\,, \tag{2.4}$$

where FP^1_{12} stands for a logical OR of discriminated signals from the FP element #1 to #12 among total 16 elements, while the element #13 to #16 were used to veto the noninteracting beam particles. BP^1_6 also means a logical OR of discriminated signals from six elements of BP. FC, FC0, and BC are discriminated signals of analog sum of all PMT channels in corresponding aerogel Čerenkov counters. Finally, reactions were defined by combining above triggers on beam and outgoing particles as follows:

$$\mathrm{KK} = \mathrm{KBeam} \otimes \mathrm{KScat}\,, \tag{2.5}$$
$$\mathrm{K}\pi = \mathrm{KBeam} \otimes \pi\mathrm{Scat}\,, \tag{2.6}$$
$$\pi\mathrm{K} = \pi\mathrm{Beam} \otimes \mathrm{KScat}\,, \tag{2.7}$$

which correspond to (K^-, K^+), (K^-, π^+), and (π^-, K^+), respectively. The trigger decision time was 420 ns. This includes 250 ns for the traveling time of the signals from the experimental area to the counting house and 170 ns for signal processing.

Independently from above definitions, another trigger which required only the hits on IT and BT was defined as

$$\mathrm{ITBT} = \mathrm{IT}^1_4 \otimes \mathrm{BT}^{17}_{24,28}\,, \tag{2.8}$$

where $\mathrm{BT}^{17}_{24,28}$ refers to a logical OR of the BT element #17 to #24 and #28. Since this trigger was the minimum-biased one, it was used for monitoring the experiment.

Since our primary purpose was to obtain (K^-, K^+) events, KK triggers were of our most interest. However, in order to monitor the experiment, events of other triggers were also recorded with certain prescaling factors. Table 2.8 summarizes the first-level triggers and Figure 2.18 shows a corresponding schematic chart except for ITBT. The typical rate for the KK trigger was about 810/spill, while the other triggers were prescaled to ∼10 events/spill for the sum of them. The live time of the data acquisition depended on the beam intensity. It was typically 75% at the K^- intensity of 1.0×10^6/spill, while 80% at that of 0.7×10^6/spill.

Trigger	Definition	Events	Typical trigger rate (/spill)	Prescale factor
KBeam	$\mathrm{IT}^1_4 \otimes \overline{\mathrm{IC}}$	incident K^-	1.0×10^6	8×10^5
πBeam	$\mathrm{IT}^1_4 \otimes \mathrm{IC}$	incident π^-	0.70×10^6	2×10^6
KScat	$\mathrm{FP}^1_{12} \otimes \mathrm{BP}^1_6 \otimes \mathrm{FC0} \otimes \overline{(\mathrm{FC} \oplus \mathrm{BC})}$	outgoing K^+	–	–
πScat	$\mathrm{FP}^1_{12} \otimes \mathrm{BP}^1_6 \otimes (\mathrm{FC} \oplus \mathrm{BC})$	outgoing π^+	–	–
KK	KBeam ⊗ KScat	(K^-, K^+)	810	1
Kπ	KBeam ⊗ πScat	(K^-, π^+)	2000	1×10^4
πK	πBeam ⊗ KScat	(π^-, K^+)	160	4×10^1
ITBT	$\mathrm{IT}^1_4 \otimes \mathrm{BT}^{17}_{24,28}$	minimum bias	3800	2×10^3

Table 2.8: Summary of the first-level triggers. KScat and πScat were not recorded on tapes. The values for the trigger rates are those before prescaling.

2.10.2 Second-level trigger

The events identified as KK by the first-level trigger still contained a large amount of backgrounds, most of which are outgoing protons resulting from (K^-, p) scattering. Although these protons were partially suppressed by the FC0 aerogel Čerenkov counter, fast protons with the momentum higher than the threshold, 1.85 GeV/c, fully remained in the sample. Hence, we introduced the second-level trigger for the purpose of more efficient proton suppression. The principle of this trigger was based on the particle-dependent correlations between trajectory and TOF. Figure 2.19 exhibits a schematic chart of the signal processing in the second-level trigger. Since the magnetic field inside the 48D48 was in the x-direction, the y-position of the particle trajectory at FD3 (the drift chamber in the 48D48 magnet aperture) and BT (the last TOF hodoscope) roughly determined the momentum and path

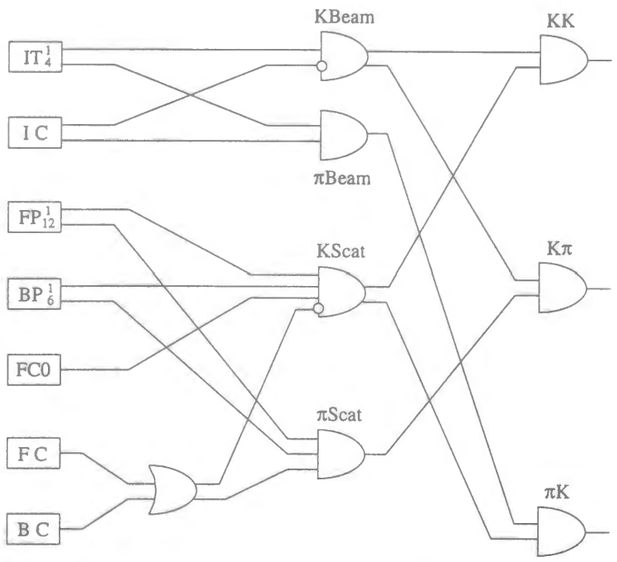

Figure 2.18: Schematic chart of the first-level triggers. ITBT is not shown here.

length by assuming the particles were originated from the diamond target. Particles with different masses result in different TOF in the condition of the same momentum and path length, and thus TOF cuts depending on the y-position of the trajectory at FD3 and BT will permit to suppress protons effectively without rejecting K^+'s. In practice, we used the TOF from IT to BT. The TOF difference between protons and K^+'s amount to 4.5 ns with momentum of 1.2 GeV/c. The y-position information at FD3 was provided as a 16-bit word (FD3 bits). As mentioned in Section 2.6, FD3 consisted of four planes, u-y-y'-v, with a wire spacing of 1.27 cm. The logical OR of the discriminated signals in group of six y-y' wires, three on each of y and y' planes, produced single-bit data. Each group of 6 wires covered 4.445 cm in the y direction. Since the BT scintillator logs were aligned in y, the log number represented the y-position at BT with the accuracy of 8 cm. By combining every BT log and FD3 bit, the possible trajectories were broken into a number of spaces, each of which was small enough to separate protons and K^+'s with TOF.

In this experiment, trigger decisions were required as quickly as possible to prevent the optical image on the IIT phosphor from fading out. We used the LeCroy Fast Encoding and Readout TDC (FERET) system consisting of three Fast Encoding Time-to-Charge Converters (TFC, LeCroy 4303), three Fast Encoding and Readout ADCs (FERA, LeCroy 4300B), and single FERA driver (LeCroy 4301) for measuring the IT-BT TOF. According to forty elements of BT, we utilized three sets of TFC and FERA; each set handled up to 16 inputs. This system provided the resolution of 50 ps/ch. A 16-bit output of the FERA module included 11 bits of TOF information and 4 bits of the substation number with single

bit indicating the header/data flag. Adding the station number of the FERA module and removing the least-significant-bit of the TOF information by signal reconfiguration with the external electronics, the FERA output were converted to the 16-bit data consisting of 10 bits of IT-BT TOF and 6 bits of BT log number. The converted data were next fed into the Memory Lookup Unit (MLU, LeCroy 2373) to obtain corresponding "acceptable FD3 bits". The MLU generates a 16-bit output word by regarding a 16-bit input word as an address of the internal memory. The combined data of IT-BT TOF and BT log number was used as the 16-bit input word here. Contents of the memory were downloaded in the beginning of the data acquisition. Then the "MLU accept" signal was created by making a logical AND of the "acceptable FD3 bits" and the real FD3 bits. Finally, the second-level trigger was produced from the "MLU accept" in a fixed time, 19 μs after the first-level decision. This was done in order to reduce fluctuation in intensity of the SCIFI image due to fading of the phosphor image on the IIT. In consequence of this trigger, the typical

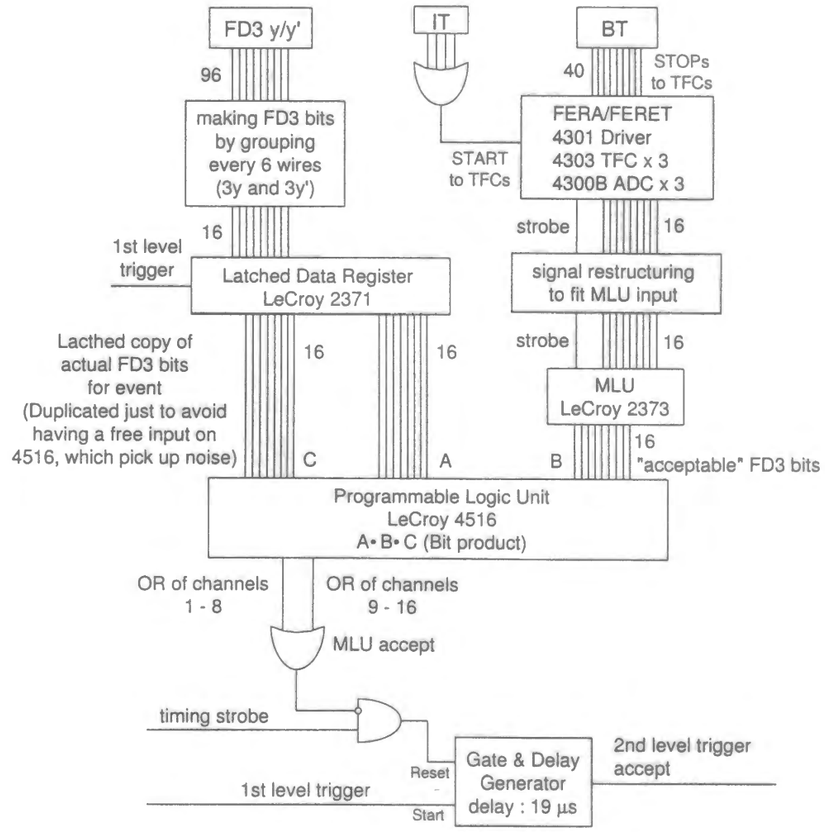

Figure 2.19: Schematic chart of the second-level trigger.

trigger rate was 65, where outgoing protons passing through the first-level KK trigger were suppressed by a factor of $8 \sim 10$; the efficiency for outgoing K^+'s was 95%.

2.10.3 Triggers for IIT

As described in Section 2.9.2, an IIT had a function of two-stage gate operation. Basically, the first- and second-level triggers mentioned in the previous sections were fed into gate inputs of the second and third stage of the IIT. However, in order to reduce the load on the phosphors, we have included several additional logics into the basic trigger algorithm only for the IIT triggers. A schematic signal chart of the triggers for IITs are shown in Figure 2.20.

In the first level, the basic trigger was KK. While the data acquisition was busy, triggers were vetoed and not sent to the IITs. The matrix coincidence logic was also utilized to reduce the trigger rates. This logic was produced by a matrix coincidence module which had two series of twelve inputs. Suppose these inputs are denoted as vectors $\boldsymbol{x}$ and $\boldsymbol{y}$, the definition of accept/reject decisions for every combination of (x_i, y_j) $_{i=1,12\ j=1,12}$ was possible by setting the dip-switches inside the module. The module generated the accept signal when any of the combination (x_i, y_j) was acceptable. We used the lower twelve elements of FP (#1 to #12) as $\boldsymbol{x}$, and twenty-four elements of BT (#14 to #37) as $\boldsymbol{y}$. Twenty-four channels of BT were covered by using two modules of the matrix coincidence

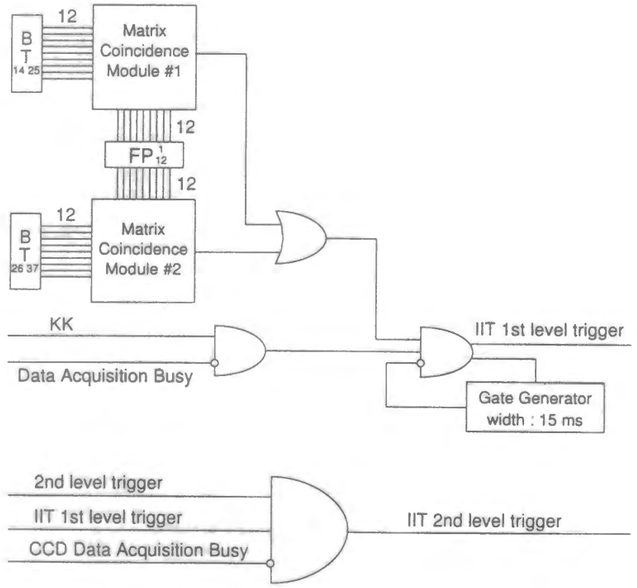

Figure 2.20: Schematic chart of the triggers for the IITs.

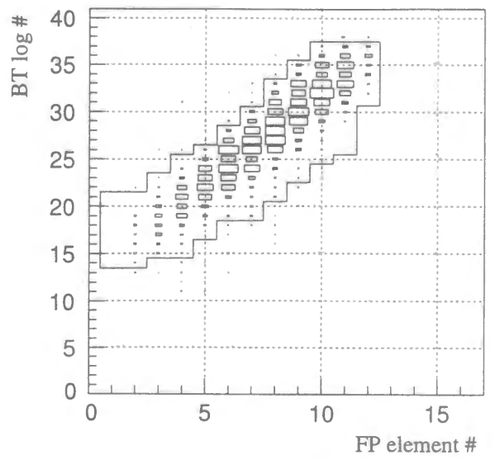

Figure 2.21: Correlation between the FP element number and the BT log number for K^+'s of $p_{K^+} > 1.1$ GeV/c. The region surrounded by a solid line was selected by the matrix coincidence logic.

logic. The selected FP and BT elements and the accept/reject decision of each combination were determined from the analysis of (K^-, K^+) events. Similarly to the second-level trigger described in the previous subsection, the y-position of the particle trajectory at FP and BT strongly depended on the particle momentum. For the further trigger rate reduction, we limited the region that Ξ^-'s likely stop in the target, $p_{K^+} > 1.1$ GeV/c, which was predicted by the Monte Carlo simulation. Figure 2.21 shows the correlation between the FP element number and the BT log number for K^+'s of $p_{K^+} > 1.1$ GeV/c. The region surrounded by a solid line corresponds to the selected area by the matrix coincidence logic, which was determined by the offline analysis during the beam time. The trigger rate decreased by a factor of five with the efficiency of 92% using this logic. The trigger decision time was 420 ns. Considering the time necessary for the signal to travel back to the experimental area, the IIT gate on the second stage opened 670 ns after the reaction, which was acceptable for the decay time of the phosphor on the first stage IIT (2.4 μs). Since it turned out that the IIT image was not intensified at the trigger rate higher than 60 Hz for the Hamamatsu one and 100 Hz for the Delft one as mentioned in Section 2.9.2, trigger requests coming within 15 ms after the accepted trigger were inhibited by self-veto (trigger hold-off). The live time of IITs dropped to about 50% due to this trigger hold-off. As a result of the above operations, the typical trigger rate was 50 per spill at the first level.

The second-level trigger for IITs was a logical AND of the IIT first-level trigger described above and the normal second-level trigger described in the previous subsection. The trigger decision was made 19 μs after the first-level trigger decision. Also while the data acquisition of CCD images was busy, this trigger was vetoed. The IIT second-level trigger rate was around 12; the reduction factor was about four compared to the IIT first-level trigger rate.

2.11 Data acquisition system

The data taking was performed by the VME-based data acquisition (DAQ) system. Figure 2.22 shows a schematic diagram of the DAQ system. Two Fast Intelligent Controllers (FIC, CES 8232 and CES 8231), called FIC1 and FIC2 respectively, functioned as a core of this system. A microprocessor Motorola 68000 was built in on FIC, and both of FIC1 and FIC2 were operated by OS9/68000.

Analog signals from PMTs of scintillator hodoscopes, aerogel Čerenkov counters, and neutron counter arrays were divided into two streams. The signals in one of the streams were brought to Fastbus ADCs (LeCroy 1885) after proper attenuation, while those in the other stream were brought to Fastbus TDCs (LeCroy 1879, Kinetic F432) through discriminators. Concerning signals from the drift chambers, the discriminated pulses were sent to Fastbus TDCs (LeCroy 1885) for timing measurement of each sense wire, which was converted to the position information. The Fastbus ADCs and TDCs were controlled by the Fastbus Segment Manager/Interfaces (SM/I), located in each of four Fastbus crates, according to system calls from FIC1 through the CAMAC interface (LeCroy 2891A). The

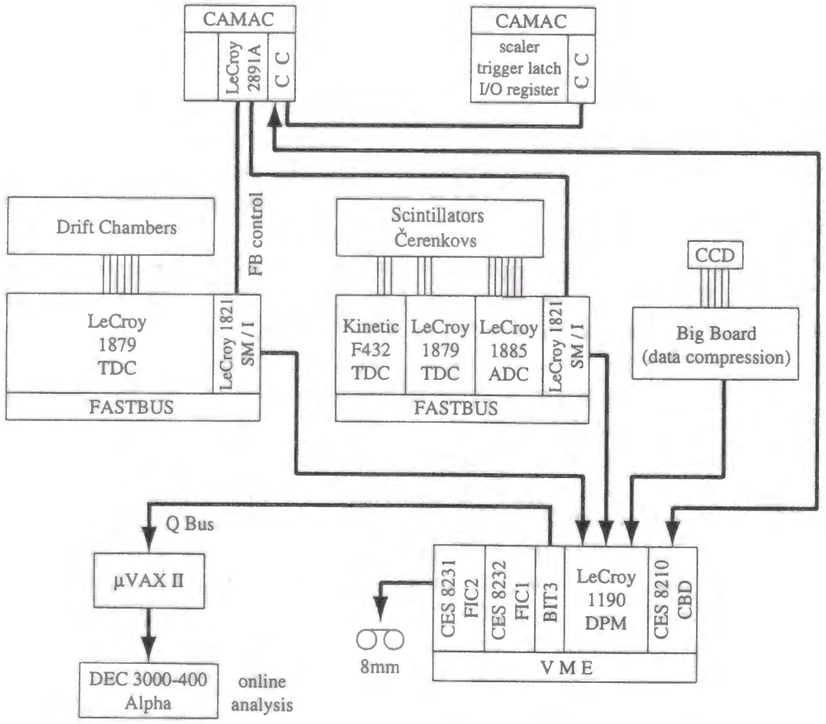

Figure 2.22: Schematic chart of the data acquisition (DAQ) system.

data collected in the Fastbus modules were transferred to VME Dual Port Memory (DPM) modules (LeCroy 1190) through the SM/I's. The SCIFI image data obtained and digitized by CCD cameras were sent to the DPMs after being compressed by trimming off the pixel data of which brightness was below the threshold. This compression process was performed by the specially designed two "Big Boards", one board for each IIT system, where the thresholds were adjusted by dip-switches on the board. Other important data such as scaler counts and trigger patterns were taken by the CAMAC modules. The CAMAC data were temporarily stored in the FIC1 memory through the CAMAC Branch Driver (CES 8210).

After the completion of the data collection, FIC2 read the data on the DPMs and FIC1 memory with Direct Memory Access (DMA), and then wrote them onto 8mm tapes using an Exabyte 8mm tape drive. Although the data size depended on the beam rate, the typical value was 13.8 kbytes in total, which contained 2.6 kbytes of the counter data and 11.2 kbytes of the image data from the four IITs.

2.12 Online monitoring

While the data collected in FIC2 were written down on the 8mm tape, a sample of them were transferred to a μVAX II via a BIT3 VME-Qbus interface for online monitoring. For efficient monitoring, the data brought to the μVAX II were also passed to a DEC 3000-400 Alpha running OpenVMS by way of Ethernet. The online analysis was performed by a software package called IDA. It allowed us to monitor not only the detector performance but also the kinematic values such as the momentum, mass, and reaction vertex. It was quite useful to check the trigger performance. The IIT images were monitored with respect to the image quality by another software based on the HIGZ package. Not only experimental data but also high voltages applied to the detectors were objects for online monitoring. The difference between the actual and demand values was monitored by a software called HVOLT. This software was also utilized for high voltage operations such as turning-on, turning-off, and gain-adjustment by remote control.

Chapter 3

Data Analysis

3.1 Outline

The data acquisition was performed from March to June in 1996. The diamond target was exposed to 8×10^{11} K^-'s in total during the whole period of the experiment. The obtained data were then subjected to detailed offline analysis. The data was first analyzed in terms of the track-reconstruction and particle-identification of incident and outgoing particles. Then the basic (K^-, K^+) data sample was extracted using the combined information of the incident and outgoing particles. The further analyses were divided into two streams. One was the severe background suppression by application of a series of tight cuts in order to search for the direct production of the H-dibaryon by investigating the missing mass spectrum below the end point of quasi-free Ξ^- production. If H-dibaryons are produced with cross section within our sensitivity, a peak structure would be seen at the position corresponding to the H mass. The other was the analysis of image data obtained by the SCIFI detectors. Here, H-dibaryons assumed to be produced via the atomic capture of stopped Ξ^-'s were searched for with respect to the $H \to \Lambda n$ decay mode. The (K^-, K^+) events which passed through the relatively loose cuts were used in this analysis in order not to reduce the statistics. Each image was scanned by human eyes for selection of the events of interest. Then the selected events were sent to the reconstruction of the kinematics of $H \to \Lambda n$ by combining with data from the neutron counter arrays so as to search for the mass peak of the H.

For the analysis software, we utilized the Interactive Data Analyzer (IDA) package for the primary analysis on the counter data. This package was originally designed for the NA36 experiment at CERN, and then further developed for the Brookhaven H search experiments on the VMS platform. Since each analysis process is built in as a "module", one can easily make analyses of both specific detectors and overall kinematics. Moreover, inclusion of the HBOOK package into IDA allowed us to extract the analyzed data in the form of a column-wise ntuple and to make a further analysis such as cut studies with PAW. The image data of the SCIFI detectors were scanned by another software using the HIGZ package for image browsing.

3.2 Beam analysis

The momenta of beam particles were calculated by fitting hit positions at the beam-line hodoscopes (MT and MP) and drift chambers (ID1-3) with use of the second-order TRANSPORT [127] matrix. Figure 3.1 shows the momentum spectrum of the beam particles. Also Figure 3.2 represents the beam profile at the target position, which was obtained from projection of the straight-line fit of hit points in ID1-3.

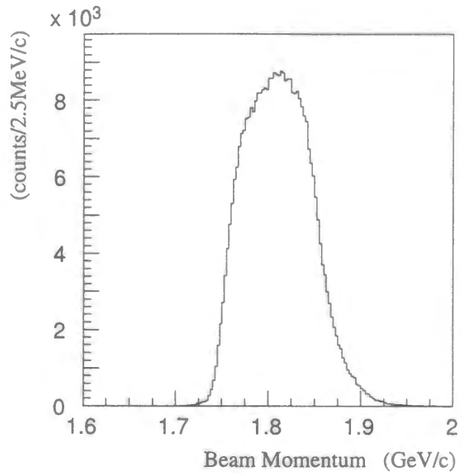

Figure 3.1: Momentum distribution of the beam particles.

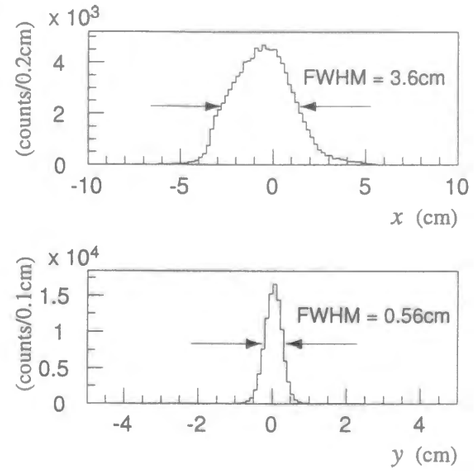

Figure 3.2: Beam profile at the target position along x (top) and y (bottom).

The particle identification was basically performed by a pulse height cut on IC aerogel Čerenkov counter. At the online trigger level, the π^- rejection efficiency was 99.4% as mentioned in Section 2.7. A tighter cut in the offline analysis after the calibration of the pedestal fluctuation caused by the 60Hz cycle AC noise (see Appendix C) permitted us to obtain higher efficiency. The TOF between MT and IT, shown in Figure 3.3, was also utilized to minimize the π^- contamination. These are described later in the specific cut studies.

3.3 Track reconstruction of outgoing particles

Trajectories of outgoing particles were reconstructed by using the information of hit position at the drift chambers (FD0-3 and BD1-2) and of the field map in the 48D48 dipole magnet. The whole reconstruction process can be divided into three stages:

1. Straight-line fit upstream of the 48D48 magnet.
2. Straight-line fit downstream of the 48D48 magnet.

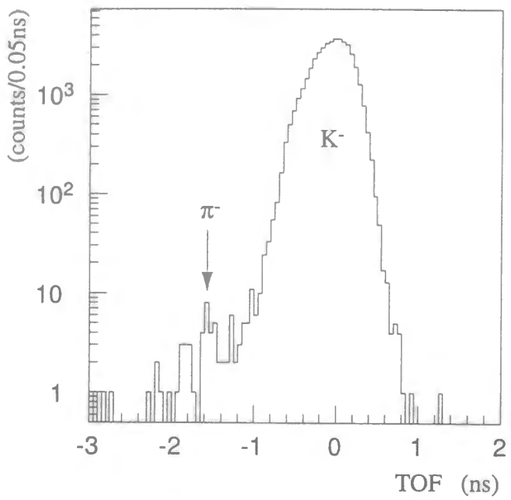

Figure 3.3: Spectrum of the TOF between MT and IT for particles passed through the online K^- selection by the aerogel Čerenkov counter IC.

3. Connection of the two trajectories in the 48D48 magnet considering the consistency of the equation of motion in the magnetic field.

For the stage 1, hit positions on the total fourteen planes of FD0-2 were fitted with straight lines. For the cases of multiple hits, all of reasonable combinations were considered. Also, since it is possible to have missing hits on a couple of planes, it was acceptable to drop less than two planes from the fit in the algorithm to find track candidates. For the stage 2, the method of track finding was the same as that in the stage 1. The hits on the total of nine planes of BD1 and BD2 were the subjects of fitting here.

For the analysis of the stage 3, the Runge-Kutta tracking is usually carried out. However, since it takes a lot of time to make the Runge-Kutta tracking for every event, we adopted a method of the local-fit parameterization similar to that used in TRANSPORT [127]. To parameterize the tracking, the phase space of the 48D48 spectrometer acceptance was broken into 1440 divisions in terms of trajectory position at z=0, scattering angle, and momentum. The central trajectory of each division of the phase space was calculated by the fourth-order Runge-Kutta tracking. This central trajectory and the first-order deviation in the division were parameterized as matrices. The actual trajectory and momentum were calculated from the first-order correction of the central trajectory of the corresponding division. The size of each phase space division was determined in order that the reconstructed momentum error lies below 0.3% for all of divisions. Using this method, track reconstruction was performed with simple matrix operations after reading the matrix elements when starting the analysis. This made the calculation time shorter and the repetition of analysis for various studies easy. This track fitting was performed for

all combinations of straight tracks before and after the 48D48 magnet.

In order to valuate each trajectory candidate, the goodness-of-fit, which was defined in Eq. (3.1), was calculated.

$$\chi^2 = \left\{ \sum_{i=1}^{5} \frac{(x_i - x_i')^2}{\sigma_{xi}^2} + \sum_{i=1}^{5} \frac{(y_i - y_i')^2}{\sigma_{yi}^2} \right\} / 5 \tag{3.1}$$

Here x_i and y_i refer to the measured position at each drift chambers, while x_i' and y_i' refer to the fitted-track projection on each chamber z position. Also the position resolution of each chamber is represented as σ_{xi} and σ_{yi}. The summation was performed over the five drift chambers FD1-3 and BD1-2. The best fit which provides the minimum χ^2 was sent to the next step of the analysis. Figure 3.4 shows the goodness-of-fit distribution.

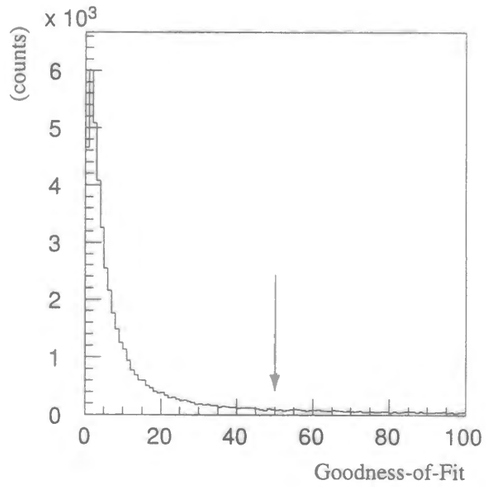

Figure 3.4: Goodness-of-fit distribution of the outgoing particles. The arrow shows the cut position in the data reduction.

3.4 Reaction vertex

In order to obtain the position of the reaction vertex, the distance of closest approach (DCA) between the beam track and the reconstructed trajectory of the outgoing particle was calculated first. Given z_p and z_s as z positions on each track which provided the DCA, the z coordinate of the vertex position, z_{vtx}, was calculated to be the middle point: $(z_p + z_s)/2$. The x and y coordinates of the vertex position, x_{vtx} and y_{vtx}, were defined as a projection of the straight-line fit of the beam track to $z = z_{vtx}$ considering smaller fitting errors of the beam track compared to that of the outgoing-particle trajectory. When we had multiple candidates of the beam tracks, the track which provided the smallest DCA was selected to produce one complete event. Figures 3.5 and 3.6 represent the distribution of DCA and the reaction vertex. The target was positioned at $(x, y, z) = (0, 0, -19.5\,\mathrm{cm})$.

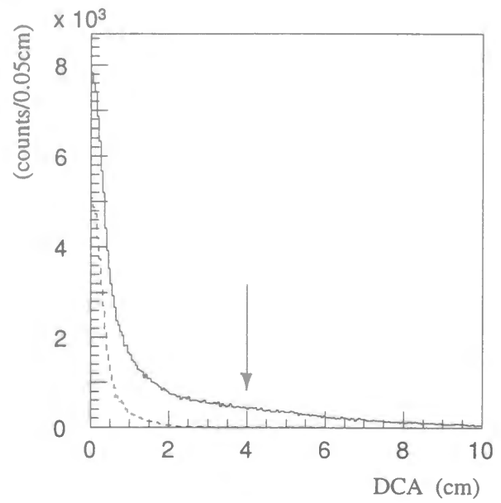

Figure 3.5: Distribution of the distance of closest approach (DCA). The dashed line shows the distribution with the cut of goodness-of-fit < 50. The arrow indicates the cut position in the data reduction.

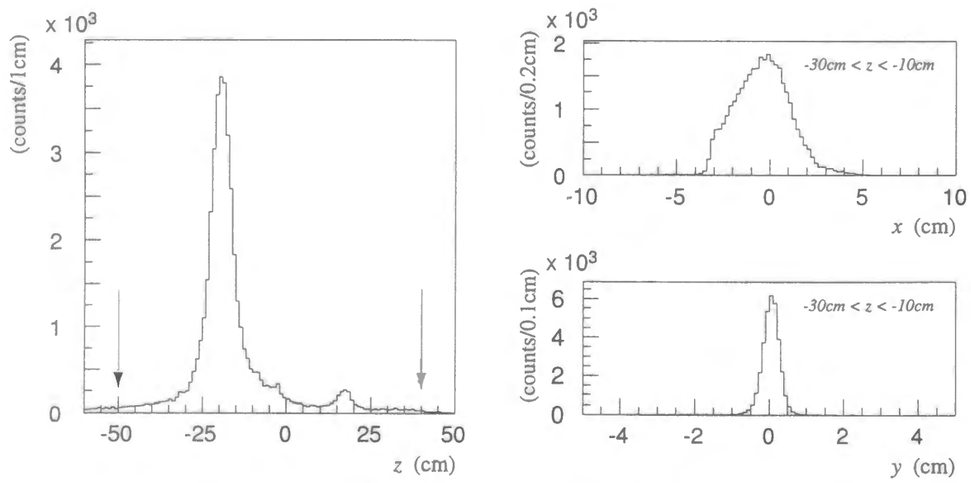

Figure 3.6: Distribution of the reconstructed reaction vertex with the cut of goodness-of-fit < 50. (Left) : z vertex; (Top right) : x vertex; (Bottom right) : y vertex. An additional cut $-30\text{cm} < z < -10\text{cm}$ was applied for the x and y vertices. The target was positioned at $(x, y, z) = (0, 0, -19.5\,\text{cm})$. The arrows in the z vertex distribution show the cut positions in the data reduction.

3.5 Momentum of outgoing particles

As a consequence of tracking, momenta of outgoing particles were calculated as mentioned in Section 3.3. Figure 3.7 shows a plot of momentum versus TOF for the outgoing particles. Three loci correspond to π^+, K^+, and protons, respectively, as indicated in the figure. Figure 3.8 represents the momentum spectrum of outgoing K^+'s. The K^+ sample was obtained from a cut on the outgoing-particle mass described in the next section. The cut region is shown in Figure 3.9. The peak at 1.2 GeV/c corresponds to the quasi-free Ξ^- production as will be discussed in Section 3.7. In the the low momentum region ($\lesssim 1.0$ GeV/c), the (K^-, K^+) events should be dominated by the $\Xi^*(1530)^-$ production and the two-step process: $K^- + N_1 \to \pi + Y_1$, $\pi + N_2 \to K^+ + Y_2$, where N_1, $N_2 = p$ or n, $\pi = \pi^0$ or $\pi^\pm$, and Y_1, $Y_2 = \Lambda$, Σ^0, or $\Sigma^\pm$. The strength for the sum of these processes is similar to or larger than that of the Ξ^- production which dominates in the high momentum region [121]. However, the above processes in the low momentum region were out of the acceptance of the spectrometer. The momentum resolution ($\Delta p/p$) was derived from the missing-mass width of the Ξ^- production on hydrogen. It was estimated to be better than 0.53% in r.m.s. at 1.2 GeV/c. The details are described in Section 3.12.3.

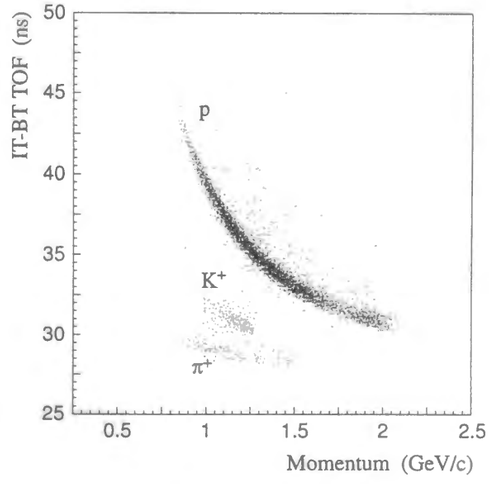

Figure 3.7: Plot of momentum versus TOF for the outgoing particles. Three loci correspond to π^+, K^+, and protons, respectively, as indicated.

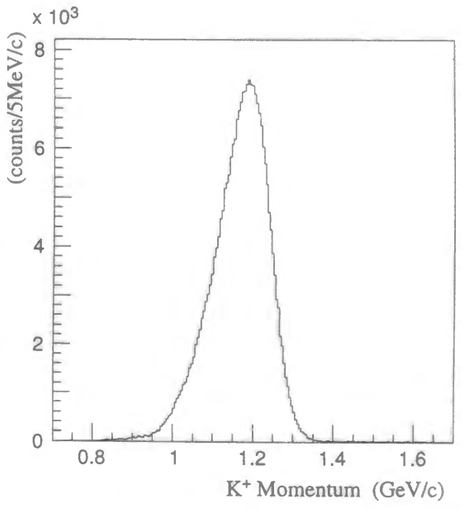

Figure 3.8: Momentum spectrum of the outgoing K^+. The low momentum region is out of the acceptance of the spectrometer (see the text).

3.6 Mass of outgoing particles

Mass of the outgoing particle was reconstructed by the measured momentum, path length, and TOF. The momentum and path length were calculated in the trajectory reconstruction as described in Section 3.3. For estimating TOF of the outgoing particle, we used TOF from IT to BT, which is a sum of TOF of the beam particle from IT to the vertex and TOF of the outgoing particle from the vertex to BT. By subtracting the former contribution using the measured beam momentum and assuming the beam particle to be K^-, TOF of the outgoing particle from the vertex to BT was calculated. Then the mass of the outgoing particle M was calculated by the following equation:

$$M = \frac{P\sqrt{(cT)^2 - L^2}}{L}, \tag{3.2}$$

where P, T, L, and c stand for the outgoing-particle momentum, TOF from the vertex to BT, path length from the vertex to BT, and light velocity, respectively. Figure 3.9 shows the mass spectrum of outgoing particles.

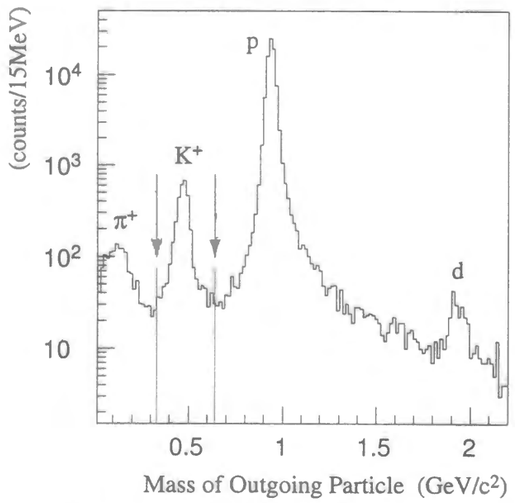

Figure 3.9: Mass spectrum of the outgoing particles. The events between the arrows were extracted as the K^+ sample in the data reduction.

In order to adjust the absolute value of the mass spectrum, the timing calibration of TOF from IT to BT was very important. This was done by investigating the TOF difference (ΔTOF) between the measured one (TOF_{meas}) and the predicted one (TOF_{pred}) calculated from the measured path length and momentum,

$$\Delta TOF = TOF_{meas} - TOF_{pred}\,. \tag{3.3}$$

The proper offset was calculated in order that ΔTOF became zero. As the timing offsets sometimes shifted (roughly one per week) due to bad cable connections and grounding or some other unresolved reasons during the data collection, the timing calibration was basically performed run by run in the offline analysis. Therefore, the calibration was carried out using protons resulting from K^-p scattering of which statistics easily accumulated. Namely, TOF_{pred} in Eq. (3.3) was calculated for protons. Based on the above method, the relative timing among four elements of IT was adjusted by calculating ΔTOF between a specified BT element (#18) and each IT element for the first step. Then, each timing offset of BT elements (#1 $\sim$ #39)[1] was calibrated. As a result, the center of the K^+ peak was positioned at 489.9 MeV/c^2, while the world average of the K^+ mass is 494.677 $\pm$ 0.016 MeV/c^2. The mass resolution of K^+ was obtained to be 19.1 MeV/c^2 r.m.s., which corresponds to the TOF resolution of 164 ps.

3.7 Missing mass

Missing mass is defined as the invariant mass of an undetected residual system assuming the target particle to be at rest. This variable is determined by measurement of momenta of both incident and outgoing particles. In the reaction $1 + 2 \to 3 + X$, where 1 is the incident particle, 2 is the target, and the momenta of 1 and 3 are measured to be $\vec{P}_1$ and $\vec{P}_3$, missing mass M_X is calculated as

$$M_X = \sqrt{\left(\sqrt{P_1^2 + M_1^2} - \sqrt{P_3^2 + M_3^2} + M_2\right)^2 - \left(\vec{P}_1 - \vec{P}_3\right)^2}, \tag{3.4}$$

where M_1 and M_2 are rest masses of the incident and target particles. Energy loss of the particle 1 and 3 when traveling inside the target and detectors was taken into account in order to obtain $\vec{P}_1$ and $\vec{P}_3$ which are the momenta at the reaction vertex. As the z vertex resolution was not so good, the reaction vertex was assumed to be at the center of the target in the calculation. Figure 3.10 shows the missing mass spectra of the (K^-, K^+) reaction against carbon targets calculated with carbon kinematics, $^{12}\mathrm{C}(K^-, K^+)X$, and proton kinematics, $p(K^-, K^+)X$, respectively. The quasi-free production of Ξ^- was clearly observed.

The missing mass resolution was studied with use of a CH_2 target because the Ξ^- production on hydrogen in CH_2 can be regarded as a two-body reaction. The missing-mass width of 3.8 MeV/c^2 r.m.s. was obtained for the $p(K^-, K^+)X$ kinematics as the experimental resolution. The absolute value of the missing mass was also adjusted using the peak of Ξ^- produced with the (K^-, K^+) reaction on hydrogen. An additional energy correction by -30 MeV was applied to the outgoing K^+ so that the peak center of the missing mass for Ξ^- production on hydrogen was positioned at 1321 MeV. The details are described in Section 3.12.3.

[1] Although the total number of BT elements was forty, the data from #40 was not used, because it had few hits and thus the timing alignment was not possible.

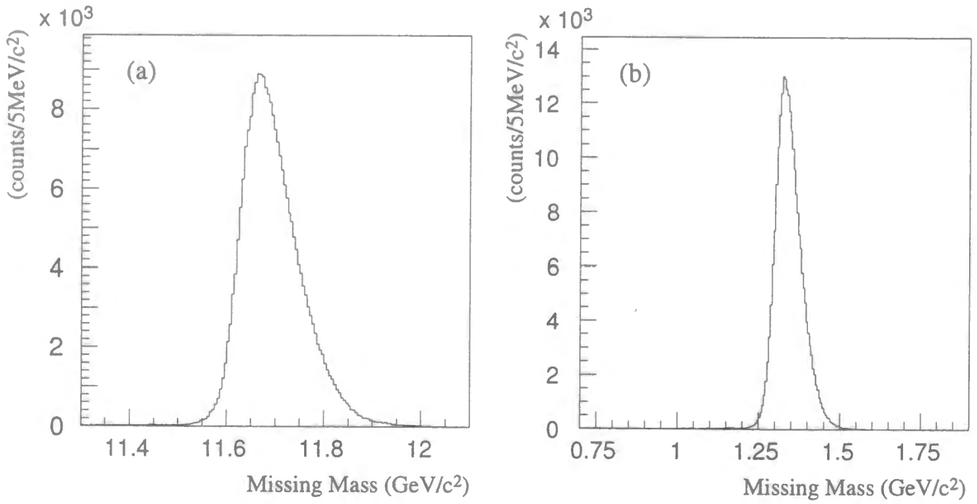

Figure 3.10: Missing mass spectra for the kinematics of $^{12}\mathrm{C}(K^-, K^+)X$ (a) and $p(K^-, K^+)X$ (b). The quasi-free Ξ^- production was clearly observed.

3.8 Data reduction

The experimental data obtained through the first- and second-level triggers for (K^-, K^+) selection were recorded over more than two-hundred 8mm-tape cartridges. However, they still contained a large amount of background such as (K^-, p) events as shown in Figure 3.9. In order to treat the data more easily, an enriched sample of the (K^-, K^+) reaction was extracted from the data on 8mm tapes with several kinematic criteria and was stored on a hard disk of a workstation. The criteria included cuts on the goodness-of-fit, DCA, z vertex, and reconstructed mass of outgoing particles, which are shown as arrows in Figures 3.4, 3.5, 3.6, and 3.9, respectively. The cuts were very loose at this stage for the safety: goodness-of-fit < 50, DCA < 4 cm, -50 cm $< z < 40$ cm, and 0.33 GeV/c^2 $<$ outgoing-particle mass < 0.64 GeV/c^2. The further analysis on the (K^-, K^+) reaction was performed using this data sample. The number of events which passed the above criteria was found to be 357,580. With the more reasonable z vertex cut around the target, -40 cm $< z <$ 0, the number of (K^-, K^+) candidates amounted to 316,967, which is the largest-to-date event number obtained in experiments.

3.9 Neutron measurement

With the neutron counter arrays described in Section 2.8, the time-of-flight, hit position, and energy deposit of neutrons (pulse height) were measured. The neutrons of our interest were expected to be produced via the following reactions:

$$(\Xi^-, {}^{12}\mathrm{C})_{atom} \to H + X \tag{3.5}$$

$$H \to \Lambda + n\,, \tag{3.6}$$

and

$$(\Xi^-, {}^{12}\mathrm{C})_{atom} \to {}^{12}_{\Lambda\Lambda}\mathrm{B} + n\,. \tag{3.7}$$

The analysis processes of neutron measurement are described below.

3.9.1 Measurement of time-of-flight and hit position

The time-of-flight (TOF) of the neutron was obtained from the meantime of two PMTs coupled to both ends of each scintillator log. The explicit representation of TOF of the i-th log is:

$$TOF^i = \alpha \cdot \frac{TDC_1^i + TDC_2^i}{2} - T_{IT} - \bar{T}_0^i - T_{off} - \frac{\Delta z}{c\beta_K}\,. \tag{3.8}$$

The coefficient α is a constant to convert a TDC channel to time. TDC_1^i and TDC_2^i are TDC values for the top (the subscript "1") and bottom (the subscript "2") PMTs of the i-th scintillator log. T_{IT} is the time when the beam particle passed through IT counter, which was defined as the start time of every event. The log-dependent offset is calibrated by $\bar{T}_0^i$, while T_{off} is used for the overall offset calibration. Δz is the distance traveled by the K^- from IT to the target center and $c\beta_K$ is the velocity of the K^-, thus $\Delta z/c\beta_K$ stands for the traveling time of the K^- between IT and the target center. Also, the hit position along the log, namely y, is measured by

$$Y_{ND} = c' \cdot \alpha \cdot \frac{TDC_1^i - TDC_2^i - T_{diff}^i}{2} + Y_0\,, \tag{3.9}$$

where c' stands for the speed of light in the scintillator, T_{diff}^i refers to an offset to calibrate the TDC difference of the i-th log, and Y_0 is the y position of the log center. For x and z position of the hit, the log center along each direction was used. Then as a kinematic value which reflects energy, β^{-1} was defined as follows:

$$\beta^{-1} = c\frac{TOF}{\ell}\,, \tag{3.10}$$

where c is the speed of light and ℓ is the distance between the target center and the hit position. Figure 3.11 shows the β^{-1} spectrum of neutral hits. The prominent peak standing at $\beta^{-1} = 1$ comes from prompt γ's resulting from de-excitation of the target nuclei, while the smooth spectrum over the whole range shows neutrons. It should be reminded that slower neutrons correspond to higher values of β^{-1}.

Here are described the calibration constants in Eqs. (3.8)-(3.10). The TDC channel to timing conversion coefficient α, whose nominal value is 0.025 ns/ch, was calibrated using the delayed trigger for all TDC channels. $\bar{T}_0^i$ and T_{diff}^i were obtained from the cosmic ray calibration (see Section 3.9.4). Concerning T_{off}, it was obtained by measuring TOF of prompt γ's at $\beta^{-1} = 1$. Since the time between the moment of impact of the beam particle against the target nucleus and emission of a prompt γ is negligible, the time interval between the (K^-, K^+) reaction and the neutron detection can be calculated using this calibration constant. At this step, the remaining components which should be considered were the stopping time of Ξ^-, and for the measurement of neutrons from the H-dibaryon, the decay time of H. Since it was impossible to measure them event by event, the average stopping time of Ξ^-, which was estimated to be 0.14 ns with the distribution width of 75 ps (r.m.s.) using the Monte Carlo simulation, was added to the T_{off} and the remaining uncertainties, the H decay time and deviation of the Ξ^- stopping time from its average for each event, were taken into account to the width and position shift of the expected peak when searching for the signal. The timing of each log was checked through all the runs by monitoring the γ peak, and any timing shifts were calibrated by adjusting $\bar{T}_0^i$ so as to obtain a correct timing of γ's. This suppressed the long-term timing drift within 100 ps.

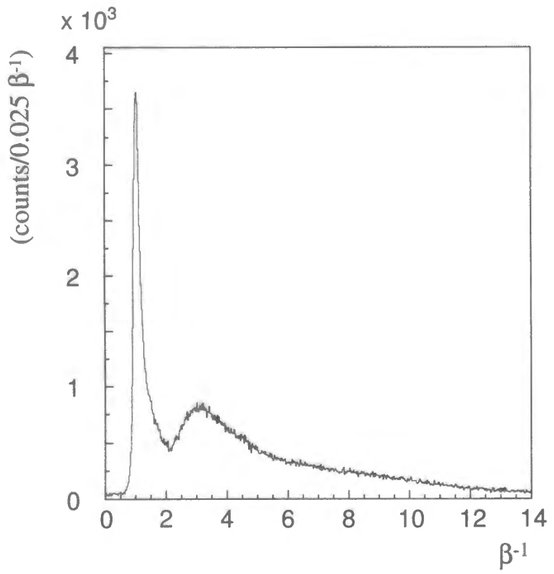

Figure 3.11: β^{-1} spectrum of neutral hits. The prominent peak at $\beta^{-1} = 1$ comes from prompt γ's, while the smooth spectrum over the whole range shows neutrons. Slower neutrons corresponds to higher values of β^{-1}.

3.9.2 Measurement of energy deposit

Energy deposit in the neutron counter log was calculated by the geometric mean of ADC values of two PMTs at each ends of the log in order to compensate the light attenuation in the scintillator. Therefore the energy deposit of the i-th log is

$$E_{ND}^i = \sqrt{C_1^i \cdot ADC_1^i \cdot C_2^i \cdot ADC_2^i}\,, \tag{3.11}$$

where ADC_1^i and ADC_2^i are ADC channels measured from the pedestal. C_1^i and C_2^i were calibration constants to convert ADC values to energy deposit, which were determined by a cosmic ray entering the center of each log (Section 3.9.4). They are defined as

$$C_1^i = \frac{E_0}{ADC_{01}^i}\,, \qquad C_2^i 2 = \frac{E_0}{ADC_{02}^i}\,, \tag{3.12}$$

where E_0 is the energy deposit of a cosmic ray passing through the center of the log, 10.46 MeV. ADC_{01}^i and ADC_{02}^i are the corresponding ADC values obtained from the top and bottom PMTs of the i-th log.

Actually, by using an exponential nature of the light attenuation with the attenuation constant λ, the observed energy at both ends of the log due to the energy deposit at any place will be expressed to be

$$E_1^i = \epsilon_1^i E \exp\left(-\frac{\ell_1}{\lambda}\right)\,, \qquad E_2^i = \epsilon_2^i E \exp\left(-\frac{\ell_2}{\lambda}\right)\,, \tag{3.13}$$

where E is the "true" energy deposit, while ϵ_1^i and ϵ_2^i are coefficients proportional to the light production and collection efficiencies. The distance between the position of the energy deposit and each end of the log is denoted as ℓ_1 and ℓ_2. From the ratio of ADC with a hit at any place of the log to that at the log center,

$$\begin{aligned} E_1^i &= \epsilon_1^i E_0 \exp\left(-\frac{L}{2\lambda}\right) \cdot \frac{ADC_1^i}{ADC_{01}^i} \\ &= \epsilon_1^i \exp\left(-\frac{L}{2\lambda}\right) \cdot C_1^i \cdot ADC_1^i\,, \end{aligned} \tag{3.14}$$

where L is the whole length of the log. Similarly,

$$E_2^i = \epsilon_2^i \exp\left(-\frac{L}{2\lambda}\right) \cdot C_2^i \cdot ADC_2^i\,. \tag{3.15}$$

Then,

$$\begin{aligned} \sqrt{C_1^i \cdot ADC_1^i \cdot C_2^i \cdot ADC_2^i} &= \sqrt{\frac{E_1^i}{\epsilon_1^i \exp(-L/2\lambda)} \cdot \frac{E_2^i}{\epsilon_2^i \exp(-L/2\lambda)}} \\ &= \sqrt{\frac{\epsilon_1^i E \exp(-\ell_1/\lambda)}{\epsilon_1^i \exp(-L/2\lambda)} \cdot \frac{\epsilon_2^i E \exp(-\ell_2/\lambda)}{\epsilon_2^i \exp(-L/2\lambda)}} \\ &= E\sqrt{\exp\left\{\frac{-(\ell_1+\ell_2)+L}{\lambda}\right\}} \\ &= E\,. \end{aligned} \tag{3.16}$$

3.9.3 Identification of neutral hits

Since neutrons were observed from the recoil of charged particles caused by the n-p and/or n-^{12}C scattering in the scintillator, it is possible that the resulting charged particles enter the neighboring scintillator logs and provide signals. To avoid preventing such multiple hits from being regarded as independent events, a group of hits in the neighboring scintillator logs was considered as a "cluster" which was induced by single neutron. The y position difference of the neighboring hits in the cluster was required to be within 30 cm. The y position resolution is described in Section 3.9.5. With the above definition, 20% of total neutral events were recognized as the multi-hit clusters. The time of detection was assumed as that of the earliest log in the cluster.

Identification of the neutral hit was performed by first examining whether the charge-veto counter along the possible path from the target and the cluster defined above had a hit or not. If there was no corresponding hit, the event was identified as neutral. But if there was, the additional requirement was tested. For the charged particles, the y-projection on the veto counter for the path connecting the target and the cluster was required to be positioned within ± 25 cm from the y-position calculated from the time difference of the two PMTs at both ends of the veto element. If the hit did not satisfy this requirement, the event was recognized as neutral. The detailed description can be also found in Refs. [76, 77].

3.9.4 Cosmic ray calibration

As mentioned in the previous subsections, most of the calibration constants in calculating the kinematic variables were obtained from the cosmic ray calibration which was carried out before and after the run. A schematic view of this calibration setup is shown in Figure 3.12. The neutron counter arrays were settled down on the floor, and two scintillator bars put at the center of the logs over and below the array were used as trigger counters. The cosmic ray data were taken in coincidence with the hit in both trigger counters. The perpendicular tracks were selected out in the offline analysis by looking at hit patterns in the arrays.

Since the neutron counter layers were aligned with a shift by a half of the log width alternately, timing adjustment between the logs in the same layer was achieved by using the timing information of the neighboring layer. For example, in Figure 3.12, the use of an event sample passing through the path labeled as "Cosmic 1" and another sample passing through the path labeled as "Cosmic 2" allowed us to adjust the relative time offset between Log A and Log B in the first layer by aligning the relative timing between Log A and Log C and that between Log B and Log C. Time offsets of the remaining logs in the first layer were adjusted in the same way. After making this process for other layers, timing adjustments between the layers were performed considering the layer distance. In this way, the time offset of the i-th log , $\bar{T}_0^i$, was calculated for all the logs in the neutron counter array. As for T_{diff}^i, it was obtained so that the difference of TDC values between the two PMTs viewing the log became zero.

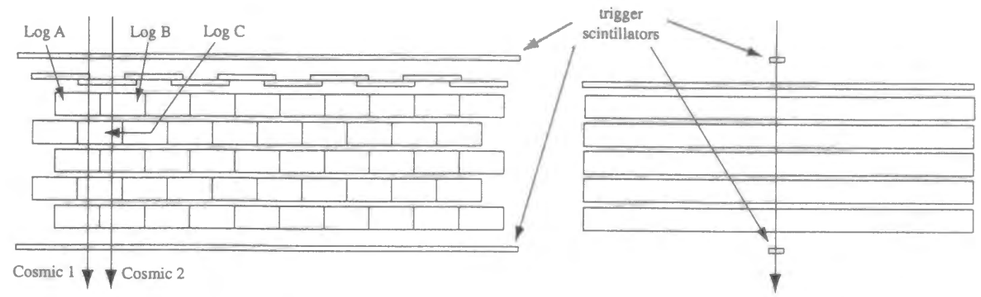

Figure 3.12: Schematic view of the setup for the cosmic ray calibration. The left figure shows the 90°-rotated view of the right figure.

Also, the average energy loss of a minimum ionizing particle when passing vertically through the log was calculated to be 10.46 MeV. From this fact, the energy deposit calibration was done using the relation in Eq. (3.12). The gain change was found to be within ~10% comparing the data taken before and after the run.

3.9.5 Timing and position resolution

The resolution of the TOF measurement (σ_t) was studied using cosmic rays and a laser flasher, and it was parameterized on the average of two-hundred scintillator logs as

$$\sigma_t(\mathrm{ns}) = \frac{0.41}{\sqrt{E(\mathrm{MeV})}}, \tag{3.17}$$

where E is the energy deposit in the scintillator log. The details are written in Refs. [77, 108]. For the cosmic ray, the mean energy deposit was calculated to be 10.46 MeV, and the corresponding timing resolution was 127 ps. However, when neutrons hit the log, the energy deposit spreads with a certain distribution due to the detection mechanism. Thus the timing resolution of neutrons with kinetic energy of T_n was estimated by folding the distribution as follows:

$$\sigma_t^2(T_n) = \sigma_0^2 \int \frac{E_0}{E} \cdot P(E, T_n) dE \tag{3.18}$$

with

$$\int P(E, T_n) dE = 1\,, \tag{3.19}$$

where σ_0 and E_0 is the timing resolution and the energy deposit for cosmic rays respectively, and $P(E, T_n)$ refers to the energy-deposit distribution for neutrons having the kinetic energy of T_n. $P(E, T_n)$ was calculated from the DEMONS code as mentioned in Section 2.8. In Ref. [76], $\sigma_t(T_n)$ was parameterized as

$$\sigma_t(T_n) = C \cdot [T_n(\mathrm{MeV})]^{-0.281}\ (\mathrm{ns}). \tag{3.20}$$

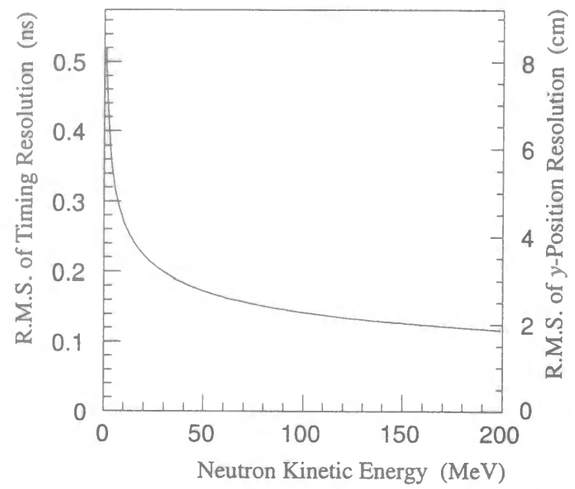

Figure 3.13: Timing and y-position resolution (r.m.s.) of the neutron counter arrays as a function of the neutron kinetic energy.

Considering the difference between timing resolution of Ref. [76] and ours[1], C was estimated to be 0.52.

As for the y-position resolution, from Eq. (3.9), it is written as

$$\sigma_{Y_{ND}} = \frac{c'}{2}\sigma_{diff} \,. \tag{3.21}$$

Here c' is the effective speed of light in the scintillator log, which was evaluated to be 16 cm/ns. σ_{diff} is the resolution of time difference between the two PMTs at both ends of the log. The TOF was calculated from a mean time of the two PMTs, and thus using the relation $\sigma_{diff} = 2\sigma_t$,

$$\sigma_{Y_{ND}} = 8.3 \cdot [T_n(\mathrm{MeV})]^{-0.281} \ (\mathrm{cm}) \tag{3.22}$$

was obtained. Figure 3.13 shows the timing and y-position resolution in r.m.s. as a function of the neutron kinetic energy.

[1] In the 1992 data taking, the intrinsic resolution of the TOF measurement was reported to be 137 ps, and C was estimated at 0.56 [76]. The TOF resolution was improved to be 127 ps by calibrating the common-mode rate-dependent shifts of start timing of the Kinetic F432 Fastbus TDCs. See Ref. [77] for the detail.

3.10 Image data analysis of the SCIFI detector

The image data obtained by the SCIFI detector was digitized in terms of the coordinates and brightness of each pixel on the CCD camera, then recorded on 8mm tapes in the same stream as the other counter data. This allowed the data to be easily handled by computers in the offline analysis. The raw image data was position calibrated at first, and then passed to the basic performance check and scanned by human eyes. The further analysis was focused on the search for $H \to \Lambda + n$ decays, which is described in Section 3.13.4.

3.10.1 Position calibration of image data

Since the electro-static focusing was performed in the first stage of the IIT, the image was influenced by pin-hole distortion. Also, a relatively large amount of leaking of the fringe field of the 48D48 spectrometer magnet into the IIT magnetic shields provided additional image distortion. This distortion effect was measured by recording the image of hole-pattern masks when the magnet was on. The calibration was performed by transforming the distorted image to the original configuration. Since the SCIFI block we used had a little complicated shape as shown in Figure 3.14, hole-pattern masks were put on the places labeled by 1, 2 and 3, which are the opposite sides of fibers coupled to the IITs, then the reference images were obtained by flashing LED light to the masks. According to the SCIFI block structure, the place 1 and 3 were covered by aluminum frames, thus 2mmϕ-holes were opened on the aluminum frame with 1 cm interval. For the place 2, since no frame was placed there, the masks presented in Figure 3.15 were put on when the calibration data were taken. Each hole had the diameter of a few hundred μm for the purpose of giving light to only one fiber, whose cross section was 1 mm $\times$ 1 mm as mentioned in Section 2.9.1. Using two types of the mask, all the fiber sheets were monitored. Figure 3.16 represents the distorted image of one SCIFI-detector channel which was influenced by magnetic fields and pin-hole distortion (a) and points of weighted-mean with brightness for each hole image (b). Suppose (X_i, Y_i) is defined as the coordinate of each point on the distorted image (Figure 3.16(b)), and (X_{0i}, Y_{0i}) as the coordinate of original configuration. The calibration was performed by finding the third-order polynomial function to transform the whole area globally for the first step. Coefficients of the function were found so as to make the following χ^2 least.

$$\begin{aligned}\chi^2 \;=\; \sum_i \Big[\Big\{ X_{0i} - (a_1 + b_1 X_i + c_1 Y_i + d_1 X_i^2 + e_1 X_i Y_i + f_1 Y_i^2 \\ + g_1 X_i^3 + h_1 X_i^2 Y_i + k_1 X_i Y_i^2 + \ell_1 Y_i^3) \Big\}^2 \\ + \Big\{ Y_{0i} - (a_2 + b_2 X_i + c_2 Y_i + d_2 X_i^2 + e_2 X_i Y_i + f_2 Y_i^2 \\ + g_2 X_i^3 + h_2 X_i^2 Y_i + k_2 X_i Y_i^2 + \ell_2 Y_i^3) \Big\}^2 \Big]\end{aligned} \tag{3.23}$$

This transformation, however, was not sufficient due to the higher order distortion, random sheet shifts by stacking errors, etc. Therefore, local corrections were performed in

order that every hole located at the right position, and every small triangle area formed by the nearest three holes one another was interpolated linearly. Moreover, the above calibration not only removed distortion effects but also included a transformation from the CCD pixel coordinate to the actual dimension. Figure 3.17 shows the calibrated mask image.

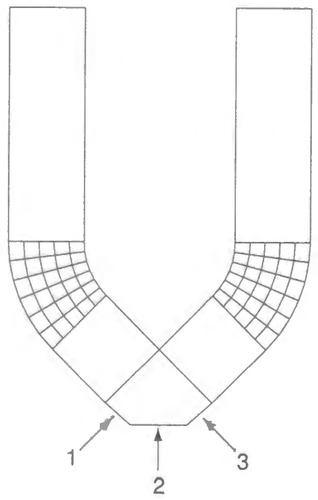

Figure 3.14: Schematic front view of the SCIFI block. The hole-pattern masks were put on the places labeled as 1, 2, and 3 when taking the position calibration data with LED flashers.

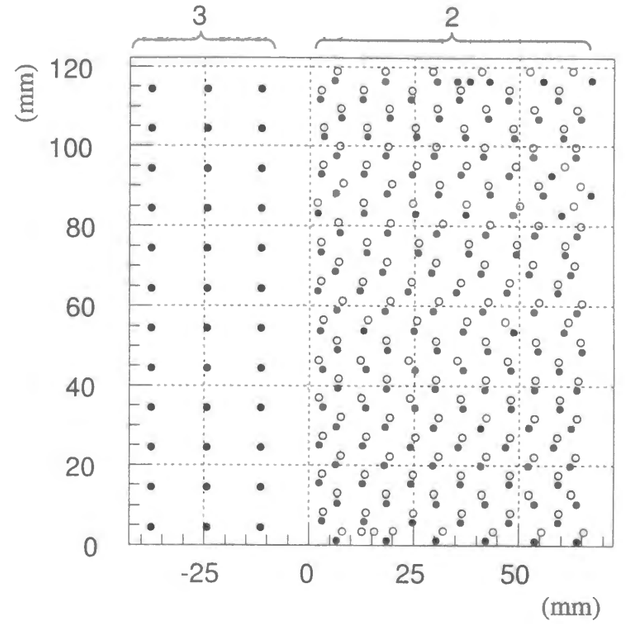

Figure 3.15: Hole patterns for the position calibration using a LED flasher. The region 2 and 3 correspond to those labeled 2 and 3 in Figure 3.14 respectively. Open and closed circles in the region 2 show the hole position in two different masks, while closed circles in the region 3 represent the projection of the holes on the aluminum frame onto the base plane of the SCIFI block.

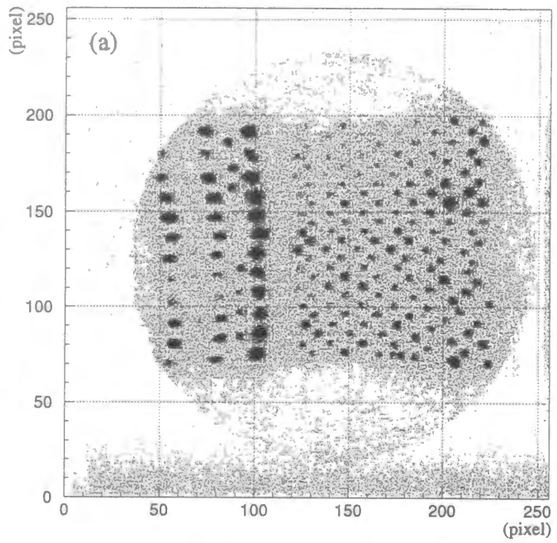

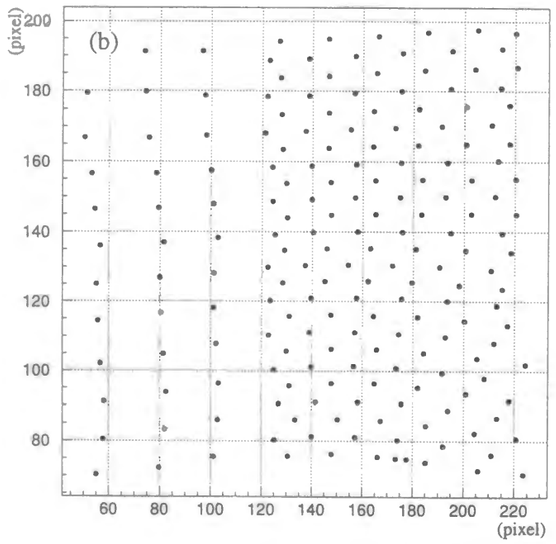

Figure 3.16: (a) : Distorted image of the mask-hole pattern under the magnetic field of the spectrometer. (b) : Points of weighted-mean with brightness for each hole image of (a).

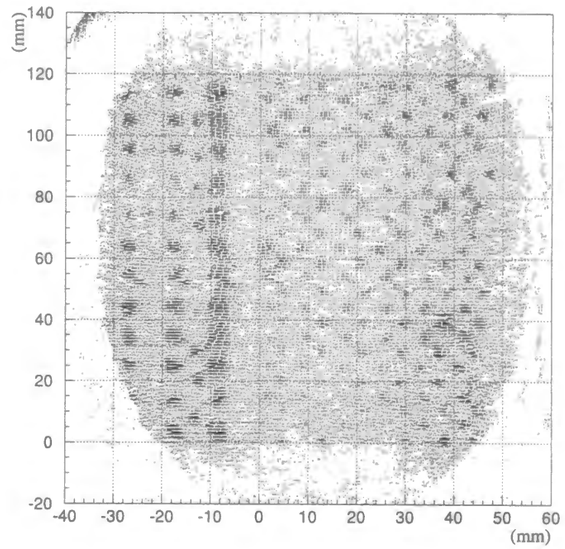

Figure 3.17: Calibrated image of Figure 3.16(a). The calibration also included transformation from the CCD pixel coordinate to the actual dimension.

3.10.2 Detector alignment

After the position calibration of the image data, spatial configuration between the internal coordinates of the SCIFI block and the global coordinates of the spectrometer system was calculated in terms of the rotation angles and the parallel shifts along x and y. This was done by using image data of straight beam tracks. As for the rotation angles, Euler angles between the above two coordinate systems were calculated. Defining $\vec{v}_{img}$ as a vector obtained by the straight-line fit of a beam track, $\vec{v}_{cham}$ as another vector which was reconstructed by the drift chambers for the same event, and $R(\theta, \phi, \psi)$ as a rotation matrix with Euler angles (θ, ϕ, ψ), the angular configuration of the two coordinate systems were deduced by searching for the optimized (θ, ϕ, ψ) which provided the least χ^2_θ defined as

$$\chi^2_\theta = \sum_i \left\{ \angle \left(R(\theta, \phi, \psi) \vec{v}^i_{img}, \vec{v}^i_{cham} \right) \right\}^2 \tag{3.24}$$

with use of the MINUIT package. Then, the parallel shift parameters along x and y were obtained from the x- and y-difference between the projection of the drift chamber tracks on the SCIFI block and the straight track images seen in the SCIFI block. In consequence, it was found that the bases of the SCIFI blocks were apart from 12.3 mm for the upper block and 15.7 mm for the lower block.

3.10.3 Performance of the SCIFI detector

The position resolution of the SCIFI detector was estimated from the deviation of the center of photon clusters around the straight-fitted line for beam particles, which can be treated as minimum ionizing particles (MIP). The obtained result is shown in Figure 3.18. The resolution of 490 μm was obtained for both Hamamatsu and Delft systems. Considering contributions from the fiber size ($\sigma_{fiber} = 1\text{mm}/\sqrt{12}$), CCD pixel magnification ($\sigma_{CCD} = 139\mu$m (Hamamatsu), 121 μm (Delft)), IIT resolution ($\sigma_{IIT} = 30\mu$m), and position calibration error ($\sigma_{cal} \sim \sigma_{fiber}$), the position resolution of the SCIFI detector is almost explained as follows:

$$\begin{aligned} \sigma_{pos} &= \sqrt{\sigma^2_{fiber} + \sigma^2_{CCD} + \sigma^2_{IIT} + \sigma^2_{cal}} \\ &= 432\mu\text{m(Hamamatsu)},\ 427\mu\text{m(Delft)}\,. \end{aligned} \tag{3.25}$$

Also, we note that the density of photon clusters along the track was found to be 3.6/cm.

The angular deviations of beam tracks in the image data from the predictions by the drift chambers were utilized to evaluate the angular resolution. Figure 3.19 represents the angular resolution as a function of the track length. It was parameterized to be

$$\sigma_\theta(\text{deg}) = 3.25/L(\text{cm})\,, \tag{3.26}$$

where L refers to the track length.

As another observable to show the SCIFI detector performance, the invariant mass of Λ hyperons was kinematically reconstructed. An event sample of the sequential Ξ^- decay presented in Figure 3.20 was selected for this analysis. The proton resulting from Λ decay was required to stop in the SCIFI block in order to determine its kinetic energy using the range-energy curve. The coefficients given in Ref. [73] were used to parameterize the range-energy curve in the form of $T = a \cdot R^b$, where T is the kinetic energy, R refers to the range, and a and b stand for the parameterizing coefficients presented in Table 3.1. The flight direction of Λ was found from the decay points of Ξ^- and Λ. Once the proton energy and Λ flight-direction were known, the Λ mass was reconstructed by considering the momentum balance of the proton and π^-, where masses of the proton and π^- were fed into the calculation as the input constants. Figure 3.21 shows the reconstructed mass of Λ. The resolution of 10 MeV/c^2 was obtained.

	π^-	proton	Σ^-	Ξ^-
a	14.1	32.5	36.3	38.0
b	0.5653	0.5553	0.5535	0.5521

Table 3.1: The coefficients a and b for the parameterization of the range-energy curve in the form of $T = a \cdot R^b$, where T is the kinetic energy in MeV and R is the range in cm.

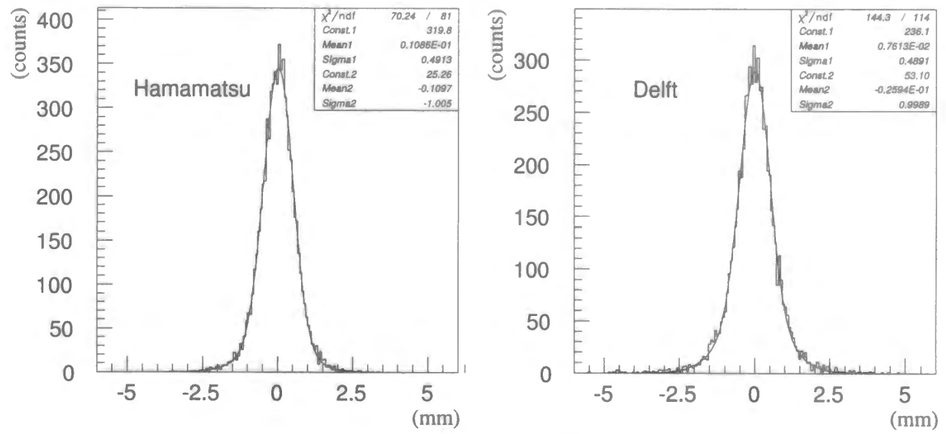

Figure 3.18: Deviation of the center of photon clusters around the straight-fitted line. The position resolution of 490 μm was obtained.

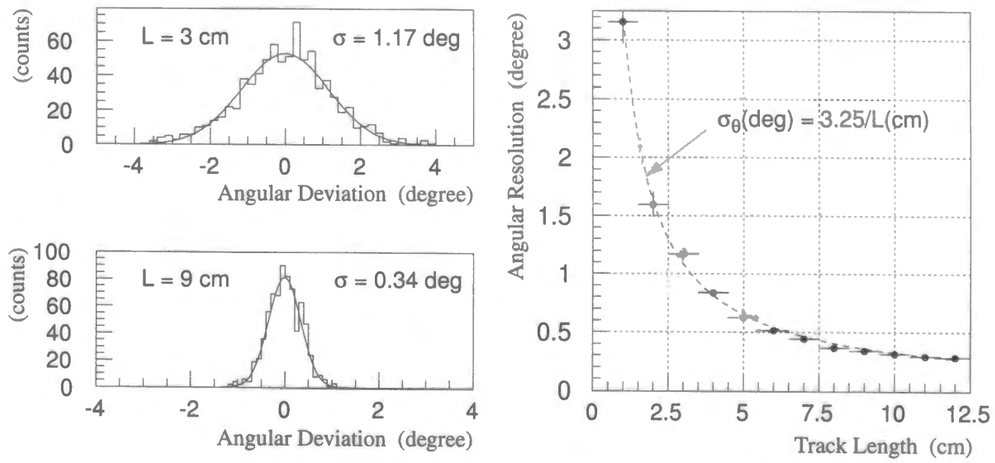

Figure 3.19: Left : Angular deviation of the straight-line fit of the track in the image data compared to the predicted track by drift chambers for the cases of the track-length of 3 cm and 9 cm. Right : Angular resolution of the straight-line fit of the image data as a function of the track length.

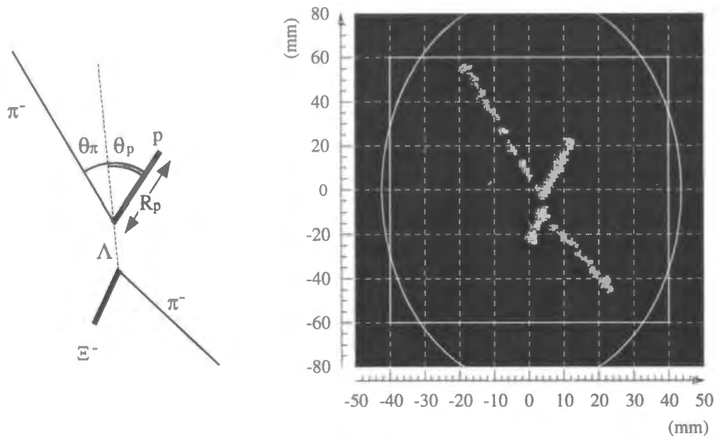

Figure 3.20: Example of the Ξ^- decay sample used for the Λ mass reconstruction.

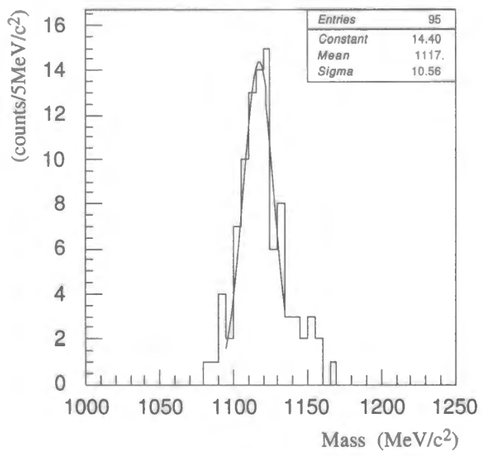

Figure 3.21: Reconstructed Λ mass spectrum.

3.11 Monte Carlo simulation of the (K^-, K^+) reaction

According to our experimental setup, a Monte Carlo simulation of the (K^-, K^+) reaction was developed so as to reproduce our experimental spectrum. It included the measured field map of the 48D48 magnet and efficiencies of the detectors as well as the geometric acceptance of the detector setup. The momentum and spatial distributions of the incident K^- beam were also taken into account. In order to simulate quasi-free reactions, Fermi motion of protons in a carbon nucleus was also simulated by using a simple harmonic-oscillator wave function, which introduces the following momentum distribution:

$$f(|p|) = \begin{cases} C_1 p^2 \mathrm{e}^{-b^2p^2} & (s \text{ orbit}) \\ C_2 p^4 \mathrm{e}^{-b^2p^2} & (p \text{ orbit}) \end{cases}, \tag{3.27}$$

where C_1 and C_2 are normalization factors and the oscillator parameter b was chosen to be 1.88 fm [128]. Comparison between the data and the Monte Carlo simulation is shown in Figure 3.22 in terms of the missing mass for $^{12}\mathrm{C}(K^-, K^+)X$ and the K^+ momentum. The solid line shows the Monte Carlo simulation, while the error bars represent the experimental data. The Gaussian resolution of missing-mass, which is discussed in Section 3.12.3, was taken into account. It was found the Monte Carlo simulation reproduces the experimental data well. Some discrepancy in the low-mass region of the missing-mass spectrum (Figure 3.22(a)) was resolved when applying tight cuts mentioned in Section 3.12.1 (Figure 3.22(a′)).

In simulating the quasi-free Ξ^- production, $K^- + (p) \to K^+ + \Xi^-$, the recoiled Ξ^- was traced to simulate the Ξ^- stopping by means of the continuous energy loss and the competing weak decay, $\Xi^- \to \Lambda\pi^-$. The emission probability of Ξ^- from the carbon nucleus, which was measured as 0.801 ± 0.024 [74], was also included. The obtained distributions of the (K^-, K^+) events which provide stopped Ξ^-'s are displayed with the shaded area in Figure 3.22. Consequently, the Ξ^- stopping probability was estimated to be 7.4 % against the total (K^-, K^+) reactions accepted by the spectrometer.

Although the direct measurement of the Ξ^- stopping rate was not available in this experiment, two cases were reported with respect to the comparison between the data and simulation. One is the experiment with the emulsion target (KEK-E176). The Ξ^- stopping rate of 14% was obtained from the data, while 9% was obtained from the simulation [129]. The deceleration of Ξ^- when emerging from the nuclei due to Coulomb attraction, nuclear potential, secondary scattering, etc, is one of the possible reasons of this difference as well as the simplicity of the Fermi motion of protons. The other experiment is the one in which the scintillating-fiber target was used (KEK-E224). This experiment showed the Ξ^- stopping rate of 1.22% and 1.34% for the data and the simulation respectively [130, 131]. The experimental value was evaluated from the visible energy release at the (K^-, K^+) reaction vertex, and thus it is possible to have missed the events accompanying neutral particles. If the neutral particles carry out a part of the energy release, the range of the stopped Ξ^- becomes shorter, and the Ξ^- is regarded as having interacted or decayed before stopping. In that sense, the experimental value can be considered as the minimum of the stopping rate. Including the above errors of the simulation against the data and also the

error of the escaping probability from the carbon nucleus into the systematic errors, the stopping probability of Ξ^- was evaluated to be $7.4^{+4.1}_{-0.7}$ %. Recently, the measurement of the Ξ^- momentum distribution for the (K^-, K^+) reaction on ^{12}C was reported in Ref. [131] with the incident K^- momentum of 1.65 GeV/c. It implies that the measured distribution lies in the lower momenta by ~100 MeV/c than the simulated distribution with use of the harmonic-oscillator nuclear model. If this tendency holds at 1.8 GeV/c K^-, the Ξ^- stopping rate would be larger than we have estimated here.

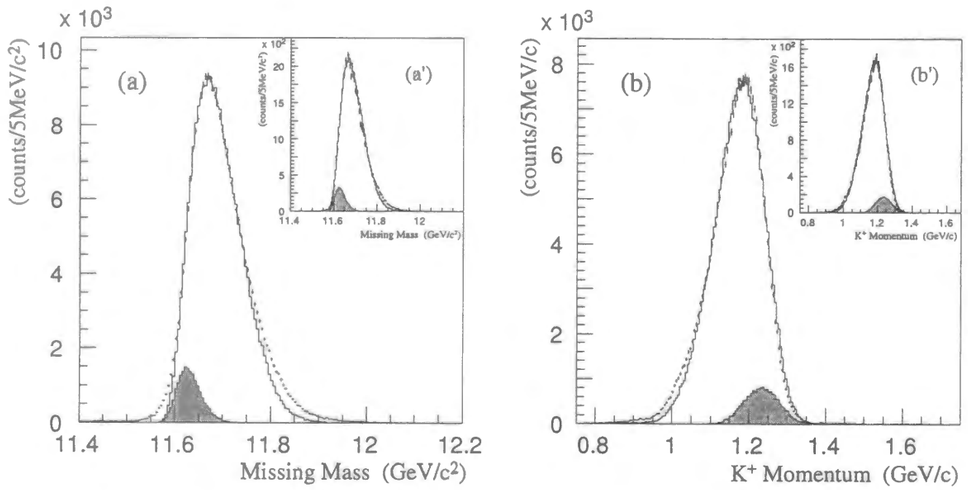

Figure 3.22: Comparison between the Monte Carlo simulation and the experimental data in terms of (a): the missing mass for ^{12}C(K^-, K^+) kinematics and (b): the K^+ momentum. The solid lines show the simulation results and the error bars show the experimental data. Relatively loose cuts were applied to produce the data histograms of (a) and (b), while quite tight cuts were applied for (a′) and (b′) (see the text).

3.12 Search for the direct H production in the (K^-, K^+) reaction

The production of the H-dibaryon could occur via the (K^-, K^+) reaction on two protons in a nucleus:

$$K^- + (pp) \rightarrow K^+ + H. \tag{3.28}$$

Aerts and Dover have calculated the direct H production on ^{3}He [111] and they suggested a peak structure in the spectrum of the K^+ momentum and/or the (K^-, K^+) missing mass. The peak would be well-separated from that of the quasi-free Ξ^- production if the H is sufficiently light. Considering the quasi-free reaction of Eq. (3.28) in the elementary process of the H production, the similar peak structure would be also expected in the case of a ^{12}C target. The data analysis to search for the direct H production in ^{12}C(K^-, K^+) is described in this section.

3.12.1 Cut studies

In order to suppress backgrounds caused from the event reconstruction failures and the misidentification of pions and protons as kaons, a series of tight cuts was applied. The followings are the summary of the cuts:

1. $\pm 2\sigma$ cut on the reconstructed outgoing particle's mass: less than 0.53 GeV/c^2 and greater than 0.45 GeV/c^2.
2. The ADC channels of the IC and FC aerogel Čerenkov counters are less than 350 after the 60Hz-AC-noise correction. These thresholds correspond to the rejection efficiencies of 99.82% for π^-'s and 99.99% for π^+'s.
3. Flight-path-length-corrected TOF in the beam line between MT and IT is consistent with the beam particle being a K^- within a 1 ns window.
4. Only one hit or two hits in adjacent elements in MP within a 5 ns window.
5. Time of MP hit within a 2 ns window from the expected time.
6. Events for which beam momentum reconstruction failed are rejected.
7. (K^-, K^+) vertex cuts:
   - 3σ vertex z-position cut around the centroid of the vertex z-position distribution, which had the dependence on the K^+ scattering angle θ_{K^+}. The distribution width in σ changed from 1.9 cm for large angles to 4 cm for small angles ($\theta_{K^+} < 3°$).
   - Vertex x-position less than 5 cm from the target center: less than 5 cm and greater than -5 cm.

- Vertex y-position less than 0.4 cm from the target center.
- Distance of closest approach between the K^- and K^+ trajectories less than 0.5 cm.

8. Distance between the chamber-tracking-projection onto BT and the BT hit position calculated from the time difference of two PMTs at both ends of the scintillator log was required to be less than 10 cm in both x and y.
9. All four FD3 planes must have a hit.
10. Goodness-of-fit of the outgoing particles is less than 50.
11. Beam-track projection onto IT must be consistent with the IT element being hit.
12. Beam-track χ^2 less than 5.

The reduction of event counts owing to application of the above cuts is summarized in Table 3.2. The events were divided into four groups in terms of the excitation energy, of which detail is described in the next subsection, with the corresponding processes of interest. The number of primary (K^-, K^+) candidates was 316,967 as mentioned in Section 3.8, while the number of events after the cuts were 53,243.

Excitation energy (MeV)	Number of events		Remaining rate (%)	Production process of interest
	before cuts	after cuts		
~ -350	4,302	11	0.26	–
$-350 \sim -40$	5,691	21	0.37	deeply bound H
$-40 \sim 0$	2,847	77	2.71	$\Xi^-/\Lambda\Lambda$ hypernuclei, loosely bound H
$0 \sim$	304,127	53,134	17.48	quasi-free Ξ^-
Total	316,967	53,243	16.80	–

Table 3.2: Reduction of event counts due to application of the cuts. The events were divided into four groups in terms of the excitation energy with the corresponding processes of interest.

3.12.2 Excitation-energy spectrum

The missing mass for each event which passed the cuts described in the previous subsection was calculated and used to produce the excitation-energy spectrum of the $^{11}\mathrm{B}+\Xi^-$ system shown in Figure 3.23. This spectrum is equivalent to the missing mass spectrum whose origin was moved to the energy threshold to produce the ground state of $^{11}\mathrm{B}$ and a free Ξ^- in the final state of the (K^-, K^+) reaction. The dash-dotted lines show the expected peaks of the H production for several assumed H masses, which is described in the next section. The K^+ momentum spectrum with the same cuts is also shown in Figure 3.24, while Figure 3.25 represents the mass spectrum of outgoing particles with the same cuts except for the self cut. The region of the resulting excitation-energy spectrum which lies below zero is free from the large population of the quasi-free Ξ^- production, and thus can be investigated for signals of the production of the H-dibaryon. The position of the peak could be used to determine the H mass.

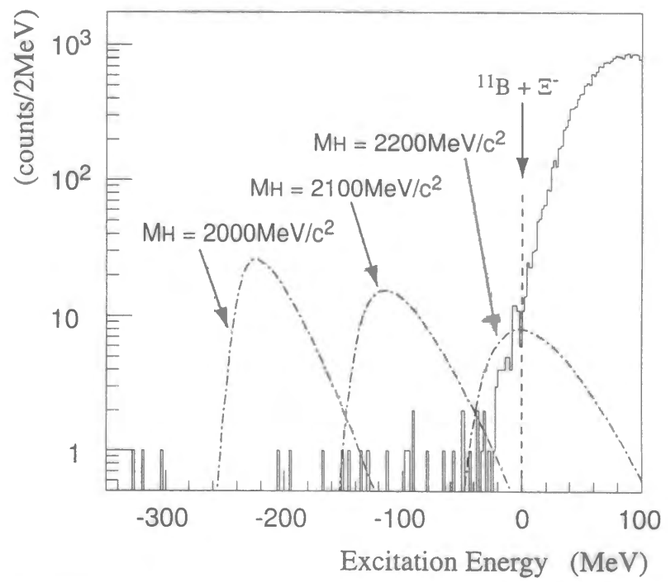

Figure 3.23: Excitation-energy spectrum of $^{11}\mathrm{B}+\Xi^-$ system. The origin corresponds to the energy threshold of $^{11}\mathrm{B}+\Xi^-$. The dash-dotted lines show the calculated peaks for H production which correspond to an assumed mass of 2000 MeV/c^2, 2100 MeV/c^2, and 2200 MeV/c^2.

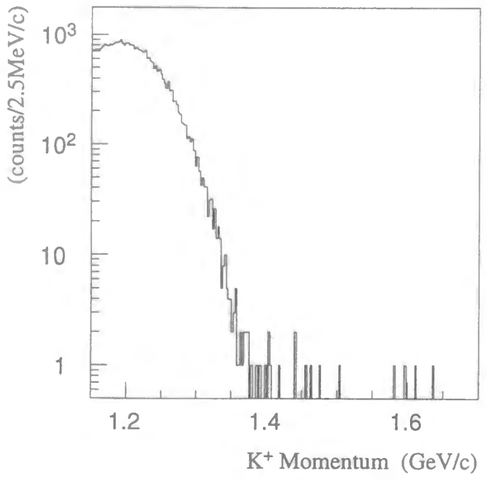

Figure 3.24: Momentum spectrum of the K^+ with the application of the same cuts used to produce Figure 3.23.

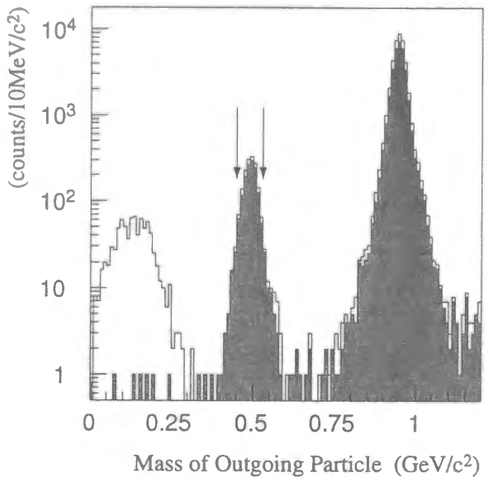

Figure 3.25: Mass spectrum of outgoing particles for a subset of the data. The shaded area shows the events which passed through the same cuts used to produce Figure 3.23 except for the self-cut, while the open area shows the events without the pulse height cut of the FC aerogel Čerenkov counter. The cut position on the outgoing particle is indicated by arrows.

3.12.3 Missing-mass resolution

The resolution of excitation energy or missing mass was studied by analyzing the data taken with polyethylene (CH_2) targets. Since hydrogens in the CH_2 target can be regarded as free protons, the Ξ^- production on hydrogen has a two-body nature, $p(K^-, K^+)\Xi^-$, and thus the resultant missing mass peak entirely corresponds to the experimental resolution. Two data sets were available for this analysis. One was obtained from an 8 cm long target, while the other was obtained from a 13 cm long target. Considering the 5 cm long diamond target in the production data taking, the 13 cm long CH_2 target is suitable for the resolution study because the material thickness is similar. However, since we found the statistics of data with the 13 cm long CH_2 target was not enough, the data set of the 13 cm long target was used to obtain the resolution function, while that of the 8 cm long target was just used to evaluate the resolution width. Figure 3.26 shows the missing mass spectrum for the kinematics of $p(K^-, K^+)X$ on hydrogen targets with application of the same cuts mentioned in Section 3.12.1. The carbon contribution was subtracted using data from the diamond target. We found that the peak can be well-fitted with a single Gaussian with 3.8 MeV/c^2 r.m.s. width. This parameterization is found to work well even in the tail

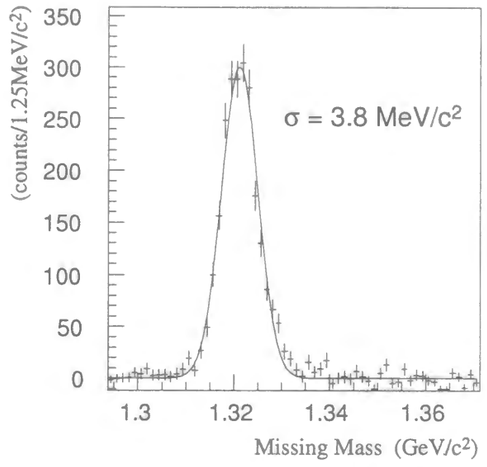

Figure 3.26: Missing mass spectrum for $p(K^-, K^+)X$ kinematics on hydrogen in the 8 cm long CH_2 target. The carbon contribution was subtracted using data from the diamond target. The peak was well-fitted with a single Gaussian with 3.8 MeV/c^2 r.m.s. width.

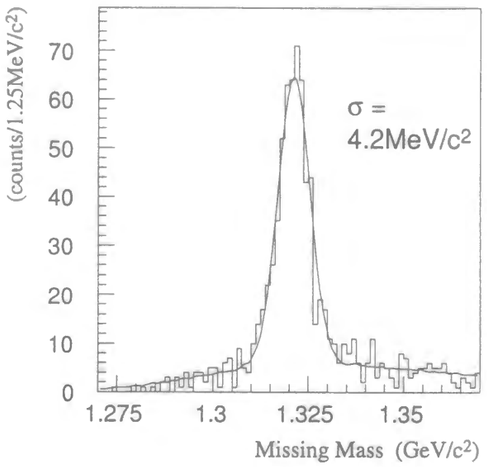

Figure 3.27: Missing mass spectrum for $p(K^-, K^+)X$ kinematics on hydrogen in the 13 cm long CH_2 target. The carbon contribution was not subtracted. The resolution width of 4.2 MeV/c^2 r.m.s. was obtained.

region. The missing mass spectrum for the 13 cm long CH_2 target with hydrogen-target kinematics is shown in Figure 3.27. The resolution width was measured to be 4.2 MeV/c^2 r.m.s. Taking the different kinematic factors for the two target-masses into consideration, the r.m.s. width of 4.2 MeV/c^2 for hydrogen corresponds to 6.1 MeV/c^2 for two-body kinematics on a ^{12}C target.

The K^+ momentum resolution ($\Delta p/p$) was derived to reproduce the above missing-mass resolution. It was found to be better than 0.53% in r.m.s. at $p_{K^+} = 1.2$ GeV/c. The absolute value of the missing mass was also adjusted with use of the missing-mass peak of the Ξ^- production on hydrogen. By applying the energy correction by -30 MeV to the energy of the outgoing K^+ originally measured with the spectrometer, the value for the peak center was obtained to be 1321.1 ± 0.1 MeV/c^2, while the world average of the Ξ^- mass is 1321.32 ± 0.13 MeV/c^2.

3.12.4 Comparison between the data and theory

Theoretical calculation

In order to compare the data and theory, the theoretical calculation of the H production in $^{12}C(K^-, K^+)H + {}^{10}Be^*$ was performed in terms of the cross section and the expected peak based on the scenario of Aerts and Dover [111]. In their model, a virtual Ξ^- is created off a

proton via the $p(K^-, K^+)\Xi^-$ reaction and fuses with a second proton to form the H. Their original calculation for the ^{3}He target was adapted for ^{12}C by assuming that only proton pairs in the relative $^1S_0$ state contribute to the H production and the residual ^{10}Be would behave as a spectator. This is the method adopted by Ahn *et al.* [71] and Nakano [70]. A calculation based on angular momentum algebra gives 3.17 $^1S_0$ proton-pairs in ^{12}C [70]. The absorption of incoming and outgoing kaons in a ^{12}C nucleus was also considered. Experimentally, this effect was derived by comparing the (K^-, K^+) cross sections on hydrogen and carbon targets [121]; the results are consistent with a theoretical DWIA calculation. We assumed that the absorption of kaons in the H production is the same as that in the quasi-free Ξ^- production. Considering the forward-angle cross section on hydrogen being 35 ± 4 μb/sr and that on carbon being 99 ± 4 μb/sr, the reduction factor of 0.47 was obtained. We also note that Aerts and Dover's calculation used a value of ~ 50 μb/sr at $p_{K^-} = 1.67$ GeV/c for free Ξ^- production on a proton, while a recent measurement found 35 μb/sr as mentioned above. These three factors were taken into account to derive our estimation of the cross section for H production off ^{12}C. Several expected peaks corresponding to several assumed H masses are superimposed on the excitation-energy spectrum in Figure 3.23. Despite reaching a sensitivity well below the theoretical predictions, no clear peak due to the H production was found.

Background studies

Although no peak structures were seen in the excitation-energy spectrum of $^{11}\mathrm{B}+\Xi^-$, there remained some events in the negative excitation-energy region which is of our interest. We first consider the deeply bound region where the $^{11}\mathrm{B} + \Xi^-$ excitation energy (E_{ex}) is less than -40 MeV. The reaction chains containing the $\bar{K}^0$-K^0 conversion are considered to have a sizable contribution to events in this region. The KEK-E224 reported that several events of this kind were observed using a scintillating-fiber active target with about ten times smaller statistics than ours [71, 72, 73]. The reaction chain having the largest cross section is

$$K^- + p \to \bar{K}^0 + n, \quad \bar{K}^0 \to K^0, \quad K^0 + p \to K^+ + n, \tag{3.29}$$

where the momentum transfer is almost zero in the forward-angle scattering and, the center of the distribution would be around $E_{ex} \approx -400$ MeV. Although the peak of this process is remote from the region of interest, a part of the distribution would give some contribution due to the Fermi momenta of protons in a ^{12}C nucleus. The smearing due to the Fermi motion was estimated at about 180 MeV FWHM, which was obtained from the double folding of the width of the quasi-free Ξ^- production. If one of the resulting neutrons in the reaction chain of Eq. (3.29) are replaced to a $\Delta(1232)$, namely:

$$K^- + p \to \bar{K}^0 + \Delta(1232)^0, \quad \bar{K}^0 \to K^0, \quad K^0 + p \to K^+ + n, \tag{3.30}$$

and

$$K^- + p \to \bar{K}^0 + n, \quad \bar{K}^0 \to K^0, \quad K^0 + p \to K^+ + \Delta(1232)^0, \tag{3.31}$$

the momentum transfer is about 360 MeV/c, and the center of the distribution would be around $E_{ex} \approx -60$ MeV, which is in the region under consideration. The distribution width

should be contributed from the natural width of $\Delta(1232)$ ($\approx$ 120 MeV FWHM) and the Fermi motion of protons mentioned above. The total width was estimated to be 240 MeV FWHM as a combined width of the two contributions. As $\Delta(1232)$ induced reactions, the following reactions are also possible:

$$K^- + n \to \bar{K}^0 + \Delta(1232)^-, \quad \bar{K}^0 \to K^0, \quad K^0 + p \to K^+ + n\,, \tag{3.32}$$

$$K^- + p \to \bar{K}^0 + n, \quad \bar{K}^0 \to K^0, \quad K^0 + n \to K^+ + \Delta(1232)^-. \tag{3.33}$$

The cross sections are considered to be similar to those in Eqs. (3.30) and (3.31). Using the cross section data in Refs. [132, 133, 134] and also assuming the effective proton number to be the same as that of the (K^-, K^+) reaction, the number of entries due to the above processes was estimated to be 8.8 ± 1.7 for (3.29) and 11.4 ± 10.0 for the sum of (3.30)-(3.33). According to the above discussion about the distribution width, 8.0$\pm$5.1 events were expected to be in the region -350 MeV $< E_{ex} < -40$ MeV as a total contribution from the reaction chains including the $\bar{K}^0$-K^0 conversion. The large systematic error is due to the poor statistics of existing data of Δ production through the kaon-nucleon reaction. In the above calculation, the angular distribution of every kaon-nucleon reaction was assumed to be same as that of $p(K^-, \bar{K}^0)n$, which was precisely measured in $1 \sim 2$ GeV/c momentum range of the incident K^- [132]. For the reaction $p(K^0, K^+)n$, the cross section of the inverse reaction was used. Also since there exist no data of the reactions $p(K^0, K^+)\Delta^0$ and $n(K^0, K^+)\Delta^-$, they were assumed to be same as those of $p(K^-, \bar{K}^0)\Delta^0$ and $n(K^-, \bar{K}^0)\Delta^-$.

The leaking of protons and π^+'s into the cut of the K^+ mass, greater than 0.45 GeV/c^2 and less than 0.53 GeV/c^2, is also one of the candidates of the sources. From the exponential extrapolations of mass spectra of the proton and the π^+ into the K^+ region, it was estimated at 5.9$\pm$5.7 protons and $(1.1\pm1.6)\times10^{-3}$ π^+'s in the region of -350 MeV $< E_{ex} < -40$ MeV. Another possible source is misidentification of π^- as K^- in the incident beam. The quasi-free peak of $(p)(\pi^-, K^+)\Sigma^-$ would be just above the $^{11}\mathrm{B} + \Xi^-$ threshold, where (p) refers to a proton in a carbon nucleus. By investigating the TOF spectrum of the beam particles, the number of misidentified events of π^- as K^- was estimated to be $(0.8 \pm 0.1) \times 10^{-2}$ in the same E_{ex} range. The errors resulted from the fitting uncertainty of the exponential tail. In consequence, the number of events resulting from all backgrounds discussed above was estimated to be 13.9 ± 7.6 in the region of -350 MeV $< E_{ex} < -40$ MeV, while 21 events remained in the same E_{ex} region of the data. Although it is difficult to make an exact estimation of the background, the events observed in the deeply bound region can be explained by the background discussed above.

Concerning a group of events just below the mass threshold of $^{11}\mathrm{B} + \Xi^-$ ($E_{ex} > -40$ MeV), they can be explained as Ξ hypernuclear states. Figure 3.28 shows the excitation-energy spectrum of $^{11}\mathrm{B} + \Xi^-$ around its threshold with several curves of the theoretical calculations by Motoba for the production of Ξ hypernuclei assuming several Woods-Saxon potential well depths ($V_{0\Xi}$). A good agreement between the data and theory was achieved in the case of $V_{0\Xi} = 14$ MeV [135]. Extrapolating the backgrounds discussed in the previous paragraph to this region, the contribution of those events was estimated to be 6.0$\pm$2.4. The leaking of quasi-free Ξ^- production due to the limited experimental resolution is another

source of the events in this region. The Monte Carlo simulation showed 8 events leaking to the region $E_{ex} < 0$. The coherent $\Lambda\Lambda$ production and the single-Λ hypernuclear production with a free Λ ($^{11}_{\Lambda}\mathrm{Be} + \Lambda$) are also possible sources of background. Moreover, considering a little larger event density below the energy threshold of $^{11}_{\Lambda}\mathrm{Be} + \Lambda$ ($-40\,\mathrm{MeV} < E_{ex} < -30\,\mathrm{MeV}$) compared to the further deeply bound region, double-Λ hypernuclei ($^{12}_{\Lambda\Lambda}\mathrm{Be}$) may have been produced. Bound states of $^{12}_{\Lambda\Lambda}\mathrm{Be}$ are below the energy threshold of $^{10}\mathrm{Be} + 2\Lambda$ which lies 17 MeV below that of $^{11}\mathrm{B} + \Xi^-$. If the Λ-Λ interaction energy is assumed to be 5 MeV attractive as previously reported [104, 105, 106, 136], the signal of the ground state would appear at $E_{ex} = -42$ MeV, 25 MeV below the $^{10}\mathrm{Be} + 2\Lambda$ threshold. The details of this topic are described in Ref. [117]. However, it is also possible that H-dibaryons in shallow bound states or resonance states contribute to these events. Ahn *et al.* suggested evidence for a Λ-Λ resonance based on the study of a $\Lambda\Lambda$ invariant-mass spectrum [75]. If all of the events in the region of -40 MeV $< E_{ex} < 0$ are assumed to be generated via the direct H production, the experimental spectrum is well-fitted with a curve assuming the H

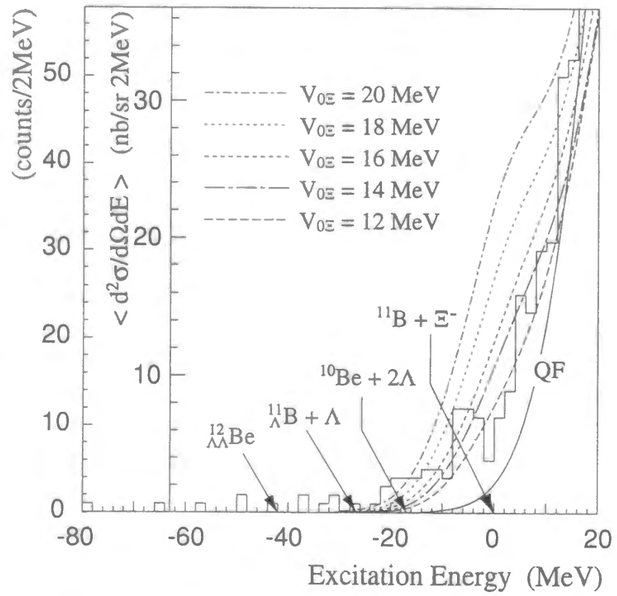

Figure 3.28: Excitation-energy spectrum of $^{11}\mathrm{B} + \Xi^-$ around the threshold with several curves of the theoretical calculations for Ξ^- hypernuclear production assuming Woods-Saxon potential. The curves in case of the Woods-Saxon potential well depth $V_{0\Xi} = 12$, 14, 16, 18, and 20 MeV are presented. The simulation result which contains the contribution of only quasi-free Ξ^- production is shown with the label "QF". The energy thresholds of $^{10}\mathrm{Be} + 2\Lambda$ and $^{11}_{\Lambda}\mathrm{B} + \Lambda$ and the expected location of the ground state of $^{12}_{\Lambda\Lambda}\mathrm{Be}$ are also indicated with arrows.

mass and forward-angle cross section to be 2220 MeV/c^2 and 0.6 μb/sr as shown in Figure 3.29. We had 33 events including image data from the SCIFI detectors in the region of $E_{ex} < 0$. Although the SCIFI detectors were not so sensitive in the forward region of the target, as seen in Section 2.9, those images were investigated to look for the decay tracks of the H. However, no images displaying $H \to \Sigma^- p$ or $\Lambda p \pi^-$ were found.

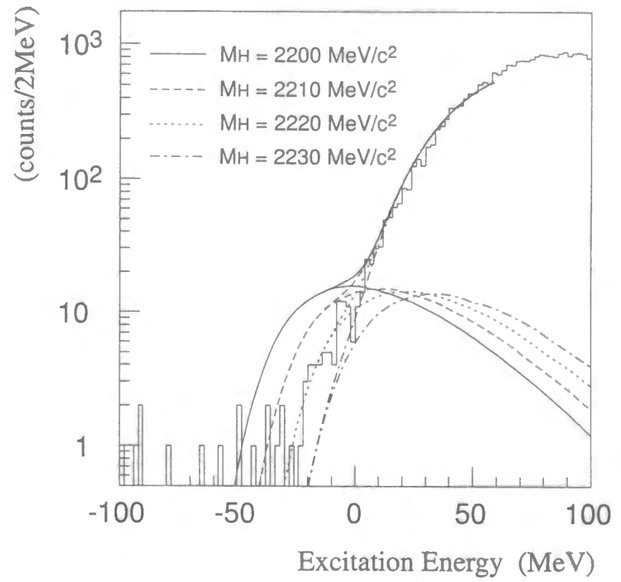

Figure 3.29: Excitation energy spectrum around $^{11}\mathrm{B} + \Xi^-$ threshold with several expected spectra of the H production. Spectra for the H mass of 2200 MeV/c^2, 2210 MeV/c^2, 2220 MeV/c^2, and 2230 MeV/c^2 are superimposed.

Upper limits

As a consequence of the above discussions, a 90% C.L. upper limit on the cross section for the direct H production was determined as a function of the H mass, which is shown in Figure 3.30. To avoid making assumptions regarding the shape of the background spectrum, no events were subtracted as background. This was done to produce the most conservative results for the upper limits. The K^+ scattering angle was averaged over $\theta_{K^+} < 14°$, which corresponds to our experimental acceptance. The upper limit was calculated by counting the events within $\pm\sigma$ from the maximum point of an assumed peak in the excitation-energy spectrum, then using Poisson statistics to determine the corresponding upper limit with 90% C.L. The results were then normalized by the known cross section of Ξ^- production on hydrogen, 35 ± 4 μb/sr [121]. The difference of the acceptance and detection efficiencies between the H production and Ξ^- production was taken into account. The details of this

normalization process are described in Appendix D. Thus the upper limit on the cross section can be expressed by:

$$\left.\frac{d\sigma}{d\Omega}\right|_{UL} = A(M_H) \cdot f(N)/\eta_s \ , \tag{3.34}$$

where $A(M_H)$ is the normalization factor of cross section per event, which is dependent on the H mass, $f(N)$ refers to the 90% C.L. upper limit with the Poisson statistics in the case of N events, and η_s stands for the area ratio of the fraction of $\pm\sigma$ to the total area of the expected peak. In the case of the assumed H mass of 2200 MeV/c^2, the normalization factor A(2200MeV/c^2) was calculated to be 0.978 nb/sr, for example. The resulting upper limits are in the range of a few nb/sr to 10 nb/sr for the H mass below 2100 MeV/c^2; upper limits of a couple of hundred nb/sr were obtained for the H mass of around 2200 MeV/c^2. The result is independent of lifetime and decay modes of the H. We note that the upper limits of the H mass less than 1960 MeV/c^2 were lowered by a factor of about 1.5 compared to the result reported in Ref. [117] due to the further background reduction. The dashed line shows a theoretical calculation for the ^{12}C target mentioned in the previous subsection, while the dotted line represents Aerts and Dover's calculation for the ^{3}He target. The latter was modified by replacing the Ξ^- production cross section with the recent measurement [121] in the same manner as we derived the former one. Our upper limits are fifty times lower than the theoretical calculation in the deeply bound region. The statistical error of 7% was estimated due to the limited amount of calibration data, while the systematic error was also obtained to be 11% from the uncertainty of the elementary cross section of Ξ^- production on hydrogen. It is noted that the uncertainty of the elementary cross section of Ξ^- production on hydrogen does not affect the comparison among the theoretical and experimental curves drawn in Figure 3.30 because all of them were derived by using the same value for the Ξ^- production cross section. Aizawa and Hirata also made a theoretical analysis of the reaction ^{3}He$(K^-, K^+)Hn$ with 1.8 GeV/c K^- by means of the nonrelativistic quark model [137] and predicted about twice larger cross section than Aerts and Dover's calculation.

Recently, Ahn *et al.* reported upper limits on the cross section for the direct H production in the (K^-, K^+) reaction on ^{12}C using a scintillating-fiber live target (KEK-PS E224) [71], which is superimposed with a dash-dotted line in Figure 3.30. Our upper limit is significantly lower than the E224 result (up to one order of magnitude at some masses). Also Stotzer *et al.* obtained upper limits on the cross section of ^{3}He$(K^-, K^+)Hn$ as shown in Figure 3.30 with a wider dash-dotted line (BNL-E836) [83]. The reaction is the one actually calculated by Aerts and Dover. The upper limits obtained from our data for H production off ^{12}C can be compared to the upper limits obtained by Ref. [83] for H production off ^{3}He by considering the ratio of the experimental upper limits to the theoretical calculation. We have achieved the lowest limit on the direct H production in the deeply bound region in terms of this ratio.

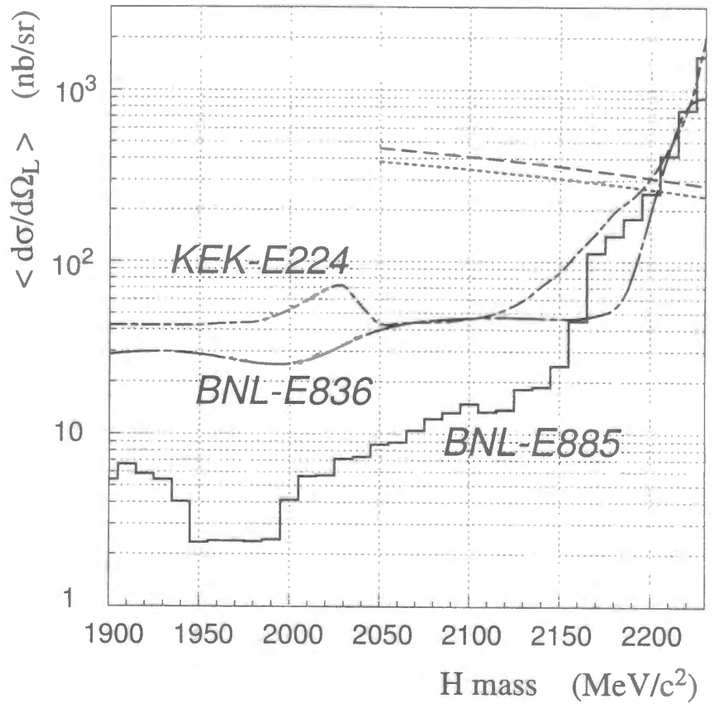

Figure 3.30: 90% C.L. upper limits on the direct H production cross section on ^{12}C. The dashed line shows a theoretical calculation based on the model of Aerts and Dover, while the dotted line represents a modified calculation of Aerts and Dover for the ^{3}He target (see the text). The results of the KEK-E224 and BNL-E836 are shown with a dash-dotted line and a wider dash-dotted line respectively (see the text). It should be noted that the upper limits of the H mass less than 1960 MeV/c^2 were lowered by a factor of about 1.5 compared to the result reported in Ref. [117] due to the further background reduction.

3.13 Search for the H-dibaryon via the atomic capture of stopped Ξ^-

H-dibaryons which were expected to be formed via the atomic capture of stopped Ξ^-'s on carbon nuclei were searched for using the data of the SCIFI detectors and the neutron counter arrays as well as the detectors in the (K^-, K^+) spectrometer.

3.13.1 Primary cuts

In order not to reduce the statistics, the primary cuts applied to this analysis for making a sample of (K^-, K^+) reactions were relatively loose. They included tighter cuts on the z vertex and outgoing-particle mass, shown in Figure 3.31, in addition to the basic cuts applied in the data reduction. As a result of the cuts, 274,798 (K^-, K^+) candidates were obtained, among which 90,683 events included the image data. This number discrepancy between the counter data and the SCIFI image data was caused by the additional matrix coincidence trigger and large dead time of the IIT system, which was mentioned in Section 2.9.2 and 2.10.3. In order to make an efficient analysis, the (K^-, K^+) events were divided into two groups in accordance with the results of the Monte Carlo simulation described in Section 3.11, as presented in Figure 3.32. Note that another long-tail Gaussian resolution function was incorporated to this simulation in addition to the intrinsic 6.1 MeV resolution so as to obtain a good agreement at the lower tail compared to Figure 3.22. One of the

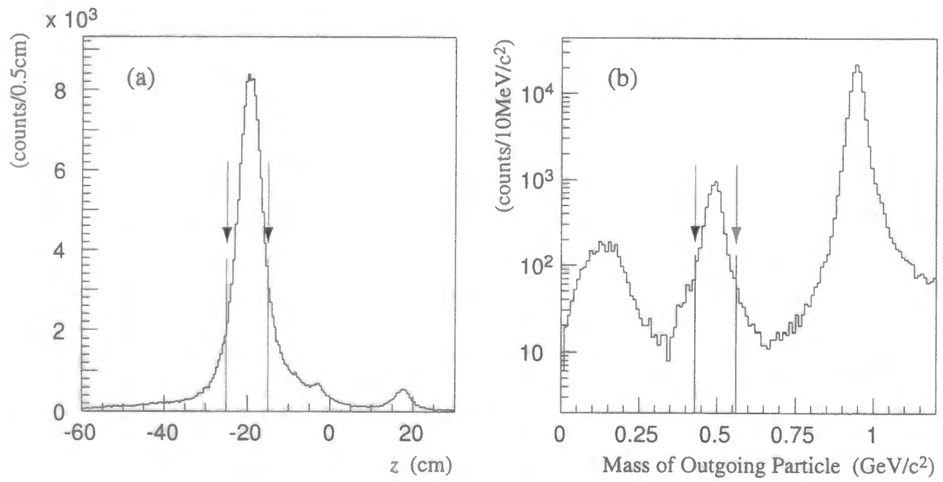

Figure 3.31: Cuts on the z vertex (a) and outgoing-particle mass (b) which was applied for the analysis on the atomic capture of stopped Ξ^- in addition to the basic cuts of the data reduction.

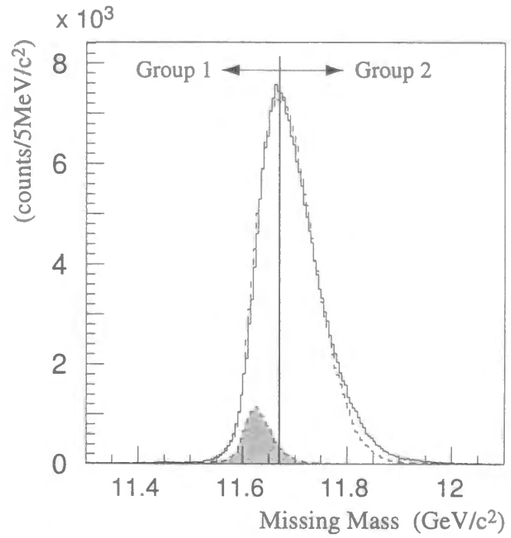

Figure 3.32: Missing-mass spectrum with $^{12}C(K^-, K^+)$ kinematics. The dashed line shows the Monte Carlo simulation, and the shaded area corresponds to stopped Ξ^-'s obtained from the simulation. The vertical line at 11.67 GeV/c^2 represents the cut position which divided into two analysis groups (see the text).

two groups consisted of the events whose missing mass is less than 11.67 GeV/c^2 (Group 1), which have a large probability of stopped Ξ^- in the target, while the other consisted of the events whose missing mass is larger than 11.67 GeV/c^2 (Group 2). According to the simulation, 88% of total stopped Ξ^-'s are included in Group 1. The numbers of events with the image data were 39,697 and 50,986 in Group 1 and Group 2 respectively. The image data were then sent to the scanning process by human eyes for the purpose of the event categorization. The events in Group 1 were fully scanned, while those in Group 2 were scanned for monitoring after prescaling with the factor of about 1/10.

3.13.2 Eye scanning

Outline

The image data of about 45,000 events were sent to the scanning by human eyes as mentioned above. We called this process "eye scanning". A browsing software based on the HIGZ package was developed for this analysis, in which the images of u- and v-view of the SCIFI block were displayed side by side in the graphic window for both upper and lower SCIFI detectors. A routine work of the eye scanning started by finding tracks which have correspondence in the u- and v-view each other, that is, tracks having the same z-positions

of the end points and/or kinked points. It often happened that tracks appeared only in one view due to the hit in the "arm", formed by the SCIFI sheets extending out of the block. Such tracks are of no interest and had to be avoided. Then the tracks observed in both views were categorized into following six types:

- H : kinked-'V' track.
- V : 'V' track.
- S : stopping event in the fiducial of the SCIFI detector.
- P : penetrating event from the fiducial of the SCIFI detector.
- X : multiple tracks more than three from the same point.

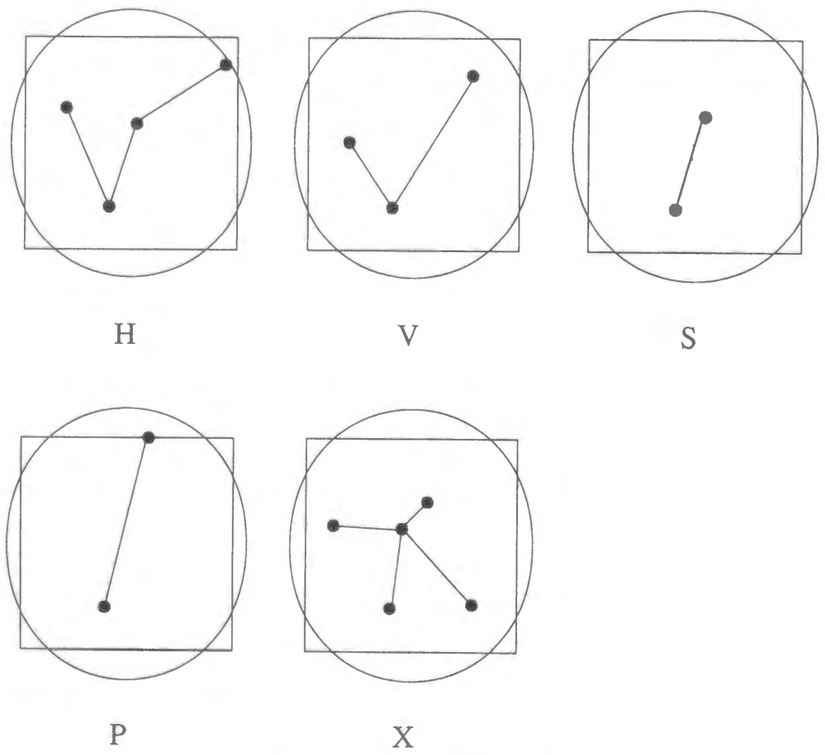

Figure 3.33: Event types which were used for category selection in the eye scanning of the image data. The closed circles stand for the marking positions to input the position information for each event category. The circle and rectangle of each category presentation show the fiducial edge of the IIT and SCIFI block respectively.

- O : others.

The candidates of $H \to \Sigma^- p$ are included in the H category, while the V category contains the decays of Λ's and Ξ^-'s. In the scanning process, several marks were put on the track so as to input the position information. Figure 3.33 shows the six category types and marking positions depending on the category. If there exist multiple events in one image, the category selection and track marking was made for all of them. The image was for example defined as "2V3S1P", which means the one included two 'V' tracks, three stopping tracks, and one penetrating track. As for the 'X' events, they were further classified in terms of the number of tracks as 'X3', 'X4', etc.

The scanning work was performed by the help of about twenty part-time workers for the period of seven months and a half. Table 3.3 shows the total result of event categorization by the eye scanning. Note that the sum of the event numbers do not amount to the number of total image data because the images often had multiple tracks which were categorized into different types.

category	number of event
H	653
V	8717
S	25215
P	24782
X3	313
X4	56
X5	4

Table 3.3: Result of event categorization by the eye scanning

Efficiency of eye-scanning

One of the most important things in the eye scanning was to evaluate the efficiency for classifying events into correct categories. The decays $\Lambda \to p\pi^-$ and $H \to \Sigma^-(\Sigma^- \to n\pi^-)p$ should be categorized as 'V' and 'H', respectively. We call this efficiency as 'recognizing efficiency' in this report. This was evaluated by mixing the simulation images into the real images to be scanned. The simulation images were made by utilizing the GEANT package in order to reproduce the physics processes that charged particles create photon images in the SCIFI detector. Some noise images were extracted from the real images in which no tracks were seen, and they were superimposed on the simulated images. A detailed description can be found in Ref. [73]. Figure 3.34 displays an example of the simulated image data of the Λ decay, and the corresponding recognizing efficiency is shown in Figure 3.35 as a function of the decay opening angle. The simulated Λ decay events were mixed into the real data randomly at the rate of one per ten events. When evaluating the efficiency, both of the proton and the π^- resulting from the Λ decay were required to have

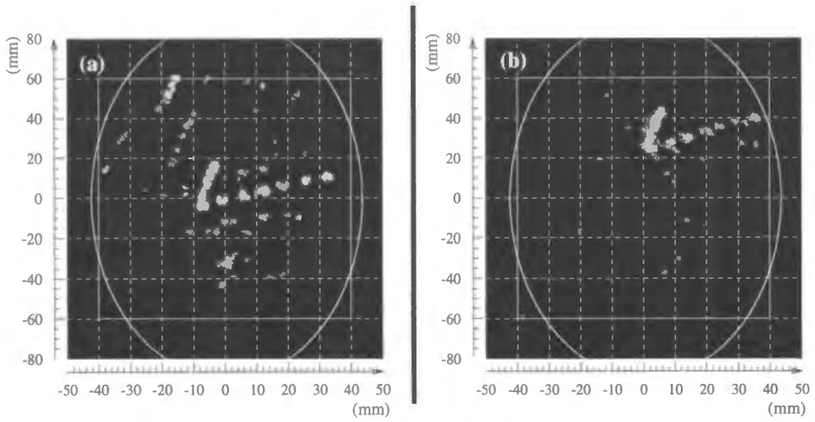

Figure 3.34: Example of the simulated image data of a Λ decay (a). The real data is also shown in (b) for the comparison.

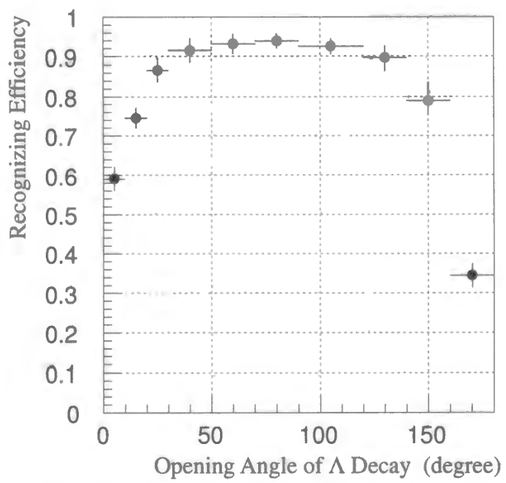

Figure 3.35: Recognizing efficiency of the eye scanning for Λ decay events as a function of the decay opening angle. Both of the proton and the π^- resulting from the Λ decay were required to have track length longer than 3.6 mm along the vertical direction to the SCIFI sheets.

track length longer than 3.6 mm along the z direction, the vertical direction to the SCIFI sheets. Except for the small ($\theta_\Lambda < 20°$) and large ($\theta_\Lambda > 160°$) angles, the recognizing efficiency was obtained in the range from 80% to 95%.

The events of $H \to \Sigma^-(\Sigma^- \to n\pi^-)p$ were also simulated and were mixed into the scanning images at the rate of one per a hundred events. Figure 3.36 shows an example of the simulated H event. The recognizing efficiency was investigated with the requirements that all the charged-particle tracks are longer than 3.6 mm along the z direction and 4.8 mm for the range, and the angles of $\angle(\Sigma^-, p)$ and $\angle(\Sigma^-, \pi^-)$ are larger than 20° and smaller than 160°. The simulated H's were generated for the masses (M_H) of 2150 MeV/c^2 and 2200 MeV/c^2; the recognizing efficiencies were found to be $22.7 \pm 8.9\%$ for $M_H = 2150$ MeV/c^2 and $20.6 \pm 6.9\%$ for $M_H = 2200$ MeV/c^2. No significant dependence on the H mass was found in spite of the different distribution of the decay angle and track length. Therefore, we evaluated the recognizing efficiency for the H events at $21.4 \pm 5.5\%$ for the whole H mass range. The relatively low efficiency was caused by the difficulty in finding the Σ^- tracks when they were short, and many of the H events were recognized as 'V' not 'H'.

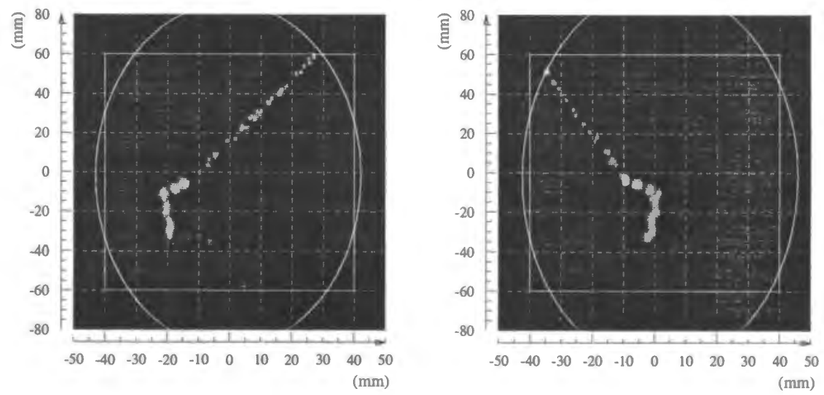

Figure 3.36: Example of the simulated image data for the sequential decay $H \to \Sigma^- p$, $\Sigma^- \to n\pi^-$. Two images correspond to the left and right views of the SCIFI block respectively.

3.13.3 Search for the H-dibaryon in $H \to \Sigma^- p$ decay

Cut studies

Since the decay of $H \to \Sigma^- p$ followed by $\Sigma^- \to n\pi^-$ presents a topology of kinked 'V', the H-dibaryon search was performed using the events which were recognized as 'H' by the eye-scanning. First of all, it was found that 129 events among 653 candidates were not kinked-'V' tracks by the careful rescanning. The unconnected 'V' and straight tracks were misidentified as kinked-'V' in those events. The remaining 524 events were further investigated by means of the following cut studies in order to suppress the backgrounds which give the same event topology.

1. The outgoing-particle momentum was required to be less than 1.4 GeV/c in order to select the quasi-free Ξ^- production events. (Figure 3.37).

2. Two kink points which correspond to the decay vertices of $H \to \Sigma^- p$ and $\Sigma^- \to n\pi^-$ are in the fiducial area of the SCIFI block. The fiducial edge was defined at 2 mm inside from the physical boundaries of either the SCIFI block or the IIT active area.

3. One of the particles at the ends of the kinked-'V' track was required to escape from the fiducial area of the SCIFI block. The π^-'s resulting from $\Sigma^- \to n\pi^-$ are energetic ($\sim$200 MeV/c) due to the large Q value of the decay, and thus most of them do not stop in the SCIFI block. We have observed 196 events in which both particles at the ends of the kinked-'V' track stopped in the SCIFI block. In most of these events, the tracks from the kink point were shorter than a few cm. Figure 3.38 shows an example of this kind of event. They can be considered as the Λ decay events followed by the p or π^- scattering, or the charged-particle evaporation from the π^- absorption in a ^{12}C nucleus.

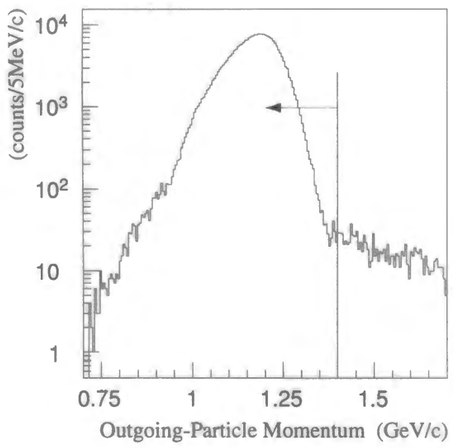

Figure 3.37: Momentum spectrum of the outgoing particles. The events with the momentum larger than 1.4 GeV/c were rejected.

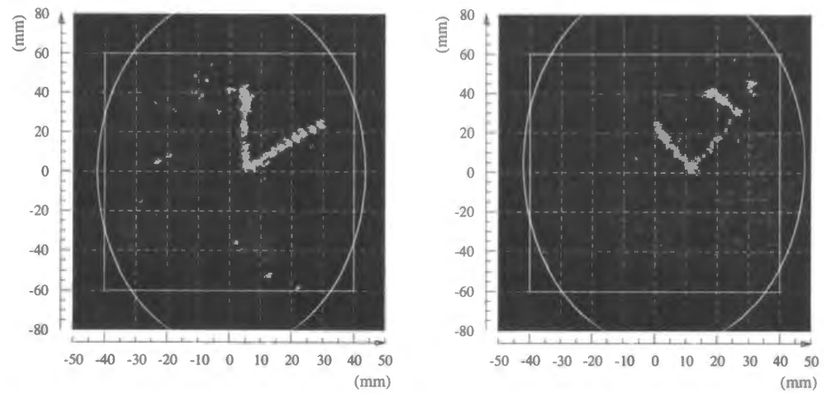

Figure 3.38: Example of the kinked-'V' track in which the particles at both ends stopped in the SCIFI block.

4. The particle at the other end was required to stop in the fiducial. The protons from $H \to \Sigma^- p$ stop in the SCIFI block with a high probability. This requirement was useful to suppress the Λ's which decayed near the fiducial edge and showed the kinked-'V' pattern as mentioned in the cut #3, and also to reject the beam-halo particles which scattered twice in the SCIFI block. We observed 112 events in which both particles at the ends of the kinked-'V' track escaped from the fiducial.

Satisfaction of the above requirements provides the unique assignment of Σ^-, proton, and π^- to the H candidates. Namely, the stopped track in the fiducial corresponds to a proton, the escaping track corresponds to a π^-, and the track between the above two tracks corresponds to a Σ^-. Using this particle assignment, the following further cut studies were performed.

5. The ranges of all the charged particles in the kinked-'V' track were required to be longer than 4.8 mm. Also, they should be across four sheets, two sheets in each view, of the SCIFI block at least, which corresponds to 3.6 mm along the z direction. This requirement is necessary to determine the track length and the flight direction. In addition, the π^--like track was required to be longer than 15 mm before escaping from the fiducial. The events which passed this requirement were fitted with straight lines and were sent to the next requirement.

6. The angle between the Σ^--like track and the proton-like track and that between the Σ^--like track and the π^--like track were required to be larger than 20° and smaller than 160°. This cut was applied based on the recognizing efficiency of the Λ decay events shown in Figure 3.35, which can be regarded as the efficiency for the kink pattern.

7. Using the track length of the proton- and Σ^--like particles and the opening angle between them, the H momentum can be reconstructed within a limited range on the assumption of the bound H[1]. We rejected the events which did not point back to the diamond target when considering the above reconstructed H momentum.

8. When the kinked-'V' events had charged hits on the neutron counter arrays of which hit positions were inconsistent with the π^--like track escaping from the SCIFI detector[2], and when the charged particles had β larger than 0.5, they were rejected from the H candidates. This cut was applied in order to reject π^-'s from $\Xi^- \to \Lambda\pi^-$. It is possible that the H formation from the $(\Xi^-,\ ^{12}\mathrm{C})_{atom}$ also accompanies relatively energetic charged particles. Among them, the proton from $(\Xi^-,\ ^{12}\mathrm{C})_{atom} \to H + {}^{10}\mathrm{Be(g.s.)} + p$ is the fastest. However, even when the H mass is assumed to be 2140 MeV/c^2 which is just above the $\Sigma^- + p$ threshold, the maximum β of the proton is 0.416. Taking the TOF resolution of the neutron counter arrays and the uncertainty of Ξ^- stopping time and position into account, this $\beta(= 0.416)$ is 5σ away from the cut position $\beta = 0.5$, and thus the probability to lose the H from the above process is negligible.

In consequence of the application of the above requirements, no events remained as a H candidate. Table 3.4 summarizes the event rejection in accordance with each cut.

Cut#	1	2	3	4	5	6	7	8	Total
Number of rejected events	5	13	196	112	104	50	43	1	524

Table 3.4: Summary of the event rejection in accordance with the requirements for the $H \to \Sigma^- p$ candidates.

Estimation of the number of stopped Ξ^-

In order to estimate the number of stopped Ξ^-, we begin with the estimation of background amount in the obtained (K^-, K^+) sample. The missing mass spectrum of the events which passed the primary cuts mentioned in Section 3.13.1 is presented in Figure 3.39 with a solid line, while the dashed line shows the missing mass in which the further cut on K^+ momentum ($p_{K^+} < 1.4$ GeV/c) was applied; this was included in the cut studies described in the previous part of this subsection. A long tail of the solid histogram in the low missing

[1]Using the range of the proton which stopped in the SCIFI block and the assumed H mass, the H momentum can be reconstructed. Considering the case of the H mass equal to that of two Λ's, the maximum momentum for the bound H is provided. On the other hand, the H momentum should be larger than that for the case that the Σ^--like particle stopped at the kink point. The direction of the "true" H momentum should be between the directions for the above two cases.

[2]The consistency was also checked with respect to the decay $\pi^- \to \mu^-\bar{\nu}_\mu$ as well as the primary decay $\Xi^- \to \Lambda\pi^-$.

mass region less than about 11.5 GeV/c^2 must be background, and its contribution to the quasi-free Ξ^- production peak has to be evaluated. This was done by looking into protons which were misidentified as kaons. As seen in the outgoing-particle mass spectrum in Figure 3.31, the majority of background events in the K^+ region are due to the proton leakage. A dotted line in Figure 3.39 represents the missing mass spectrum of protons with $^{12}\mathrm{C}(K^-, K^+)$ kinematics. The events of outgoing-particle mass greater than 0.7 GeV/c^2 and less than 1.1 GeV/c^2 in Figure 3.31 were selected out to produce the background sample of the missing-mass spectrum. It was scaled to fit the solid histogram. Comparing the solid histogram and the dotted one, it was found that the low missing-mass tail of the (K^-, K^+) sample can be explained as the proton contamination. The difference of the spectrum shape is understood by the fact that the momentum resolution becomes worse far from the center of the mass peak. The proton spectrum with the dotted histogram shows fairly flat in the missing-mass range where the image-data analysis was performed, about 11.4 GeV/c^2 $\sim$ 11.67 GeV/c^2, and 100 events per 10 MeV-wide bin are estimated there. The systematic error of 10% was estimated. Considering the ratio of the data including the SCIFI images to the total data, which is shown in Figure 3.40, the estimated amount of background in the scanned image-data with $p_{K^+} < 1.4$ GeV/c is 990 ± 100, while the number of total scanned image-data with the same K^+ momentum cut is 39,130. As for the pion contamination, the estimation with an assumption of an exponential tail in the mass spectrum in Figure 3.31 indicates 10 ± 10 events. Then the number of true (K^-, K^+) events is expected to be $38,130 \pm 100$.

The Monte Carlo simulation was utilized to obtain the stopping rate of Ξ^-'s in the diamond target among the image-scanned (K^-, K^+) sample in which the missing mass is less than 11.67 GeV/c^2. The simulation incorporated the energy-loss process using Bethe-Bloch formulae and the competing weak decay as described in Section 3.11. The Ξ^- emission probability from a carbon nucleus of $80.1 \pm 2.4\%$ [74] was also taken into account. Note that the stopping rate being discussed here is the ratio of the number of stopped Ξ^- to the number of (K^-, K^+) events accepted by the spectrometer. As a result, the Ξ^- stopping rate in the missing mass less than 11.67 GeV/c^2 was calculated as $16.8^{+9.3}_{-1.6}$ %, and the corresponding number of stopped Ξ^-'s was estimated to be 6,410 $\pm 80(\mathrm{stat.})^{+3,550}_{-600}(\mathrm{syst.})$ after rejecting the backgrounds mentioned above. The systematic error includes the difference between the data and the simulation reported in the previous experiments, which was discussed in Section 3.11, as well as errors on the measurement of the emission probability of Ξ^- from a carbon nucleus and the background estimation.

Upper limits

From the fact that no events of the $H \to \Sigma^- p$ candidates were found after the cut studies for the background rejection, we have set upper limits on the value R which stands for the product of the branching ratio of the H formation from $(\Xi^-,\ ^{12}\mathrm{C})_{atom}$ and that of the $H \to \Sigma^- p$ decay:

$$R = Br[(\Xi^-,\ ^{12}\mathrm{C})_{atom} \to HX] \cdot Br[H \to \Sigma^- p]. \tag{3.35}$$

Here, the residual of the H formation (X) was assumed to be ^{11}B(g.s.). The detection efficiency of $H \to \Sigma^- p$ with our experimental condition was calculated using the Monte Carlo simulation. Table 3.5 shows the detection sensitivity in the case of the H mass and lifetime of 2220 MeV/c^2 and 1.0 ns; the total sensitivity of ~0.3% was obtained. The sensitivity of the cut #7 was not 100% due to the limited resolution of the position and angular measurements with the SCIFI detector.

Then the upper limits on R was determined by the following equation:

$$R_{UL} = \frac{2.3}{N_{stop} \cdot \eta} \quad . \tag{3.36}$$

In Eq. (3.36), N_{stop} refers to the number of stopped Ξ^-'s in the scanned image data, and η shows the detection sensitivity. Figure 3.41 shows the obtained upper limits on R with 90% C.L. as a function of the H mass in the case of the H mass of 2220 MeV/c^2. Figure 3.42 exhibits a contour plot of the upper limits on R for the H masses from 2140 MeV/c^2 to 2230 MeV/c^2 with the H lifetimes from 0.1 ns to 10 ns. The upper limits are less than 30% in the region of the H lifetime 0.2 ~ 2 ns for the whole H mass range. Especially, we have obtained the upper limit of 10% for the H masses larger than 2220 MeV/c^2 and the H lifetimes of ~1 ns. The rapid increase of the upper limits in the lower lifetimes (0.1 ~ 0.2 ns) is due to the finite distance between the diamond target and the SCIFI detectors.

The upper limits of the same process were recently reported in Ref. [72], and the updated

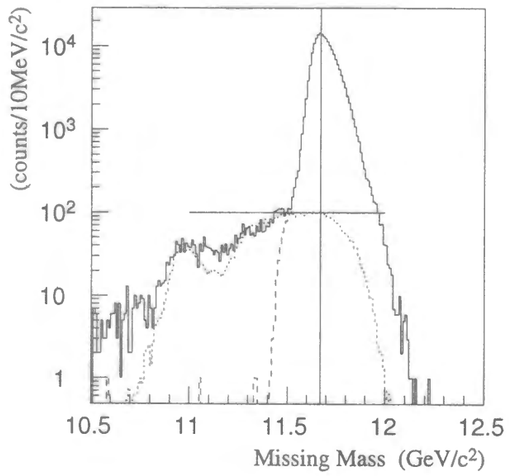

Figure 3.39: Missing mass spectrum of the (K^-, K^+) event sample. The solid line shows the one which passed the primary loose cuts described in Section 3.13.1, while the dashed line represents the one in which the further cut on K^+ momentum was applied. The dotted line shows the missing mass spectrum of protons with ^{12}C(K^-, K^+) kinematics scaled to fit the solid line (see the text).

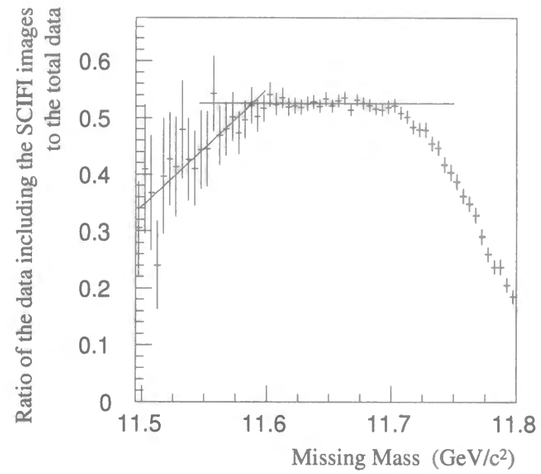

Figure 3.40: Ratio of the data including the SCIFI images to the total data as a function of the missing mass. The flat distribution of 52.5% was obtained in the region greater than 11.9 GeV/c^2 and less than 11.7 GeV/c^2. The decrease of the ratio on both sides is due to the additional matrix coincidence trigger (see Section 2.10). The missing mass of the image-scanned region is less than 11.67 GeV/c^2.

Criterion	Sensitivity of each cut[a]	Combined sensitivity
Cut #1	100%	100%
Cut #2	14.5%	14.5%
Cut #3	99.8%	14.4%
Cut #4	64.5%	9.31%
Cut #5	20.8%	1.93%
Cut #6	92.1%	1.78%
Cut #7	99.4%	1.77%
Cut #8	100%	1.77%
Recognition in the eye-scanning	21.4%	0.379%

Table 3.5: Detection sensitivity of $H \to \Sigma^- p$ events with a series of cuts in the case that the H mass and lifetime are 2220 MeV/c^2 and 1.0 ns respectively.

[a]Denoting the number of events which passed the 1-i th criteria by n_i, the sensitivity for the i th criterion was defined as n_i/n_{i-1}.

result in Refs. [130, 131]. Our result is at about the same level as theirs or up to twice better in the lifetime region of $0.5 \sim 1$ ns.

When Jaffe originally predicted the H-dibaryon, the branching ratios of several decay modes were also calculated. According to the calculation, the branching ratios were expected to be $5 : 3 : 2$ for $H \to \Sigma^- p$, $H \to \Sigma^0 n$, and $H \to \Lambda n$ respectively with the H mass of 2150 MeV/c^2 [1]. For the heavier H, the $\Sigma^- p$ mode would become dominant. If it is assumed that the decay branching ratio for $H \to \Sigma^- p$ is less than 50%, our obtained upper limits indicate that the H formation rate from the $(\Xi^-, {}^{12}\mathrm{C})_{atom}$ should be less than 20% for the H masses of $2220 \sim 2230$ MeV/c^2 with the H lifetimes of $\sim$1 ns. This is considerably lower than the predicted rates of the H formation from the $(\Xi^-, {}^{4}\mathrm{He})_{atom}$ by Aerts and Dover [114], which was more than 90% for the Nijmegen model-D potential.

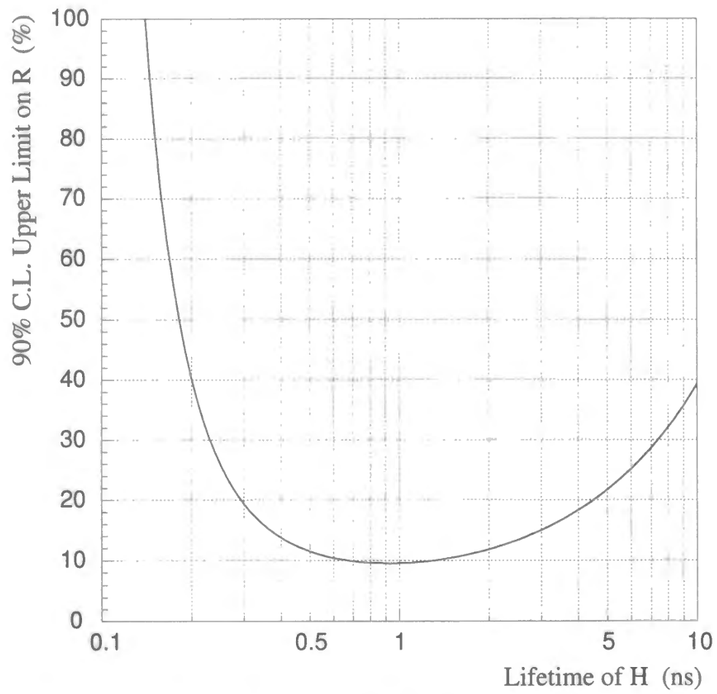

Figure 3.41: 90% C.L. upper limits on the product of the branching ratios, R $(= Br[(\Xi^-, {}^{12}\mathrm{C})_{atom} \to HX] \cdot Br[H \to \Sigma^- p])$, as a function of the H lifetime in the case of the H mass of 2220 MeV/c^2. The residual of the H formation (X) was assumed to be ^{11}B(g.s.).

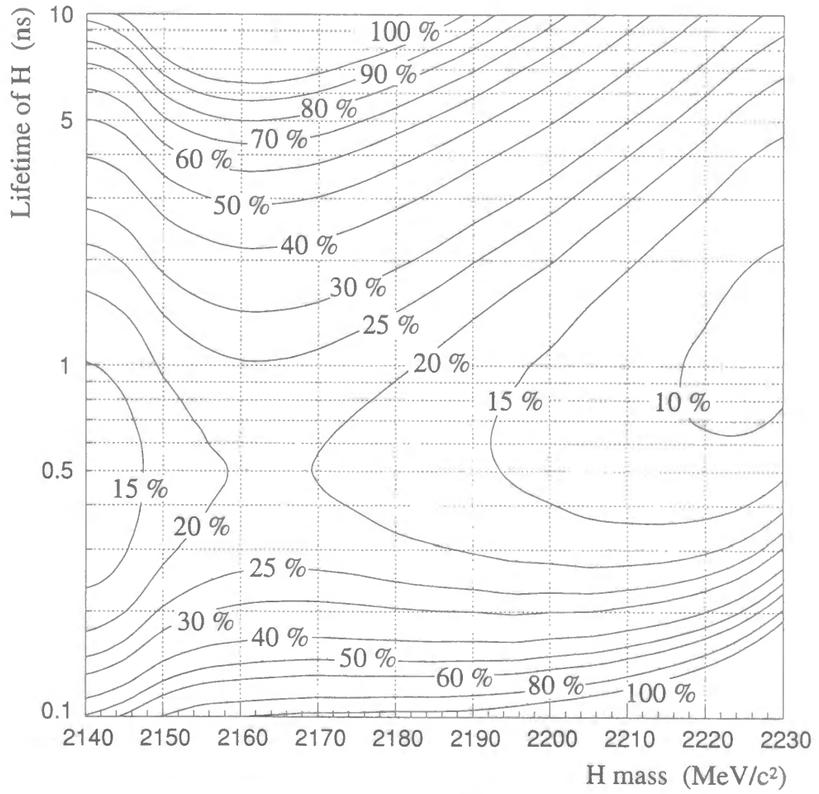

Figure 3.42: Contour plot of 90% C.L. upper limits on the product of the branching ratios, R $(= Br[(\Xi^-, {}^{12}\mathrm{C})_{atom} \to HX] \cdot Br[H \to \Sigma^- p])$, where X was assumed to be ^{11}B(g.s.).

3.13.4 Search for the H-dibaryon in $H \to \Lambda n$ decay

Kinematic reconstruction of $H \to \Lambda n$

By utilizing the ability to observe the Λ and the neutron with the SCIFI detector and the neutron counter arrays for each, the H-dibaryon was searched for by means of the mass reconstruction in $H \to \Lambda n$. The events which had 'V' tracks in the SCIFI image data in coincidence with neutral hits in the neutron counter arrays were extracted as a sample of this analysis. The neutral hits with $\beta^{-1} < 1.5$ were eliminated to discriminate γ's. All the 'V' tracks in this sample were assumed to be the charged Λ decay, $\Lambda \to p\pi^-$, and fitted with straight lines for the succeeding kinematic reconstruction. In order to reconstruct the H mass, the four-momentum of the Λ and neutron had to be known. To satisfy this condition, one of the two particles resulting from the Λ decay was required to stop in the SCIFI block. By assigning p and π^- to the 'V' track, the four-momentum of Λ was then calculated. Since the ambiguity of p/π^- assignment to the 'V' track remained, both cases were considered. For neutrons, the kinetic energy was measured by the TOF measurement, as described in Section 3.9.1. The hit position in the neutron counter was also measured from the time difference between the two PMTs coupled to both ends of the scintillator log. However, since both of the initial and final states are neutral in the decay of $H \to \Lambda n$, the decay point of the H was not able to be observed. Thus it was approximated to be at the same position as that of the Λ as shown in Figure 3.43. This approximation was based on the assumption of the H lifetime being comparable to the hyperon lifetimes. The position and time uncertainties of the H decay as well as the detector resolution were taken into account in estimating the expected peak of the H production.

Figure 3.44 shows the reconstructed H-mass spectrum which was obtained by the manner described above. Since the mass of $\Lambda + n$ is 2055.2 MeV/c^2, the backgrounds of low-energy neutrons resulting from the π^- capture etc. pile up at the threshold. The dashed line in Figure 3.44(right) represents the expected peak shape of the reconstructed H-mass spectrum for an assumed H mass of 2200 MeV/c^2, in which the detector resolution and the kinematic approximations mentioned above are incorporated. The approximations resulted in the shift of the peak center. The effects of multiple scattering and range struggling of the proton and π^- in the SCIFI block were also considered in the estimation.

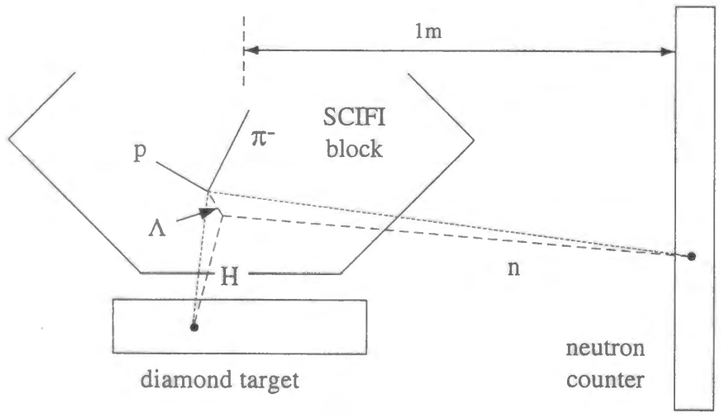

Figure 3.43: Schematic concept of the kinematic reconstruction of $H \to \Lambda n$. Since the H decay point cannot be observed because both of the initial and the final states are neutral, it was approximated to be at the same point as that of the Λ.

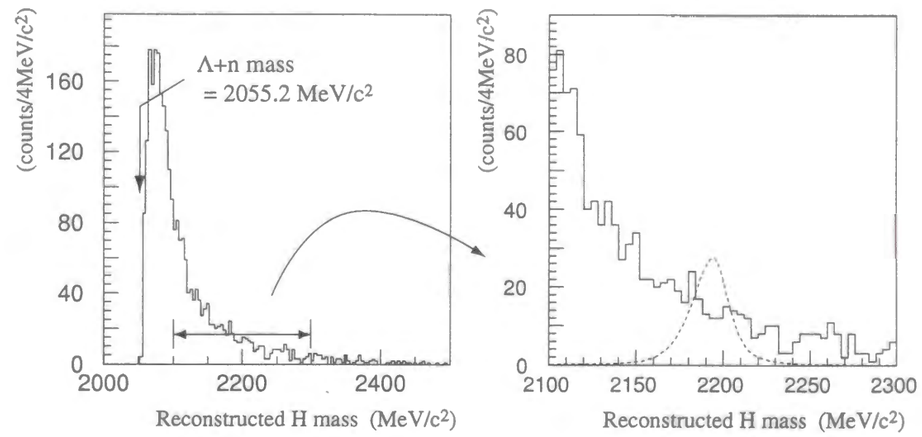

Figure 3.44: Reconstructed H-mass spectrum in the $H \to \Lambda n$ kinematics in a whole range (left) and with the magnified view in a range from 2100 MeV/c^2 to 2300 MeV/c^2 (right). The dashed line in the right figure represents the expected peak shape of the reconstructed H-mass spectrum for an assumed H mass of 2200 MeV/c^2. The peak size is arbitrary. The shift of the peak center is due to the kinematic approximation in the mass reconstruction.

Cut studies

In order to reduce the backgrounds, the events were required to pass the following cuts.

1. The outgoing-particle momentum was required to be less than 1.4 GeV/c. (Figure 3.37)

2. Energy deposit of neutrons in the neutron counter arrays was required to be larger then 2 MeVee and less than the neutron kinetic energy which was calculated from the time-of-flight as shown in Figure 3.45. Neutrons from the $H \to \Lambda n$ decay are expected to be relatively energetic because of the large Q value. The neutron kinetic energy is ~100 MeV in the case of the H mass of 2200 MeV/c^2, for example. According to Figure 2.12 in Section 2.8, the neutron detection efficiency doesn't decrease so much when setting higher energy-deposit threshold in the neutron kinetic energy range

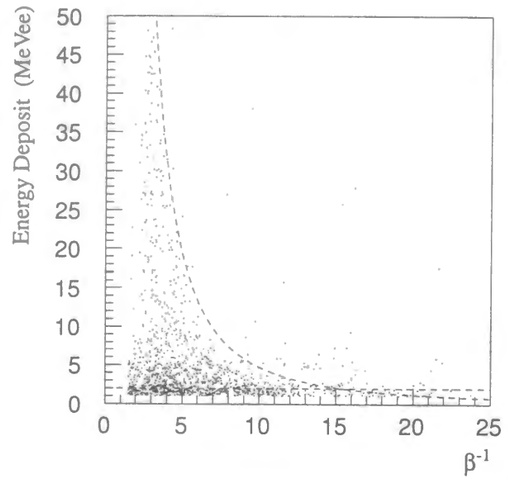

Figure 3.45: Neutron distribution in β^{-1} versus energy-deposit in the neutron counter arrays. The dashed lines show the required cut position.

larger than 50 MeV. However, it was found that 3 MeVee threshold was not effective for the further background reduction.

3. Neutrons with $\beta^{-1} < 5$ were accepted since β^{-1} of neutrons resulting from the H decay is expected around $2 \sim 3$. Figure 3.46 shows the simulated β^{-1} spectrum in $H \to \Lambda n$ decay, while Figure 3.47 shows the experimental β^{-1} distribution of the current analysis sample.

4. Both charged particles in the 'V' track images should travel four sheets, two sheets in each view, of the SCIFI block at least, which corresponds to 3.6 mm along the z direction. This requirement is the one which was also used in the analysis of the $H \to \Sigma^- p$ mode (cut #5) in the previous subsection.

5. The following relation between the reconstructed H momentum and the decay position was required.

$$\begin{aligned} y\text{-component of the } H \text{ momentum} > 0 &\leftrightarrow \text{ decay at } y > 0 \\ < 0 &\leftrightarrow \qquad\qquad < 0 \end{aligned}$$

Namely, since the center of the diamond target was positioned at $y = 0$, this requirement means that the H should decay in the positive y region when the H goes up, while the H should decay in the negative y region when the H goes down. However, due to the kinematically approximated reconstruction, this is not always true.

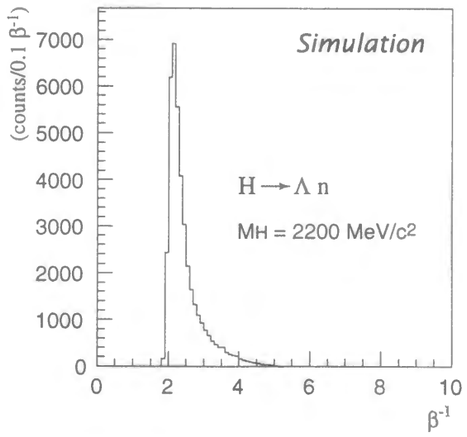

Figure 3.46: Simulated β^{-1} spectrum in $H \to \Lambda n$ decay with an assumed H mass of 2200 MeV/c^2.

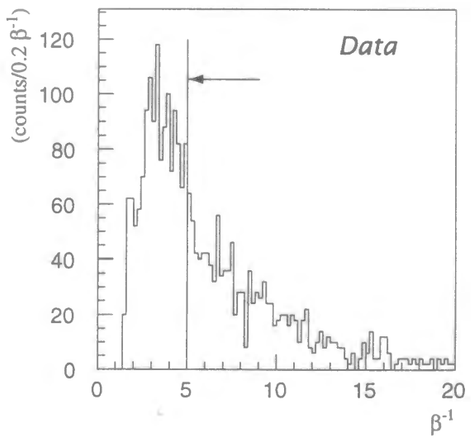

Figure 3.47: Experimental β^{-1} distribution of the current analysis sample. The solid line shows the cut position.

The cut efficiency was estimated by the Monte Carlo simulation as described later. Figure 3.48 shows the distribution of the y coordinate of the H decay vertex, which was assumed to be at the same position as that of Λ, versus the y-component of the reconstructed H momentum. The first and third quadrants are the allowed region.

6. The kinetic energy of the H will be maximum when the final state of the H formation from the $(\Xi^-, {}^{12}\mathrm{C})_{atom}$ is $H + {}^{11}\mathrm{B}$(g.s.). In the case of the H mass of 2200 MeV/c^2, the simulated spectrum of the reconstructed kinetic energy of the H with the final state of $H + {}^{11}\mathrm{B}$(g.s.) is shown Figure 3.49. The events with the kinetic energy less than 50 MeV were accepted.

7. The 'V' events with tracks penetrating from the base plane of the SCIFI block were rejected in order to eliminate Ξ^-'s which came into the SCIFI block via the base plane and decayed in the SCIFI block as displayed in Figure 3.51. This kind of events were categorized as 'V' in the eye scanning. When the resultant Λ decays into neutrals or decays out of the SCIFI block, the Ξ^- decay track gives the same topology as that of Λ decay and is included as a background.

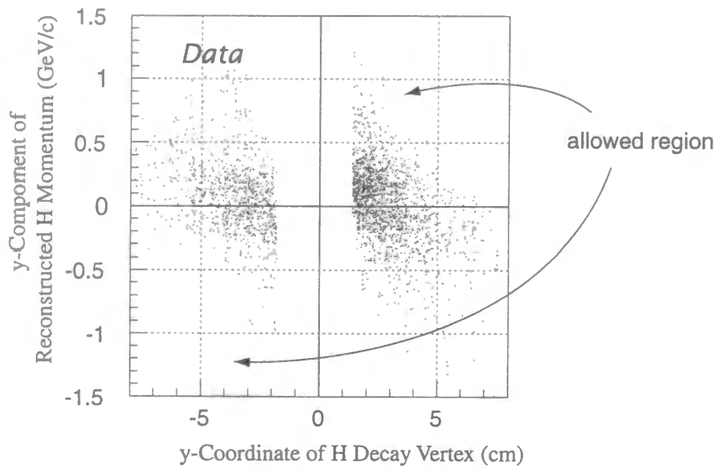

Figure 3.48: Distribution of the y-coordinate of the H decay vertex versus the y-component of the reconstructed H momentum. The H decay vertex was approximated to be at the same position as that of Λ in the analysis. The first and third quadrants are allowed region.

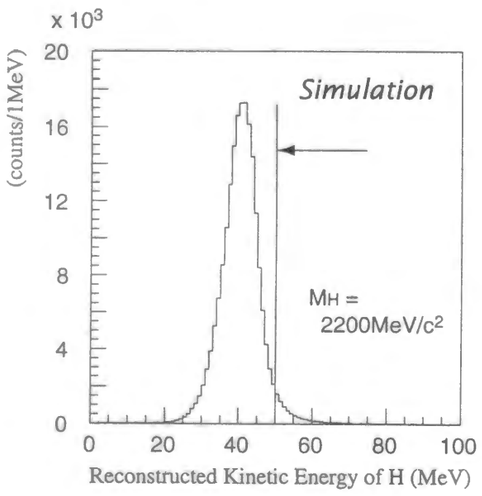

Figure 3.49: Reconstructed kinetic energy spectrum of the H obtained by the Monte Carlo simulation. The solid line and arrow indicate the cut position.

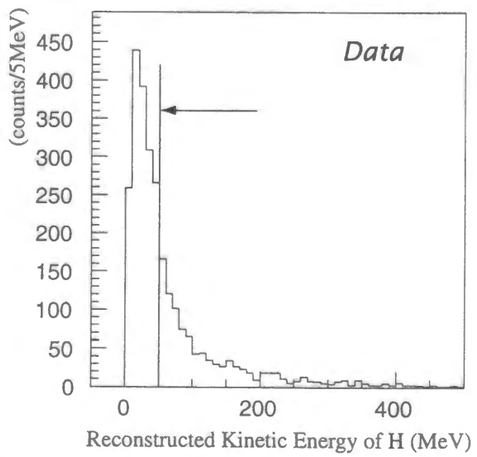

Figure 3.50: Experimental spectrum of the kinetic energy of the reconstructed H. The solid line and arrow indicate the cut position.

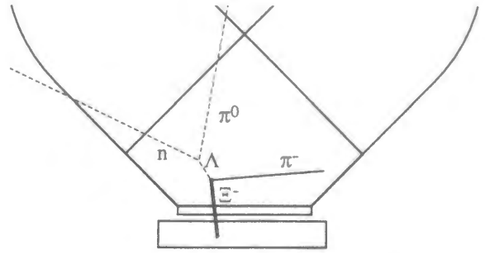

Figure 3.51: Example of background events included in the 'Λ decay' events. When a Ξ^- comes into and decays in the SCIFI block, then the resultant Λ decays into neutrals or decays out of the SCIFI block, the event has the same topology as that of the Λ decay.

8. When the neutron counter arrays had charged hits which were inconsistent with the proton and π^- from the Λ decay observed in the SCIFI detector, and when the charged particles had β larger than 0.5, they were rejected from the H candidates with the same reason described in the cut studies of $H \to \Sigma^- p$ mode (cut #8).

9. The events with Λ of which reconstructed momentum was positive in the z direction were eliminated. Events of this kind are dominated by the Ξ^- decay, while Λ's from the H decay should be isotropic.

10. The 'V' tracks of which opening angle was smaller than 20° or larger than 160° were eliminated due to the low recognizing efficiency in the eye scanning as seen in Figure 3.35.

As a result of the above cuts, the reconstructed H mass spectrum presented in Figure 3.52 was obtained. The dashed curve in Figure 3.52 corresponds to the expected peak shape of the H of which mass is assumed to be 2200 MeV/c^2, in which the same cuts as those of the experimental data were applied.

In the SCIFI image data of the event indicated as 'A', shown in Figure 3.53, one straight track (track 1) was observed as well as a 'V' track. By investigating the spectrometer data of this event, it was found that this track does not correspond to the outgoing K^+. Moreover, when assigning p and π^- to the elements 2 and 3 of the 'V' track, and reconstructing the trajectory of Λ, the distance of the closest approach (DCA) between the reconstructed Λ trajectory and the track 1 was calculated to be 614 μm. Taking the position resolution of 490 μm into account, the Λ and the particle (track 1) were considered to be generated at the same point, and this event is quite likely to show the sequential Ξ^- decay, $\Xi^- \to \Lambda\pi^-$, $\Lambda \to p\pi^-$. Therefore, we rejected this event from the remaining H candidates. It should be noted that the vertex position of Ξ^- decay is outside the SCIFI block, and thus it is not seen in the figure. Although the other events in Figure 3.52 were also extensively investigated in the image data, no evident information to reject them from the H candidates

was obtained. However, they can be resulted from neutrons via the π^- capture on a nucleus and Λ's from the Ξ^- decay or the (K^-, K^+) reaction.

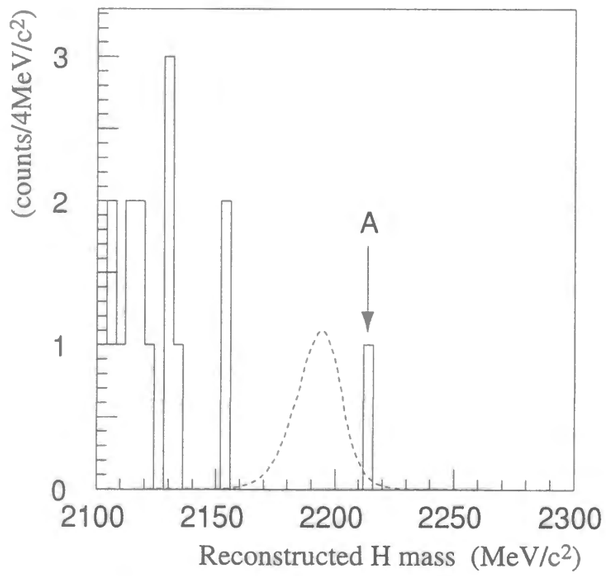

Figure 3.52: Reconstructed H-mass spectrum in the $H \to \Lambda n$ kinematics obtained after the series of cuts. The event 'A' was rejected from the H candidates with the SCIFI image data analysis (see the text). The dashed line shows the expected peak shape with an assumed H mass of 2200 MeV/c^2. The peak size is arbitrary.

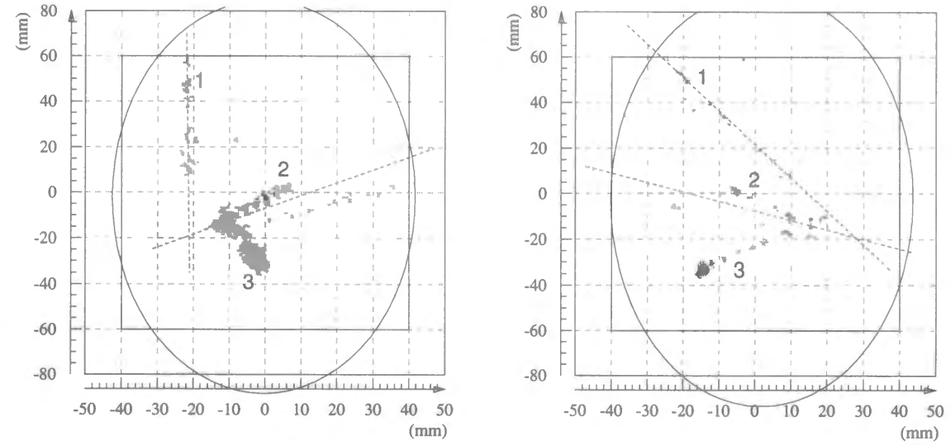

Figure 3.53: SCIFI image data of the event which remained in the signal region of the H. This event was rejected from the H candidates by means of the image analysis (see the text).

Upper limits

Since no clear events positively indicating the $H \to \Lambda n$ decay were observed, we have set upper limits on the value R which was introduced in the previous section. This time R is the product of a branching ratio of the H formation from the $(\Xi^-, {}^{12}\mathrm{C})$ atom and that of the $H \to \Lambda n$ decay:

$$R = Br[(\Xi^-, {}^{12}\mathrm{C})_{atom} \to HX] \cdot Br[H \to \Lambda n] \,, \tag{3.37}$$

where X was assumed to be ${}^{11}\mathrm{B}$(g.s.) in this process, too. Table 3.6 represents the detection sensitivity in the case of the H mass and lifetime of 2200 MeV/c^2 and 0.4 ns, which was obtained from the Monte Carlo simulation. Due to the several tight criteria, the combined sensitivity has become a small value: $0.1 \sim 0.2\%$.

Finally, the upper limits on R was determined with use of Eq. (3.36). An additional cut-off at the reconstructed H mass of 2160 MeV/c^2 (Figure 3.52) was applied in the upper limit calculation. The efficiency of this cut was incorporated in η in Eq. (3.36). Figure 3.54 shows the obtained upper limits on R with 90% C.L. as a function of the H mass in the case of the H lifetime of 0.4 ns. Also Figure 3.55 displays a contour plot of the upper limits on R in the H mass range from 2170 MeV/c^2 to 2230 MeV/c^2 and in the H lifetime range from 0.1 ns to 10 ns. The minimum upper limit of 26% was obtained in the case that the H mass and lifetime are $2200 \sim 2205$ MeV/c^2 and 0.4 ns. This result sets the finite upper limit on the H formation rate in the case that the branching ratio of $H \to \Lambda n$ is larger than 26%.

Criterion	Sensitivity of each cut[a]	Combined sensitivity
Cut #1	100%	100%
Neutron detection with 2 MeVee threshold. (Cut #2 is included.)	6.87%	6.87%
Cut #3	99.9%	6.87%
Λ decays in the fiducial.	34.3%	2.35%
Λ decays into $p + \pi^-$.	63.9%	1.50%
Either p or π^- stops in the fiducial.	49.2%	0.740%
Cut #4	50.4%	0.373%
Cut #5	96.8%	0.361%
Cut #6	95.9%	0.346%
Cut #7	93.8%	0.324%
Cut #8	100%	0.324%
Cut #9	48.4%	0.157%
Cut #10	95.3%	0.150%
Recognition in the eye-scanning	91.3%	0.137%

Table 3.6: Detection sensitivity of $H \to \Lambda n$ events with a series of cuts in the case that the H mass and lifetime are 2200 MeV/c^2 and 0.4 ns respectively.

[a]The definition is the same as that of Table 3.5.

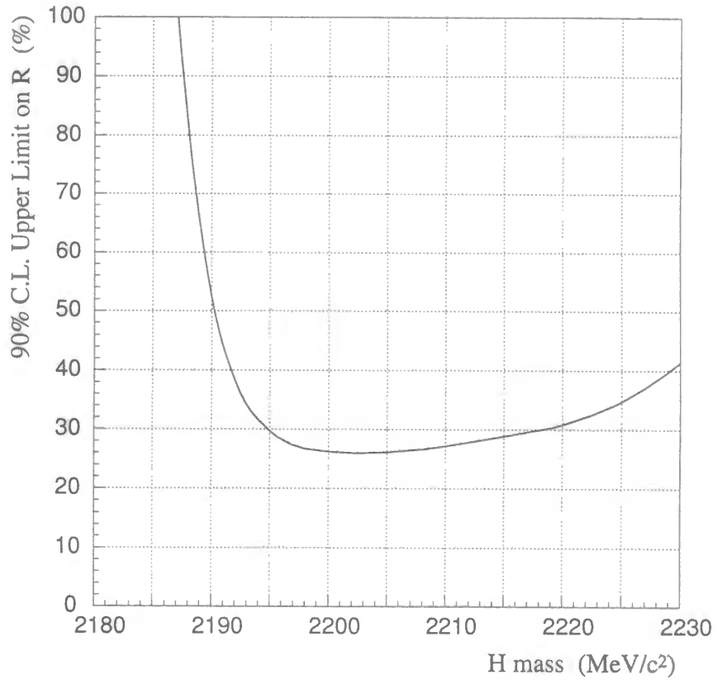

Figure 3.54: 90% C.L. upper limits on the product of the branching ratios, R (= $Br[(\Xi^-, {}^{12}\mathrm{C})_{atom} \to HX] \cdot Br[H \to \Lambda n]$), as a function of the H mass in the case of the H lifetime of 0.4 ns. The residual of the H formation (X) was assumed to be ^{11}B(g.s.).

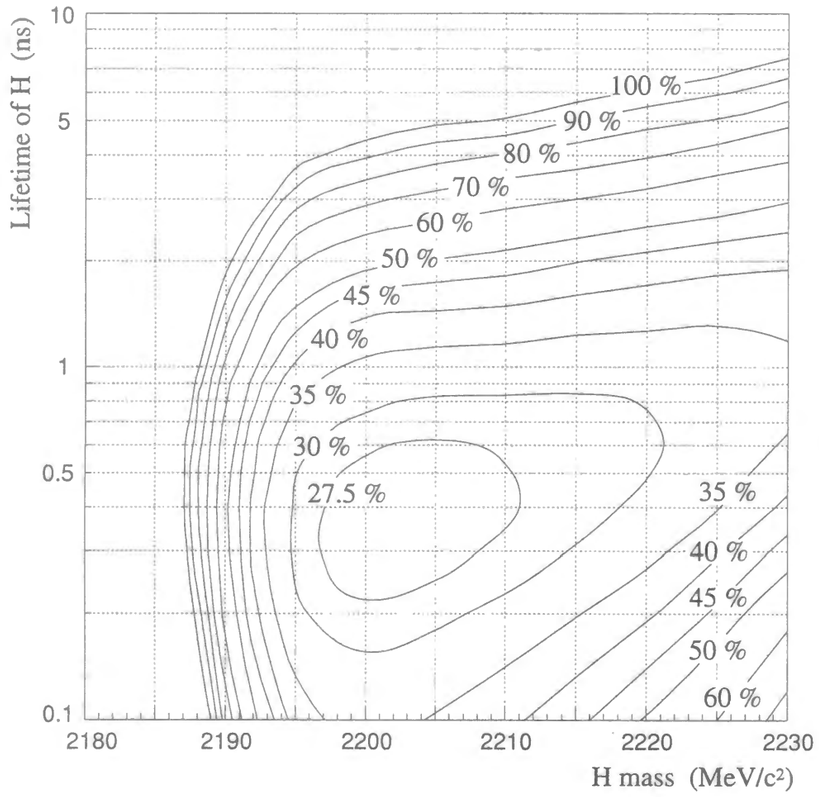

Figure 3.55: Contour plot of 90% C.L. upper limits on the product of the branching ratios, $R\ (= Br[(\Xi^-,\ ^{12}\mathrm{C})_{atom} \to HX] \cdot Br[H \to \Lambda n])$, where X was assumed to be ^{11}B(g.s.).

Chapter 4

Conclusion

The experiment to search for the H-dibaryon and S $= -2$ nuclei via the (K^-, K^+) reaction on ^{12}C was performed at the Brookhaven AGS using a 1.8 GeV/c K^- beam (BNL-E885). A 8 cm wide, 1 cm high, and 5 cm long diamond target was exposed to 8×10^{11} K^-'s in total with the typical intensity of 1.0×10^6 K^- per 1.2 sec-spill. Among the physics subjects, the H-dibaryon search is reported in this thesis, while the studies of S $= -2$ nuclei such as Ξ and double-Λ hypernuclei are described in Refs. [108, 117, 135]. The H-dibaryon was searched for in the direct production process, $K^- + {}^{12}\mathrm{C} \to K^+ + H + X$, and also through the atomic capture of Ξ^- hyperons, $(\Xi^-,\ ^{12}\mathrm{C})_{atom} \to H + X$, where Ξ^-'s are produced in the quasi-free reaction, $K^- + (p) \to K^+ + \Xi^-$.

For both searches, measurement of the (K^-, K^+) reaction was essential and it was achieved by the magnetic spectrometer system comprising the dipole magnet, drift chambers, scintillator hodoscopes, and aerogel Čerenkov counters.

In order to search for the direct H production, a missing-mass spectrum below the end point of the quasi-free Ξ^- production was investigated. If the relatively light H ($M_H \lesssim 2200$ MeV/c^2) exists, a peak separated from that of the quasi-free Ξ^-'s should be seen according to the theoretical calculations. In spite of the enough sensitivity to find the H compared to the theoretically predicted rate, no clear peak was found. Thus a 90% C.L. upper limit on the direct-production cross section of the H-dibaryon in the K^+ forward angles was determined in the range of a few nb/sr to 10 nb/sr for the H masses below 2100 MeV/c^2, while upper limits of about 200 nb/sr were obtained for the H masses around 2200 MeV/c^2. Our result has achieved a large improvement to that of the previous experiment at KEK (KEK-E224) which searched for the H with the same process, $K^- + {}^{12}\mathrm{C} \to K^+ + H + X$. Although another H search was reported in the reaction of $K^- + {}^3\mathrm{He} \to K^+ + H + n$ (BNL-E836), we obtained the lowest upper limit on the direct H production in the deeply bound region in terms of the ratio between the data and theory. And this represents a significant addition to the growing body of evidence refuting the existence of a tightly bound H.

The H formation through the atomic capture of Ξ^- hyperons was also searched for as well as through the direct production process. Selecting events of which missing-mass with $^{12}\mathrm{C}(K^-, K^+)$ kinematics was less than 11.67 GeV/c^2 enabled us to obtain the sample in which the stopped Ξ^- was enhanced. The H was searched for by looking into decay

products from the $(\Xi^-, {}^{12}\mathrm{C})_{atom}$, and the scintillating-fiber (SCIFI) detectors and neutron counter arrays were used for this purpose in addition to the (K^-, K^+) spectrometer. About 40,000 CCD images of the SCIFI detectors were obtained with the above missing-mass cuts, and they were sent to the scanning by human eyes for the event categorization. Firstly, the H-dibaryon was searched for in $H \to \Sigma^- p$ by investigating the events recognized as kinked 'V' in the eye scanning. Secondly, combining the neutron hit information and the image data of Λ decay candidates, the H mass was reconstructed with respect to the decay mode of $H \to \Lambda n$. After a series of cuts, no positive evidence of the H was found in both decay modes. Therefore the 90% C.L. upper limits on the product of the branching ratio of the H formation from the $(\Xi^-, {}^{12}\mathrm{C})_{atom}$ and that of the H decay into $\Sigma^- p$ and Λn (R) were determined for the H lifetimes from 0.1 ns to 10 ns. For the $H \to \Sigma^- p$ mode, the upper limits on R were investigated for the H masses from 2140 MeV/c^2 to 2230 MeV/c^2, and were obtained to be less than 30% for the H lifetimes of $0.2 \sim 2$ ns in the whole H mass range. Especially, the limits are of 10% for the H masses larger than 2220 MeV/c^2 and the H lifetimes of $\sim$1 ns. This value is considerably lower than Aerts and Dover's predicted rates of the H formation from the $(\Xi^-, {}^{4}\mathrm{He})_{atom}$ on the assumption that the branching ratio of $H \to \Sigma^- p$ is 50%. On the other hand, the upper limits on R were determined in the $H \to \Lambda n$ mode for the H mass range from 2180 MeV/c^2 to 2230 MeV/c^2 with the above H lifetimes. The minimum value of 26% was obtained with the H mass and lifetime around 2205 MeV/c^2 and 0.4 ns.

Acknowledgements

Until completion of this thesis work, I have been supported by a number of people with their collaboration, advice, and encouragement. I am so glad to express my thanks to them here. I deeply appreciate efforts and kindness of all who have helped me in the execution of my research at graduate school.

First of all, I would like to express my sincere gratitude to Prof. Ken'ichi Imai, who has been my supervisor. He guided me to an exciting world of the experimental hadronic and nuclear physics, and it made my graduate school days fruitful and enjoyable. He always gave me valuable ideas and suggestions when I had problems in the experiment and data analysis. I have learned from him about not only technical things on experiments but also attitudes to the physical research as a physicist.

I would address my thanks to all the members of BNL-E885 collaboration. I could not complete this thesis work without their great efforts. I thank Prof. Gregg Franklin, who was a spokesperson of E885. His contribution ranged from the total management of the collaboration to the specific analysis, especially writing an upgraded tracking code. Also he spared much time to make discussions with me for the publication. I'm grateful to a cospokesperson of E885, Prof. Morgan May, for his encouragement. His valuable advice and suggestions during the data acquisition and analysis led us to the success of this experiment. I would like to express great thanks to Pavel Khaustov and Michael Landry, who were my coworkers through the experiment. A lot of discussions with them provided me an enjoyable experience of the collaboration, and were of course indispensable to the completion of the data analysis.

I thank Prof. Brian Quinn for his contribution to the data acquisition system, especially building the newly-installed second-level trigger. I'm grateful to Prof. Curtis Meyer for the preparation of the experiment. He coordinated the fabrication and installation of the scintillating-fiber blocks. I am thankful to Prof. Reinhard Schumacher for his advice and also taking care of the drift chamber system. I would like to thank to Dr. Alain Berdoz and Dr. Daniel Carman. Without their tireless efforts for setting up and running the experiment, we could not achieve the success of the experiment. I also would like to address my thanks to Dr. Richard Magahiz, Al Biglan, Phil Koran, Rod McCrady, and Kent Paschke for keeping the experiment running. I thank Gary Wilkin for his engineering support, and Ms. Kim Minihan for her secretarial support.

I would express my gratitude to Prof. Robert Chrien at BNL. His efforts to run the experiment smoothly are exceedingly appreciated. Also my great experiences of my stay

at BNL were largely owing to his kind support. I thank Prof. Phil Pile and the AGS staffs for keeping the AGS running without significant problems during our data acquisition. I appreciate the contribution of Dr. Dave Alburger by fabricating a nice diamond target. I would thank to Dr. Reyad Sawafta and Dr. Adam Rusek for their tremendous help during my stay at BNL for the experiment. The BNL technicians, Richard Sutter, Ed Meier, Al Minn, and Rick Wall need to be thanked for their engineering supports. I'm also thankful to Ms. Cora Feliciano, who is a secretary of the medium-energy physics group at BNL.

I wish to thank to Prof. Bernd Bassalleck, Prof. Jürgen Franz, Prof. Fujio Takeutchi, and Dr. Toru Iijima for their large contribution. Prof. Bassalleck made important neutron-detector simulation for us, and also frequently gave us valuable comments and advice. Prof. Franz set up the large drift chambers in the backward region of the spectrometer (BD1,2). Prof. Takeutchi spent his time to help me at BNL, and also he was willing to allow me to use the computer at Kyoto Sangyo University, which quite shortened time for the data reduction. The significant upgrade of aerogel Čerenkov counters (IC and FC) was accomplished with enormous help by Dr. Iijima. His fantastic aerogel with high transparency has improved K/π separation very much. Also he told me a lot of practical things for living in Long Island as well as academic matters. I thank to Mr. Masaru Yosoi, Atsuko Ichikawa and Yasuhiro Kondo for kindly coming to BNL to help me all the way from Kyoto in either or both of the E885 test experiment and/or the production run. I thank to Dr. Thomas Bürger, Dr. Val Zeps, Dr. Charles Davis, Dr. Liping Gan, Dr. Larry Lee, Dr. Shelley Page, Dr. Des Ramsay, Dr. Reinhard Stotzer, and many others for keeping the experiment running. Dr. Stotzer helped us a part of the analysis. Their contribution to the collaboration was indispensable to the success of E885.

I wish to acknowledge the help and encouragement by Prof. Akira Masaike, Prof. Harutaka Sakaguchi, Prof. Hideto En'yo, Dr. Masanobu Nakamura, Dr. Kiyohiko Takimoto, Dr. Tetsuya Murakami, Dr. Haruhiko Funahashi, and all the other members and alumni of NH group and previous NE/PN group in Kyoto University, where I have learned the experimental nuclear and hadronic physics in my graduate school days. Especially, my thanks are due to Dr. Yoshitaka Itow, who taught me the SCIFI-IIT detector system in both views of the hardware electronics and the software issue. When I had problems in setting up the system at the test experiment, he had the kindness to come to BNL in order to solve the problems.

I would like to express my thanks to Prof. Tomokazu Fukuda, Prof. Tomofumi Nagae, Dr. Masaharu Ieiri, Prof. Kazuma Nakazawa, Prof. Shigeki Aoki, Prof. Takuo Yoshida, and Prof. Hideki Hamagaki for willingness to share their unique experience and knowledge in the KEK and BNL experiments. Also, I thank to Prof. Toru Okusawa for giving me a opportunity to start a new physics for me.

In the aspects of theoretical calculation, I thank to Prof. Toshio Motoba for precise calculations on the Ξ hypernuclear production. I appreciate his kindness to comply with our request in spite of his busyness. I am grateful to Prof. John Millener for discussions about the direct double-Λ hypernuclear production. Thanks are also delivered to Prof. Takashi Nakano, who made the analysis of the direct H production on emulsion in the previous KEK experiment (E176). The email discussion on the theoretical calculation of the cross

section for the direct H production was quite helpful for me.

I thank all the part-time workers who scanned the SCIFI image data. Thanks to their efforts, the image data analysis proceeded very efficiently.

I am thankful to Ms. Yuka Sasaki-Nakakoji, Ms. Terue Ishino-Kiyosawa, and Ms. Mari Sawada-Hayashi for their secretarial support and warm hospitality. I would like to thank to Ms. Keiko Nakagawa for her clerical work. Thanks to their tremendous supports, I was able to concentrate on the physics research. I'm also grateful to Mrs. Nobue Imai for her hospitality. She has largely contributed to improve our activity by supporting Prof. Ken'ichi Imai. Her delicious dishes and pleasant atmosphere encouraged us much. Also during my stay at BNL, she and Prof. Imai sometimes invited me to dinner when they visited there. It released my strain and stress caused by the long beam time.

Finally, I would address my heartfelt thanks to my father, mother, and brother. I could not complete this thesis without their continuous patience, encouragement, and support.

Appendix A

Color-magnetic interaction and the H-dibaryon

The Hamiltonian of the color-magnetic interaction between quarks due to one gluon exchange is given by

$$H_m = -\alpha_s \sum_{i>j}^{N} \sum_{a=1}^{8} (\vec{\sigma}_i \lambda_i^a) \cdot (\vec{\sigma}_j \lambda_j^a) M(m_i, m_j)\,, \tag{A.1}$$

where α_s is the strong coupling constant; N is the total number of quarks; a labels colors and i (j) labels quarks. $\vec{\sigma}_i$ and λ_i^a are the spin and color vectors for the i-th quarks. If i or j indicates an antiquark, the following replacement should be made:

$$\sigma_i \to -\sigma_i^*\,, \qquad \lambda_i \to -\lambda_i^*\,. \tag{A.2}$$

However, at present we consider the system containing only quarks (u, d, and s). M is the magnetic-interaction strength which is a function of quark masses. For simplicity, we use an average strength $\overline{M}$ instead of M. This approximation is justified by the roughly good establishment of SU(3) flavor symmetry. Then $\overline{M}$ can be removed from the summation.

The products of $\sigma^k \lambda^a$ are among the generators of color-spin SU(6) (SU(6)$_{cs}$). The whole components of SU(6)$_{cs}$ generators are defined to be

$$\alpha^\mu = \begin{cases} \sqrt{\frac{2}{3}}\sigma^k, & k = 1,2,3 \\ \lambda^a, & a = 1,2,\cdots,8 \\ \sigma^k \lambda^a\,. \end{cases} \tag{A.3}$$

The thirty-five α's generate an SU(6)$_{cs}$. They are normalized to

$$\mathrm{Tr}\ (\alpha)^2 = 4\,, \quad \mathrm{Tr}\ (\lambda)^2 = 2\,, \quad \mathrm{Tr}\ (\sigma)^2 = 2\,, \tag{A.4}$$

as is conventional. In order to extract $(\vec{\sigma}_i \lambda_i^a) \cdot (\vec{\sigma}_j \lambda_j^a)$, we consider the product $\alpha_i^\mu \alpha_j^\mu$. This can be unfolded as follows:

$$\sum_{\mu=1}^{35} \alpha_i^\mu \alpha_j^\mu = \sum_{\mu=1}^{3} \alpha_i^\mu \alpha_j^\mu + \sum_{\mu=4}^{11} \alpha_i^\mu \alpha_j^\mu + \sum_{\mu=12}^{35} \alpha_i^\mu \alpha_j^\mu$$

$$= \frac{2}{3} \sum_{k=1}^{3} \sigma_i^k \sigma_j^k + \sum_{a=1}^{8} \lambda_i^a \lambda_j^a + \sum_{k=1}^{3} \sum_{a=1}^{8} (\sigma_i^k \lambda_i^a)(\sigma_j^k \lambda_j^a)\,. \tag{A.5}$$

Therefore,

$$\sum_{i>j}^{N} \sum_{a=1}^{8} (\vec{\sigma}_i \lambda_i^a) \cdot (\vec{\sigma}_j \lambda_j^a) = \sum_{i>j}^{N} \sum_{\mu=1}^{35} \alpha_i^\mu \alpha_j^\mu - \sum_{i>j}^{N} \sum_{a=1}^{8} \lambda_i^a \lambda_j^a - \frac{2}{3} \sum_{i>j}^{N} \vec{\sigma}_i \cdot \vec{\sigma}_j\,. \tag{A.6}$$

Denoting the mass eigenstate by $|\mathcal{M}\rangle$, the eigenvalue of each component of the right side of Eq. (A.6) is calculated as follows:

$$\begin{aligned} \langle \mathcal{M} | \sum_{i>j}^{N} \sum_{\mu=1}^{35} \alpha_i^\mu \alpha_j^\mu | \mathcal{M} \rangle &= \frac{1}{2} \sum_{\mu=1}^{35} \left\{ (\alpha_1^\mu + \alpha_2^\mu + \cdots + \alpha_N^\mu)^2 - \sum_{i=1}^{N} (\alpha_i^\mu)^2 \right\} \\ &= \frac{1}{2} C_6 - \frac{35}{3} N\,, \end{aligned} \tag{A.7}$$

$$\begin{aligned} \langle \mathcal{M} | \sum_{i>j}^{N} \sum_{a=1}^{8} \lambda_i^a \lambda_j^a | \mathcal{M} \rangle &= \frac{1}{2} \sum_{a=1}^{8} \left\{ (\lambda_1^a + \lambda_2^a + \cdots + \lambda_N^a)^2 - \sum_{i=1}^{N} (\lambda_i^a)^2 \right\} \\ &= \frac{1}{2} C_3 - \frac{8}{3} N\,, \end{aligned} \tag{A.8}$$

$$\begin{aligned} \langle \mathcal{M} | \sum_{i>j}^{N} \vec{\sigma}_i \cdot \vec{\sigma}_j | \mathcal{M} \rangle &= \frac{1}{2} \left\{ (\vec{\sigma}_1 + \vec{\sigma}_2 + \cdots + \vec{\sigma}_N)^2 - \sum_{i=1}^{N} (\vec{\sigma}_i)^2 \right\} \\ &= 2J(J+1) - \frac{3}{2} N\,, \end{aligned} \tag{A.9}$$

where C_6 and C_3 are defined by eigenvalues of the following quadratic Casimir operators of SU(6) and SU(3):

$$\mathcal{F}_6 = \sum_{\mu=1}^{35} \left(\sum_{i=1}^{N} \alpha_i^\mu \right)^2\,, \tag{A.10}$$

$$\mathcal{F}_3 = \sum_{a=1}^{8} \left(\sum_{i=1}^{N} \lambda_i^a \right)^2\,, \tag{A.11}$$

and the total spin was denoted as J:

$$4\boldsymbol{J}^2 = \left(\sum_{i=1}^{N} \vec{\sigma}_i \right)^2\,. \tag{A.12}$$

Also, generally defining the generators of SU(N) as X^ν, the following relation was useful:

$$\sum_{\nu=1}^{N^2-1} (X^\nu)^2 = \frac{N^2-1}{N} \mathrm{Tr}\ (X)^2\,. \tag{A.13}$$

Inserting Eqs. (A.7), (A.8), and (A.9) into Eq. (A.6), the eigenvalue of the color-magnetic Hamiltonian (A.1) is expressed as

$$E_m = \alpha_s \left\{ 8N - \frac{1}{2}C_6 + \frac{1}{2}C_3 + \frac{4}{3}J(J+1) \right\} \overline{M} \,. \tag{A.14}$$

Here we consider the six-quark dibaryon state, $N = 6$. Since the physical state is in a color singlet, we find $C_3 = 0$. The eigenvalues of C_6 are listed in Table A.1 for the S-wave dibaryon case. C_6 takes the largest value 144 in the $SU(6)_{cs}$ representation of **490** and SU(3) flavor singlet ($uuddss$) with $J = 0$. This quantum state corresponds to the H-dibaryon, and the color-magnetic interaction provides the largest energy reduction, $-24\alpha_s\overline{M}$, among the six-quark states.

Table A.1: Quantum numbers of S-wave dibaryons.

$SU(6)_{cs}$ representation	C_6	J	$SU(3)_f$ representation
490	144	0	1
896	120	1, 2	8
280	96	1	10
175	96	1	10*
189	80	0, 2	27
35	48	1	35
1	0	0	28

Appendix B

Microstrip gas chambers

For the particle tracking, three sets of microstrip gas chambers (MSGCs) were placed in the spectrometer system in addition to the drift chambers. One of them (IM1) was positioned upstream of the target, while the others (FM1 and FM2) downstream of the target. Unlike wire chambers, MSGCs utilize microstrip prints for the position measurement. In our experiment, two different types of microstrip prints were used. One was manufactured with integrated-circuit (IC) photolithographic technology, and the other with printed-circuit (PC) photolithographic technology. An IC print consisted of a 0.3 μm thick gold layer deposited on a 125 μm thick Upilex[1] film. The gold layer was etched to the pattern of 20 μm wide anodes interleaved with 280 μm wide cathodes. The strip pitch was 500 μm. On the other hand, a 5 μm thick copper layer deposited on a 50 μm thick Kapton[2] film made a PC print. The printed pattern was the same as that of the IC print except for 50 μm wide anodes. Cross sections of the two different prints are shown in Figure B.1. For both x

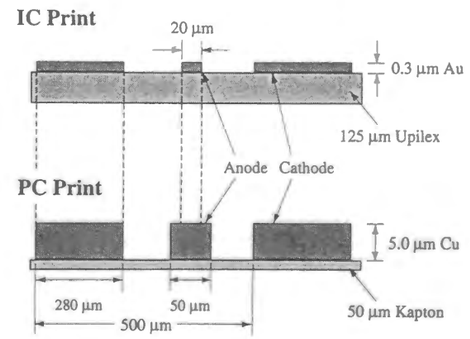

Figure B.1: Schematic view of the two types of microstrip prints (IC and PC). The drawing is not to scale.

[1]Upilex polyimide film is manufactured by UBE Industries, Japan.
[2]Kapton polyimide film is manufactured by DuPont, Wilmington DE, U.S.A.

and y measurements, two sheets of the microstrip prints were mounted orthogonally in the MSGC unit together with the cathode drift planes (50 μm thick aluminized mylar) and the readout electronics in the gas enclosure. Figure B.2 shows a cross-sectional top view of the MSGC. IM1 had PC and IC prints for x and y measurements respectively, while FM1 and FM2 contained only IC prints. The dimension of an active area was 80×50 mm^2, and the gap between the cathode drift plane and the microstrip print was 5 mm. The gas mixture flowing in the chambers was argon / dimethyl ether (DME) with the ratio of 4 : 1. The more details can be found in Ref. [123].

Although the MSGCs were introduced in order to improve the vertex resolution, we couldn't obtain enough efficiency (~80% for each print) due to sparking on the print and the noise problem. Therefore, data of the MSGCs were not used in the analysis described in this report in order not to reduce the statistics. The analysis which included the MSGC data was reported in Ref. [118].

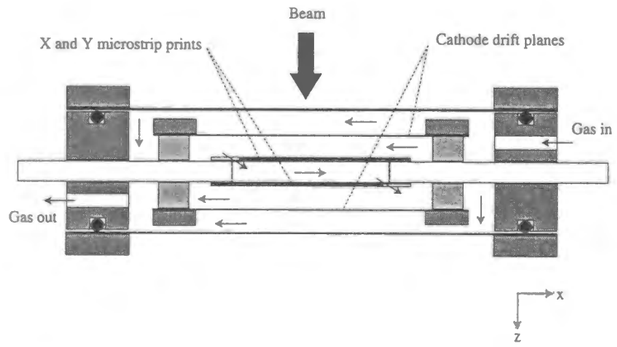

Figure B.2: Cross-sectional top view of MSGC. The thin arrows denote gas flow.

Appendix C

Calibration of the 60 Hz cycle noise

It is important for detectors which obtain pulse height information to reject AC noise coming from power lines. Generally, the AC noise can be removed by inserting a high-pass filter in a signal cable. Under the quite high signal rates, however, electric charges are piled up in a capacity in the filter and the signal gain will decrease. In our case of the beam intensity of ~10^6/sec, we could not use the filters for the in-beam detectors due to the above reasons. Especially, this was crucial for the aerogel Čerenkov counters IC and FC because the ADC pedestals fluctuate due to the AC noise (60 Hz) and thus tight cuts on the pulse height were not available.

Therefore, as one of the solutions, we sent discriminated signals of a 10 kHz pulser to a CAMAC scaler which was reset every 16.67 ms (60 Hz) and the scaler value was recorded

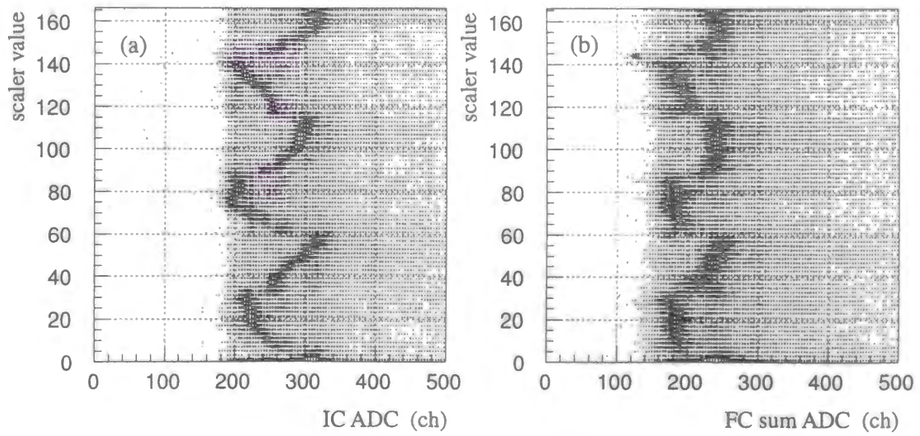

Figure C.1: ADC pedestal fluctuation depending on 60Hz phase of the AC noise for the aerogel Čerenkov counters IC(a) and FC(b). Signals from FC were analog-summed over its four PMT channels. The scaler value corresponds to time interval from the reset time with a unit of 0.1 ms.

in every events. The scaler value corresponds to time interval from the reset time with a unit of 0.1 ms. By this procedure, the phase in 60 Hz of each event could be known and it was possible to calibrate the AC noise in the offline analysis. Figure C.1 shows the ADC pedestal fluctuation of IC and FC depending on 60 Hz phase of the AC noise. The calibration was performed by aligning the pedestal peak of each phase at the same location. Figure C.2 shows the pedestal distribution of IC before the correction(a) and after the correction(b) respectively. Similarly, Figure C.3 shows the pedestal distribution of FC before the correction(a) and after the correction(b) respectively.

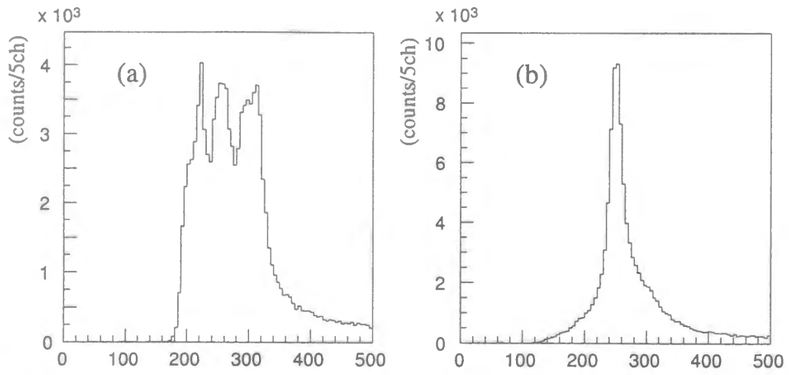

Figure C.2: Pedestal distribution of IC before the 60hz AC noise correction(a) and after the correction(b) respectively.

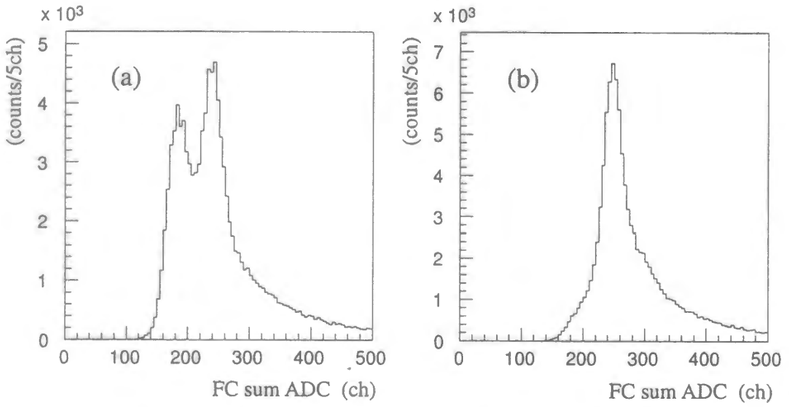

Figure C.3: Pedestal distribution of FC before the 60hz AC noise correction(a) and after the correction(b) respectively.

Appendix D

Normalization of cross section for the direct H production

The formula for normalizing the cross section on the direct H production is shortly described here. More details can be found in Ref. [108]. The number of detected events per unit missing mass is expressed to be

$$\frac{dN}{dE} = \lambda \int dt I(t)\epsilon(t)\beta(t) \int d\Omega \alpha(E,\Omega) \frac{d^2\sigma}{d\Omega dE}, \tag{D.1}$$

where λ is number-density along the beam direction, $\alpha(E,\Omega)$ is the acceptance as a function of the missing mass and the outgoing particle angle, which is reaction-dependent. Also, $\epsilon(t)$, $\beta(t)$, $I(t)$ refer to the data acquisition live time, the overall event reconstruction efficiency for a particular set of cuts, and the beam rate respectively. The first integral can be written as

$$\int dt I(t)\epsilon(t)\beta(t) = B \langle \beta \rangle , \tag{D.2}$$

where

$$B = \int dt I(t)\epsilon(t) \tag{D.3}$$

is the integrated flux $\times$ live time, which can be considered as "effective beam", and

$$\langle \beta \rangle = \frac{\int dt I(t)\epsilon(t)\beta(t)}{\int I(t)\epsilon(t)} \tag{D.4}$$

is the beam-weighted average event reconstruction efficiency. The second integral in Eq. (D.1) can be expressed as follows:

$$\int d\Omega \alpha(E,\Omega) \frac{d^2\sigma}{d\Omega dE} = \alpha(E) \cdot \left\langle \frac{d^2\sigma}{d\Omega dE} \right\rangle \cdot \Delta\Omega, \tag{D.5}$$

where

$$\alpha(E) = \frac{\int d\Omega \alpha(E,\Omega) \frac{d^2\sigma}{d\Omega dE}}{\int d\Omega \frac{d^2\sigma}{d\Omega dE}} \tag{D.6}$$

is the angle-averaged acceptance and

$$\left\langle \frac{d^2\sigma}{d\Omega dE} \right\rangle = \frac{\int d\Omega \frac{d^2\sigma}{d\Omega dE}}{\Delta\Omega} \tag{D.7}$$

is the angle-averaged double-differential cross section. Then, from Eqs. (D.1), (D.2), and (D.5) we obtain

$$\frac{dN}{dE} = \lambda B \langle\beta\rangle \alpha(E) \left\langle \frac{d^2\sigma}{d\Omega dE} \right\rangle \Delta\Omega. \tag{D.8}$$

Integration over E provides

$$N = \lambda B \langle\beta\rangle \alpha \left\langle \frac{d\sigma}{d\Omega} \right\rangle \Delta\Omega \tag{D.9}$$

where

$$\alpha = \frac{\int dE d\Omega \alpha(E,\Omega) \frac{d^2\sigma}{d\Omega dE}}{d\Omega dE \frac{d^2\sigma}{d\Omega dE}} \tag{D.10}$$

refers to the angle- and energy-averaged acceptance, and

$$\left\langle \frac{d\sigma}{d\Omega} \right\rangle = \frac{\int d\Omega dE \frac{d^2\sigma}{d\Omega dE}}{\Delta\Omega} \tag{D.11}$$

stands for the angle-averaged differential cross section.

Using Eq. (D.9), the relation between cross sections of two different processes (labeled by 1 and 2) which have the same solid angle for the outgoing particle is written as

$$\left\langle \frac{d\sigma}{d\Omega} \right\rangle_2 = \frac{N_2}{N_1} \cdot \frac{\lambda_1 B_1 \langle\beta\rangle_1 \alpha_1}{\lambda_2 B_2 \langle\beta\rangle_2 \alpha_2} \cdot \left\langle \frac{d\sigma}{d\Omega} \right\rangle_1. \tag{D.12}$$

By adopting Eq. (D.12) to the (quasi-)free Ξ^- production on hydrogen and carbon nuclei in a CH_2 target, we obtain

$$\left\langle \frac{d\sigma}{d\Omega} \right\rangle_\Xi^{^{12}\mathrm{C}} = \frac{N_{\mathrm{CH_2}}^{^{12}\mathrm{C}}}{N_{\mathrm{CH_2}}^{^{1}\mathrm{H}}} \cdot \frac{\lambda_{\mathrm{CH_2}}^{^{1}\mathrm{H}} B_{\mathrm{CH_2}} \langle\beta\rangle_{\mathrm{CH_2}} \alpha^{^{1}\mathrm{H}}}{\lambda_{\mathrm{CH_2}}^{^{12}\mathrm{C}} B_{\mathrm{CH_2}} \langle\beta\rangle_{\mathrm{CH_2}} \alpha^{^{12}\mathrm{C}}} \cdot \left\langle \frac{d\sigma}{d\Omega} \right\rangle_\Xi^{^{1}\mathrm{H}}. \tag{D.13}$$

By adopting Eq. (D.9) to the quasi-free Ξ^- production on carbon nuclei in a diamond target, we obtain

$$N_{diam}^{^{12}\mathrm{C}} = \lambda_{diam}^{^{12}\mathrm{C}} B_{diam} \langle\beta\rangle_{diam} \alpha^{^{12}\mathrm{C}} \left\langle \frac{d\sigma}{d\Omega} \right\rangle_\Xi^{^{12}\mathrm{C}} \Delta\Omega. \tag{D.14}$$

Also the relation of Eq. (D.8) for the H production is written as

$$\left(\frac{dN}{dE} \right)_{diam}^{^{12}\mathrm{C}} = \lambda_{diam}^{^{12}\mathrm{C}} B_{diam} \langle\beta\rangle_{diam} \alpha^{^{12}\mathrm{C}}(E) \left\langle \frac{d^2\sigma}{d\Omega dE} \right\rangle_H^{^{12}\mathrm{C}} \Delta\Omega. \tag{D.15}$$

From Eqs. (D.13), (D.14), and (D.15), we obtain

$$\begin{aligned} \left\langle \frac{d^2\sigma}{d\Omega dE} \right\rangle_H^{^{12}\mathrm{C}} &= \left(\frac{dN}{dE} \right)_{diam}^{^{12}\mathrm{C}} \frac{\alpha^{^{1}\mathrm{H}}}{\alpha^{^{12}\mathrm{C}}(E)} \frac{\lambda_{\mathrm{CH_2}}^{^{1}\mathrm{H}}}{\lambda_{\mathrm{CH_2}}^{^{12}\mathrm{C}}} \frac{N_{\mathrm{CH_2}}^{^{12}\mathrm{C}}}{N_{diam}^{^{12}\mathrm{C}} N_{\mathrm{CH_2}}^{^{1}\mathrm{H}}} \left\langle \frac{d\sigma}{d\Omega} \right\rangle^{^{1}\mathrm{H}} \\ &= \frac{Q}{\alpha^{^{12}\mathrm{C}}(E)} \left(\frac{dN}{dE} \right)_{diam}^{^{12}\mathrm{C}}, \end{aligned} \tag{D.16}$$

where

$$Q = \alpha^{^{1}\mathrm{H}} \cdot \frac{\lambda_{\mathrm{CH_2}}^{^{1}\mathrm{H}}}{\lambda_{\mathrm{CH_2}}^{^{12}\mathrm{C}}} \frac{N_{\mathrm{CH_2}}^{^{12}\mathrm{C}}}{N_{diam}^{^{12}\mathrm{C}} N_{\mathrm{CH_2}}^{^{1}\mathrm{H}}} \left\langle \frac{d\sigma}{d\Omega} \right\rangle^{^{1}\mathrm{H}}. \tag{D.17}$$

Integrating Eq. (D.16) over E in the expected peak region of the H production, which is dependent of the H mass, with the use of the definitions in Eqs. (D.10) and (D.11),

$$\begin{aligned} \left\langle \frac{d\sigma}{d\Omega} \right\rangle_H^{^{12}\mathrm{C}} &= \frac{Q}{\alpha^{^{12}\mathrm{C}}} \cdot \left[N_{diam}^{^{12}\mathrm{C}} \right] \\ &= A \cdot \left[N_{diam}^{^{12}\mathrm{C}} \right], \end{aligned} \tag{D.18}$$

where

$$A = \frac{\alpha^{^{1}\mathrm{H}}}{\alpha^{^{12}\mathrm{C}}} \frac{\lambda_{\mathrm{CH_2}}^{^{1}\mathrm{H}}}{\lambda_{\mathrm{CH_2}}^{^{12}\mathrm{C}}} \frac{N_{\mathrm{CH_2}}^{^{12}\mathrm{C}}}{N_{diam}^{^{12}\mathrm{C}} N_{\mathrm{CH_2}}^{^{1}\mathrm{H}}} \left\langle \frac{d\sigma}{d\Omega} \right\rangle^{^{1}\mathrm{H}} \tag{D.19}$$

is the H-mass-dependent normalization factor and $\left[N_{diam}^{^{12}\mathrm{C}} \right]$ is the number of observed events within the expected peak range in the missing mass spectrum. When calculating an upper limit of the cross section, $\left[N_{diam}^{^{12}\mathrm{C}} \right]$ is replaced to the upper limit of the Poisson statistics with a certain confidence level.

The explicit values in Eq. (D.19) were obtained from the calibration data using the 13 cm long CH_2 target as well as the production data with the diamond target. Figure D.1 shows the missing mass spectrum of the calibration CH_2 data for $p(K^-, K^+)$ kinematics. First, the target thickness λ is tabulated in Table D.1. It was found that total numbers of reconstructed events of Ξ^- production on hydrogen and carbon in the CH_2 target are $N_{\mathrm{CH_2}}^{^{1}\mathrm{H}} = 480$ and $N_{\mathrm{CH_2}}^{^{12}\mathrm{C}} = 424$ respectively by fitting the missing mass spectrum in Figure D.1 with a template of the spectrum from the diamond target data plus a Gaussian peak.

target	thickness λ (cm^{-2})		thickness (cm)	density ($\mathrm{g/cm^3}$)
	hydrogen	carbon		
diamond	$\sim 7.6 \times 10^{21}$ [1]	8.27×10^{23}	5	3.3
CH_2	10.5×10^{23}	5.25×10^{23}	13	0.94

Table D.1: Thickness of the diamond and CH_2 targets.

[1] From epoxy glue in the target.

Also the ratio of total numbers of reconstructed events of Ξ^- production on carbon for the diamond and CH_2 targets was found to be

$$\frac{N^{^{12}C}_{diam}}{N^{^{12}C}_{CH_2}} = 125.6 \pm 6.3 \, . \tag{D.20}$$

The angle- and energy-averaged acceptance for free Ξ^- production on hydrogen, $\alpha^{^1H}$, and that for H production on carbon, $\alpha^{^{12}C}$, were estimated from the Monte Carlo simulation described in Section 3.11. In the simulation, the K^+ angular distribution of Ξ^- production on a free proton was assumed to be isotropic in the center-of-mass system. Although the reaction $p(K^-, K^+)\Xi^-$ has a backward-peaking angular distribution in the center-of-mass system [138], it can be regarded to be flat in the limited forward-angle region of our acceptance. As for the H production on carbon, the K^+ angular distribution was assumed to be isotropic in the center-of-mass system of the incident K^- and two protons in the carbon nucleus. Then the normalization factor A in Eq. (D.18) is calculated as shown in Figure D.2 using the recent measurement of 35 ± 4 μb/sr [121] was used for $\langle d\sigma/d\Omega \rangle^{^1H}$. The statistical error of 7% was estimated due to the limited amount of calibration data, while the systematic error of 11% was obtained from the uncertainty of the elementary cross section of Ξ^- production on hydrogen.

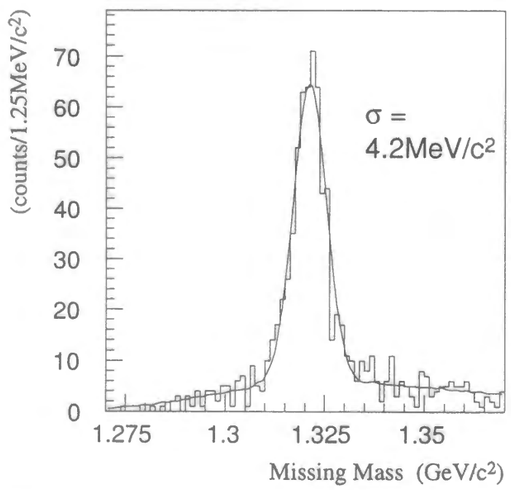

Figure D.1: Missing mass spectrum of the calibration data using the 13 cm long CH_2 target for $p(K^-, K^+)$ kinematics. The solid line represents the fitting curve with the template of the spectrum from the diamond target plus a Gaussian peak.

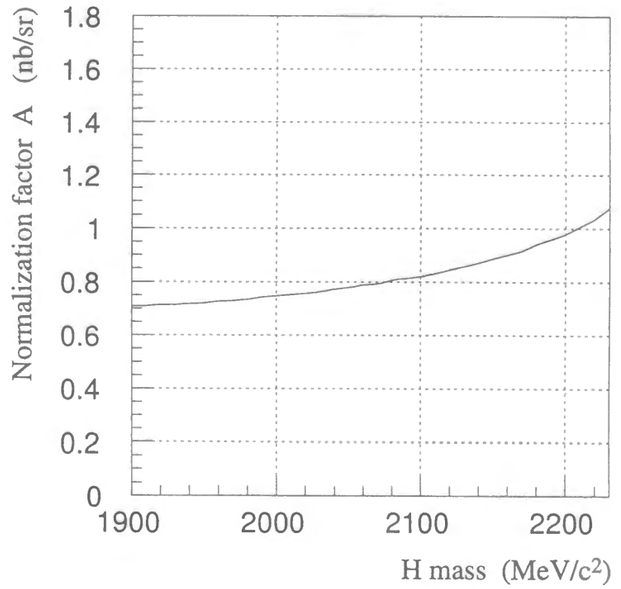

Figure D.2: Normalization factor to convert the number of observed events to cross section as a function of the H mass.

List of Figures

List of Tables

Bibliography

[1] R.L. Jaffe, Phys. Rev. Lett. **38**, 195 (1977); **38**, 1617(E) (1977).

[2] A.T.M. Aerts, P.J.G. Mulders, and J.J. de Swart, Phys. Rev. D **17**, 260 (1978).

[3] P.J. Mulders, A.T.M. Aerts, and J.J. de Swart, Phys. Rev. D **21**, 2653 (1980).

[4] K.F. Liu and C.W. Wong, Phys. Lett. B **113**, 1 (1982).

[5] P.J. Mulders and A.W. Thomas, J. Phys. G **9**, 1159 (1983).

[6] K. Saito, Prog. Theor. Phys. **72**, 674 (1984).

[7] A.T.M. Aerts and J. Rafelski, Phys. Lett. B **148**, 337 (1984).

[8] B.O. Kerbikov, Yad. Fiz. **39**, 816 (1984); Sov. J. Nucl. Phys. **39**, 516 (1984).

[9] L.A. Kondratyuk, M.I. Krivoruchenko, and M.G. Shchepkin, Yad. Fiz. **45**, 514 (1987); Sov. J. Nucl. Phys. **45**, 323 (1987).

[10] K. Maltman, Phys. Lett. B **291**, 371 (1992).

[11] E. Golowich and T. Sotirelis, Phys. Rev. D **46**, 354 (1992).

[12] A.P. Balachandran, A. Barducci, F. Lizzi, V.G.J. Rodgers, and A. Stern, Phys. Rev. Lett. **52**, 887 (1984).

[13] A.P. Balachandran, F. Lizzi, V.G.J. Rodgers, and A. Stern, Nucl. Phys. **B256**, 525 (1985).

[14] S.A. Yost and C.R. Nappi, Phys. Rev. D **32**, 816 (1985).

[15] R.L. Jaffe and C.L. Korpa, Nucl. Phys. **B258**, 468 (1985).

[16] D.I. Diakonov, V.Y. Petrov, P.V. Pobylitsa, and M. Praszałowicz, Phys. Rev. D **39**, 3509 (1989).

[17] H.K. Lee and J.H. Kim, Mod. Phys. Lett. A **5**, 887 (1990).

[18] V.B. Kopeliovich, B. Schwesinger, and B.E. Stern, Nucl. Phys. **A549**, 485 (1992).

[19] I.R. Klebanov and K.M. Westerberg, Phys. Rev. D **53**, 2804 (1996).

[20] J. Kunz and P.J. Mulders, Phys. Lett. B **215**, 449 (1988).

[21] F.G. Scholtz, B. Schwesinger, and H.B. Geyer, Nucl. Phys. **A561**, 542 (1993).

[22] G.L. Thomas, N.N. Scoccola, and A. Wirzba, Nucl. Phys. **A575**, 623 (1994).

[23] M. Oka, K. Shimizu, and K. Yazaki, Phys. Lett. B **130**, 365 (1983); Nucl. Phys. **A464**, 700 (1987).

[24] B. Silvestre-Brac, J. Carbonell, and C. Gignoux, Phys. Rev. D **36**, 2083 (1987).

[25] S. Fleck, C. Gignoux, J.M. Richard, and B. Silvestre-Brac, Phys. Lett. B **220**, 616 (1989).

[26] M. Oka and S. Takeuchi, Nucl. Phys. **A524**, 649 (1991).

[27] U. Straub, Z. Zhang, K. Bräuer, A. Faessler, and S.B. Khadkikar. Phys. Lett. B **200**, 241 (1988).

[28] U. Straub, Z. Zhang, K. Bräuer, A. Faessler, S.B. Khadkikar, and G. Lübeck, Nucl. Phys. **A508**, 385c (1990).

[29] Y. Koike, K. Shimuzu, and K. Yazaki, Nucl. Phys. **A513**, 653 (1990).

[30] S. Takeuchi and M. Oka, Phys. Rev. Lett. **66**, 1271 (1991).

[31] S. Takeuchi, S. Nussinov, and K. Kubodera, Phys. Lett. B **318**, 1 (1993).

[32] C.E. Wolfe and K. Maltman, Phys. Lett. B **393**, 274 (1997).

[33] C. Nakamoto, Y. Suzuki, and Y. Fujiwara, Prog. Theor. Phys. **97**, 761 (1997); C. Nakamoto, Y. Fujiwara, and Y. Suzuki, Nucl. Phys. **A639**, 51c (1998).

[34] P.N. Shen, Z.Y. Zhang, Y.W. Yu, X.Q. Yuan, and S. Yang, J. Phys. G **25**, 1807 (1999).

[35] K. Shimizu and M. Koyama, Nucl. Phys. **A646**, 211 (1999).

[36] P.B. Mackenzie and H.B. Thacker, Phys. Rev. Lett. **55**, 2539 (1985).

[37] Y. Iwasaki, T. Yoshié, and Y. Tsuboi, Phys. Rev. Lett. **60**, 1371 (1988).

[38] J.W. Negele, A. Pochinsky, and B. Scarlet, Nucl. Phys. B (Proc. Suppl.) **73**, 255 (1999).

[39] I. Wetzorke, F. Karsch, and E. Laermann, hep-lat/9909037 (1999).

[40] S.A. Larin, V.A. Matveev, A.A. Ovchinnikov, and A.A. Pivovarov, Yad. Fiz. **44**, 1066 (1986); Sov. J. Nucl. Phys. **44**, 690 (1986).

[41] N. Kodama, M. Oka, and T. Hatsuda, Nucl. Phys. **A580**, 445 (1994); See also the footnote in S.D. Paganis, T. Udagawa, G.W. Hoffmann, and R.L. Ray, Phys. Rev. C **56**, 570 (1997) about a typographical error.

[42] J. Carlson and V.R. Pandharipande, Phys. Rev. D **43**, 1652 (1991).

[43] K. Nishikawa, N. Aoki, and H. Hyuga, Nucl. Phys. **A534**, 573 (1991).

[44] D. Pal and J.A. McGovern, J. Phys. G **18**, 593 (1992).

[45] S.K. Ghosh and S.C. Phatak, Phys. Rev. C **58**, 1714 (1998).

[46] M. Bozoian, J.C.H. van Doremalen, and H.J. Weber, Phys. Lett. B **122**, 138 (1983).

[47] J.L. Rosner, Phys. Rev. D **33**, 2043 (1986).

[48] C. Gignoux, B. Silvestre-Brac, and J.M. Richard, Phys. Lett. B **193**, 323 (1987).

[49] P. Zenczykowski, Phys. Rev. D **36**, 3517 (1987).

[50] T. Goldman, K. Maltman, G.J. Stephenson, Jr., K.E. Schmidt, and F. Wang, Phys. Rev. Lett. **59**, 627 (1987).

[51] N. Aizawa and M. Hirata, Prog. Theor. Phys. **86**, 429 (1991).

[52] B. Silvestre-Brac and J. Leandri, Phys. Rev. D$\tilde{K}^0$-K^0 **45**, 4221 (1992).

[53] F. Wang, J. Ping, G. Wu, L. Teng, and T. Goldman, Phys. Rev. C **51**, 3411 (1995).

[54] D.B. Lichtenberg, R. Roncaglia, and E. Predazzi, J. Phys. G **23**, 865 (1997).

[55] T. Goldman, K. Maltman, G.J. Stephenson, Jr., J. Ping, and F. Wang, Mod. Phys. Lett. A **13**, 59 (1998).

[56] F. Stancu, S. Pepin, and L.Y. Glozman, Phys. Rev. D **57**, 4393 (1998).

[57] N.I. Kochelev, Pis'ma Zh. Éksp. Teor. Fiz. **70**, 483 (1999); JETP Lett. **70**, 491 (1999).

[58] A.S. Carroll *et al.*, Phys. Rev. Lett. **41**, 777 (1978).

[59] A.M. Badalyan and Yu.A. Simonov, Yad. Fiz. **36**, 1479 (1982); Sov. J. Nucl. Phys. **36**, 860 (1982).

[60] G.T. Condo *et al.*, Phys. Lett. B **144**, 27 (1984).

[61] H. Bärwolff *et al.*, Ann. Physik. **43**, 407 (1986).

[62] B.A. Shahbazian, A.O. Kechechyan, A.M. Tarasov, and A.S. Martynov, Z. Phys. C **39**, 151 (1988).

[63] B.A. Shahbazian, V.A. Sashin, A.O. Kechechyan, and A.S. Martynov, Phys. Lett. B **235**, 208 (1990).

[64] B.A. Shahbazian, T.A. Volokhovskaya, V.N. Yemelyanenko, and A.S. Martynov, Phys. Lett. B **316**, 593 (1993).

[65] B.A. Shahbazian, T.A. Volokhovskaya, V.N. Yemelyanenko, and A.S. Martynov, Nuovo Cim. **A107**, 2459 (1994).

[66] A.N. Alekseev *et al.*, Yad. Fiz. **52**, 1612 (1990); Sov. J. Nucl. Phys. **52**, 1016 (1990).

[67] V.V. Barmin *et al.*, Phys. Lett. B **370**, 233 (1996).

[68] H. Ejiri *et al.* Phys. Lett. B **228**, 24 (1989).

[69] S. Aoki *et al.*, Phys. Rev. Lett. **65**, 1729 (1990).

[70] T. Nakano, Ph.D. dissertation, Kyoto University, 1990 (unpublished).

[71] J.K. Ahn *et al.*, Phys. Lett. B **444**, 267 (1998).

[72] S. Yamashita, Ph.D. dissertation, Kyoto University, 1995 (unpublished).

[73] Y. Itow, Ph.D. dissertation, Kyoto University, 1995 (unpublished).

[74] M.S. Chung, Ph.D. dissertation, Korea University, 1994 (unpublished).

[75] J.K. Ahn *et al.*, Phys. Lett. B **444**, 267 (1998).

[76] T. Iijima, Ph.D. dissertation, Kyoto University, 1995 (unpublished).

[77] F. Merrill, Ph.D. dissertation, Carnegie Mellon University, 1995 (unpublished).

[78] I.R. Sukaton, Ph.D. dissertation, Carnegie Mellon University, 1995 (unpublished).

[79] M. Burger, Ph.D. dissertation, University of Freiburg, 1996 (unpublished).

[80] L. Gan, Ph.D. dissertation, University of Manitoba, 1998 (unpublished).

[81] B. Bassalleck *et al.*, Few-Body Systems Suppl. **9**, 51 (1995).

[82] W.D. Ramsay, Proceedings of the 14th International Conference on Particles and Nuclei (PANIC96), eds. R.E. Mischke and T.W. Donnelly, World Scientific, Singapore, p.602 (1997).

[83] R.W. Stotzer *et al.*, Phys. Rev. Lett. **78**, 3646 (1997).

[84] R.W. Stotzer, Ph.D. dissertation, University of New Mexico, 1997 (unpublished).

[85] T. Bürger, Ph.D. dissertation, University of Freiburg, 1997 (unpublished).

[86] M. Godbersen, AIP Conference Proceedings **338**, 5th Conference on Intersections between Particle and Nuclear Physics, ed. S.J. Seestrom, p.533 (1995).

[87] R. Longacre *et al.*, Nucl. Phys. **A590**, 472c (1995).

[88] R. Longacre, Observation of $H(2210)$ Dibaryon through Weak Decay Modes $\Sigma^- p$ and $\Lambda p\pi^-$, produced in Heavy Ion Collisions with 14.6 A GeV/c Si Beam on Pb Target, BNL Report (1997).

[89] A.J. Baltz *et al.*, Phys. Lett. B **325**, 7 (1994).

[90] H.J. Crawford and T. Hallman, BNL-AGS Research Proposal E896 (1994).

[91] H.J. Crawford, Nucl. Phys. **A639**, 417c (1998).

[92] A. Rusek *et al.*, Phys. Rev. C **52**, 1580 (1995).

[93] A. Rusek *et al.*, Phys. Rev. C **54**, R15 (1996).

[94] A. Rusek, Ph.D. dissertation, University of New Mexico, 1995 (unpublished).

[95] A. Jacholkowski *et al.*, J. Phys. G **25**, 423 (1999).

[96] I. Chemakin *et al.*, Nucl. Phys. **A639**, 407c (1998).

[97] H. Kawai, KEK-PS Research Proposal E248 (1991).

[98] J. Belz *et al.*, Phys. Rev. Lett. **76**, 3277 (1996).

[99] J. Belz *et al.*, Phys. Rev. C **56** 1164, Addendum (1997).

[100] J. Belz *et al.*, Phys. Rev. D **53**, R3487 (1996).

[101] A. Alavi-Harati *et al.*, Phys. Rev. Lett. **84**, 2593 (2000).

[102] F.S. Rotondo, Phys. Rev. D **47**, 3871 (1993).

[103] J.F. Donoghue, E. Golowich, and B.R. Holstein, Phys. Rev. D **34**, 3434 (1986).

[104] M. Danysz *et al.*, Phys. Rev. Lett. **11**, 20 (1963).

[105] D.J. Prowse, Phys. Rev. Lett. **17**, 782 (1966).

[106] S. Aoki *et al.*, Prog. Theor. Phys. **85**, 1287 (1991).

[107] P. Khaustov, Nucl. Phys. **A639**, 375c (1998); P. Khaustov *et al.*, Phys. Rev. C **61**, 027601 (2000).

[108] P. Khaustov, Ph.D. dissertation, Carnegie Mellon University, 1999 (unpublished).

[109] T. Fukuda and R.E. Chrien, BNL-AGS Research Proposal E906 (1994).

[110] K. Nakazawa, KEK-PS Research Proposal E373 (1995).

[111] A.T.M. Aerts and C.B. Dover, Phys. Rev. D **28**, 450 (1983).

[112] Y. Yamamoto, T. Motoba, T. Fukuda, M. Takahashi, and E. Ikeda, Prog. Theor. Phys. Suppl. **117**, 281 (1994).

[113] A.J. Baltz, C.B. Dover, and D.J. Millener, Phys. Lett. B **123**, 9 (1983).

[114] A.T.M. Aerts and C.B. Dover, Phys. Rev. D **29**, 433 (1984).

[115] T. Yamada and K. Ikeda, Phys. Rev. C **56**, 3216 (1997).

[116] Y. Hirata, Y. Nara, A. Ohnishi, T. Harada, and J. Randrup, Prog. Theor. Phys. **102**, 89 (1999).

[117] K. Yamamoto *et al.*, Phys. Lett. B **478**, 401 (2000).

[118] M. Landry, Ph.D. dissertation, University of Manitoba, 2000 (unpublished).

[119] P.H. Pile *et al.*, Nucl. Instr. Meth. **A321**, 48 (1992).

[120] D.E. Alburger and M. May, To be published in Nucl. Instr. Meth. **A**.

[121] T. Iijima *et al.*, Nucl. Phys. **A546**, 588 (1992).

[122] V. Sum *et al.*, Nucl. Instr. Meth. **A326**, 489 (1993).

[123] M. Landry *et al.*, Nucl. Instr. Meth. **A421**, 31 (1999).

[124] I. Adachi *et al.*, Nucl. Instr. Meth. **A355**, 390 (1995).

[125] B.C. Byrd, P.L. McGaughcy, W.C. Sailor, R.C. Hammock, and Y. Yariv, Nucl. Instr. Meth. **A313**, 437 (1992).

[126] B.C. Byrd, W.C. Sailor, Y. Yariv, T.A. Carey, and A. Gavron, Nucl. Instr. Meth. **A313**, 457 (1992).

[127] K.L. Brown, F. Rothacker, D.C. Carey, and Ch. Iselin, Transport SLAC-91 (1991).

[128] C.B Dover, D.J. Millener, and A.Gal, Phys. Rep. **184**, 1 (1989).

[129] K. Imai, private communication.

[130] J.K. Ahn *et al.*, KEK Preprint 99-172 (2000); Submitted to Phys. Rev. C.

[131] J.K. Ahn, Ph.D. dissertation, Kyoto University, 2000 (unpublished).

[132] P.J. Litchfield *et al.*, Nucl. Phys. **B30**, 125 (1971).

[133] A.A. Hirata *et al.*, Nucl. Phys. **B30**, 157 (1971).

[134] V. Flaminio, W.G. Moorhead, D.R.O. Morrison, N. Rivoire, CERN HERA 83-02, Compilation of cross-sections 2, K^+ and K^- induced reactions, (1983).

[135] P. Khaustov *et al.*, Phys. Rev. C **61**, 054603 (2000).

[136] C.B. Dover, D.J. Millener, A. Gal, and D.H. Davis, Phys. Rev. C **44**, 1905 (1991).

[137] N. Aizawa and M. Hirata, Z. Phys. A **343**, 103 (1992).

[138] C.B. Dover *et al.*, Annals of Phys. **146**, 309 (1983).